CHAOTIC MOTIONS OF NONLINEARLY MOORED STRUCTURES

by

Amal Chandrakant Phadke

B.E., University of Bombay, India, 1989
M.Tech., Indian Institute of Technology, Bombay, India, 1991

A THESIS SUBMITTED IN PARTIAL FULFILLMENT OF

THE REQUIREMENTS FOR THE DEGREE OF

MASTER OF APPLIED SCIENCE

in

THE FACULTY OF GRADUATE STUDIES

DEPARTMENT OF CIVIL ENGINEERING

We accept this thesis as conforming

to the required standard

THE UNIVERSITY OF BRITISH COLUMBIA

August 1993

© Amal C. Phadke, 1993

In presenting this thesis in partial fulfilment of the requirements for an advanced degree at The University of British Columbia, I agree that the Library shall make it freely available for reference and study. I further agree that permission for extensive copying of this thesis for scholarly purposes may be granted by the Head of my Department or by his or her representatives. It is understood that copying or publication of this thesis for financial gain shall not be allowed without my written permission.

Department of Civil Engineering
The University of British Columbia
2324 Main Mall
Vancouver, BC V6T 1Z4
CANADA

Abstract

A number of studies have described the theoretical and numerical aspects of the chaotic motions of offshore structures with nonlinear moorings. As one such example, Aoki, Sawaragi and Isaacson (1993) described the numerical simulation of the motions of a single degree of freedom system with a piecewise-linear restoring force function. However, relatively few laboratory measurements of chaotic motions have been reported, and the primary aim of the present study is to investigate the corresponding problem experimentally. Thus, the present work describes the measurement of chaotic motions of a floating structure with nonlinear moorings. The structure is modeled as a rectangular box, and the moorings are represented by a nonlinear restoring force - displacement relationship, corresponding to an idealized geometric nonlinearity associated with a slack mooring or a mooring with gaps.

The experiments were conducted in the wave flume of the Hydraulics Laboratory of the Department of Civil Engineering at the University of British Columbia. The flume is 40 m long, 0.62 m wide, operates with a nominal water depth of 0.55 m, and is equipped with a wave generator capable of producing regular and random waves and controlled by a DEC VAXstation-3200 computer.

The model structure is 76 cm long × 25 cm wide × 20 cm high. Two vertical Plexiglas plates parallel to the sides of the wave flume were installed so as to limit the structure motions to three degrees of freedom corresponding to surge, heave and pitch. Ball bearings mounted on the sides of the box are used to minimize friction between the plates and the structure. Two vertical cantilevered beams located at some distance from the each end of the structure were used to simulate the nonlinear mooring stiffness.

Displacement measurements at three different locations on the body were made using potentiometers mounted on a rigid aluminum frame, with a system of strings, pulleys and counter-weights used to transmit the structure motions to the potentiometers. The measured displacements were transformed to provide the surge, heave and pitch motions with respect to the centre of gravity of the structure.

The results are presented in the form of time series, phase portraits, spectra, Poincaré maps, and Lyapunov exponents. The influence of various governing parameters on the response is examined. These include a dimensionless wave height, which characterizes the magnitude of the excitation; a relative wave frequency; and gap width and a dimensionless spring stiffness, which characterize the moorings.

Periodic, sub-harmonic and chaotic responses are observed for both monochromatic and bichromatic waves. In general, sub-harmonic and chaotic responses were obtained for bichromatic excitation to a greater extent than for monochromatic excitation. Transient chaotic motions have also been observed, such that the response initially appears to be very irregular, but eventually settles to a regular periodic motion. Poincaré maps of the response exhibit a distinct fractal structure under certain conditions, indicating the presence of chaotic motions. Finally, Lyapunov exponents, which provide a quantitative indication of chaotic motions, have also been computed for each time series, and are used to confirm the presence of chaotic motions.

Table of Contents

List of Tables

List of Figures

Acknowledgments

The author would like to thank his supervisor Dr. Michael Isaacson for his guidance and encouragement throughout the preparation of this thesis. The author would like to express a special word of gratitude to Kurt Nielson of the Civil Engineering Department Workshop at UBC for his help in building the model and other associated facilities. Thanks also to John Wong for making available the required electronic parts and components and to Sundar Prasad for his help with the computing and wave generator facilities. A special acknowledgment is made to Sundar Prasad, Andrew Kennedy and Dr. Fai Cheung for their advice and suggestions during the course of this experimental work. Finally, the financial support in the form of a Research Assistantship from the Natural Sciences and Engineering Research Council of Canada is gratefully acknowledged.

Chapter 1

Introduction

1.1 General

The phenomenon of chaotic behaviour in nonlinear dynamical systems has received considerable attention in recent years. At the turn of the century, the French mathematician H. Poincaré (1890) discovered that certain mechanical systems whose time evolution is governed by Hamilton's equation could display chaotic motion. Unfortunately, this was considered by many physicists as a mere curiosity, and it took another 65 years until in 1963 meteorologist Edward Lorenz discovered a similar phenomenon. Lorenz (1963), in his famous work "Deterministic non-periodic flow", which was published in the *Journal of Atmospheric Science*, presents a system of three differential equations which are deterministic, but show very irregular (also called *random-like*) behaviour. Lorenz's paper, the general importance of which is recognized today, was not widely appreciated until many years after its publication. He discovered one of the first examples of deterministic chaos in dissipative systems. A physical system is said to have deterministic time dependence, if there exists a well defined governing differential or difference equation for calculating its future behaviour from given initial conditions.

The term *deterministic chaos* denotes an irregular or chaotic motion that is generated by a nonlinear system whose dynamical laws uniquely determine the time evolution of a state from the knowledge of its previous history. In recent years, new theoretical results, the availability of high speed computers, and refined experimental techniques have made it clear

that this phenomenon is widespread in nature and has far reaching consequences in many branches of science and technology.

Examples of nonlinearities in mechanical and electrical systems include the following:

- Nonlinear elastic or spring elements
- Nonlinear damping such as friction
- Backlash, limiters or bilinear springs
- Fluid related forces
- Nonlinear boundary conditions
- Nonlinear feedback control forces in servo systems
- Nonlinear resistive, capacitor or inductive circuit elements
- Diodes
- Many transistors and other active devices
- Electric and magnetic forces

It should however be noted that, a system nonlinearity is a necessary but not a sufficient condition for the generation of a chaotic motion.

Observed chaotic behaviour is not due to external sources of noise, but rather is a property of the nonlinear system which results in adjacent trajectories separating exponentially fast in a bounded region of phase space. Consequently, it becomes virtually impossible to predict the long-term behaviour of such systems, because in practice initial conditions can only be fixed with finite accuracy, and errors increase exponentially fast. An attempt to solve such a nonlinear system on a computer, gives rise to a result which depends increasingly on more decimal digits of the numbers representing the initial conditions. Since, the errors increase exponentially fast, even a very small change in the initial conditions produce an entirely different response.

The above results give rise to a number of fundamental questions:

- Can one predict whether or not a given system will display deterministic chaos?

- Can one specify the notion of chaotic motion more mathematically and develop quantitative measures for chaos?
- Does the existence of deterministic chaos imply the end of long-time predictability in physics for certain nonlinear systems or can one still learn something from a chaotic signal?

These questions have been discussed in great detail in literature. (e.g. Schuster, 1988).

1.2 Literature Review

Although there is a vast literature on chaotic behaviour in nonlinear dynamical systems, there has been relatively little work reported on the chaotic motions of floating structures with nonlinear moorings. Before discussing chaos in nonlinear offshore systems, a brief review of chaos in nonlinear systems will be presented in paragraphs to follow for the sake of completeness.

As already mentioned, considerable interest in chaotic systems began after Lorenz' (1963) work on the model of atmospheric convection. Many other deterministic equations showing chaotic behaviour have been obtained, both as simple, analytical systems and as models of real physical, biological or chemical systems. These include both systems of nonlinear ordinary differential equations and maps.

Duffing's equation is perhaps the most widely studied by researchers working in the area of chaotic dynamics. It is defined as

$$\ddot{x} + a\dot{x} + bx + cx^3 = f(x) \tag{1.1}$$

where, an overdot denotes a time derivative.

This equation is important in the theory of nonlinear oscillations because of the large number of systems that can be modeled by it. Duffing's equation in a slightly different form was investigated by Ueda (1979) as applied to certain electrical systems.

$$\ddot{x} + a\dot{x} + x^3 = B \cos t \tag{1.2}$$

This equation is now widely recognized as exhibiting important dynamical properties. An excellent coverage of Duffing's equation can be found in Kapitaniak (1991).

The concept of chaos is relatively new to ocean engineering. The first reported research work dates back to mid to late eighties. In their pioneering work, Bishop and Virgin (1988) used a combined numerical and geometric approach to study the dynamic behaviour of a moored semi-submersible based on solutions of the nonlinear differential equation used to model the system. They observed competing steady states, sub-harmonic resonance and chaos as typical responses in regular seas. They used a quantitative overview to classify the computer generated results of direct time simulation, with the aim of illustrating the inadequacies and limitations of a linear, analytical approach.

Aoki, Sawaragi and Isaacson (1993) have studied motions of a floating body with nonlinear moorings modeled as a single degree of freedom system. Response of the system to monochromatic and bichromatic excitation with both material and geometric nonlinearities is studied. They have reported existence of jump phenomenon for both material and geometric nonlinearity cases. They report sub-harmonic and chaotic response for geometrically nonlinear system for monochromatic and bichromatic excitation.

The damping ratio is a one of the most crucial parameters deciding the system behaviour. Chaotic behaviour in nonlinear systems is normally found at lower damping ratios. Aoki, Sawaragi and Isaacson (1993) have reported that chaotic behaviour disappears at high damping ratios. Interestingly, Sumanuskajonkul and Hu (1992) have observed that in certain dynamical systems chaotic motions may occur at high damping situations even

when periodic motions are found at identical low damping systems. They investigated dynamic responses of bilinear and impacting oscillators subjected to harmonic loading. Instead of adapting the frequency ratio of excitation and structure as the controlling parameter, they used damping and stiffness ratio.

Gottlieb et. al. (1990) have reported on a semi-analytic method for predicting local instability, global bifurcation and the onset of chaotic motion in a multi-point mooring system. They considered large geometric nonlinearities and combined periodic waves and regular current. They have shown that a stability analysis based on an approximate solution of a strongly nonlinear ocean system can serve as an efficient indicator for the nonlinear behaviour, thus reducing numerical search efforts for global instability and chaotic response regions.

Yim and Lin (1991) investigated chaotic and stochastic dynamics of the rocking response of free-standing offshore equipment subjected to horizontal base excitation. They used a realistic model to take into account the geometric nonlinearity (finite slenderness ratio) of the rocking system. Additional important nonlinear effects including transition of governing equations of motion at impact were examined. It was demonstrated that the nonlinearities associated with the transition of governing equations at impact produced complex responses. In addition to the anticipated harmonic and sub-harmonic periodic responses, two new types of steady state motions - quasi-periodic and chaotic responses were observed. In this study, it was shown that although the excitations to the rocking systems were simple and purely deterministic, some stochastic characteristics of the chaotic rocking responses could be detected using Poincaré maps and amplitude probability densities.

Papoulias and Bernitsas (1988) analyzed dynamic behaviour of a single-point mooring system under time-dependent external excitation. They described the time evolution of the corresponding dynamical system in a six-dimensional phase space. Bifurcation sequences of

state equations were studied and parameter values at which the response of SPM changed rapidly were identified. An analysis of stability and instability domains of the system revealed regions of operationally hazardous response. An important conclusion of their study was that an SPM system under time-independent environmental excitation might not stay in a position of static equilibrium.

Lyapunov exponents are perhaps the best quantitative estimate of chaotic nature of a deterministic dynamical system. A Lyapunov exponent characterize the properties of an attractor of a dynamical system. Lyapunov exponents are related to the average rates of convergence and/or divergence of nearby trajectories in phase space and, therefore, they measure how predictable or unpredictable the system is. A considerable amount of work has been reported on the estimation of the Lyapunov exponents. They were introduced to the theory of dynamical systems by Oseledec (1968). The first numerical visualization of the chaotic motion in phase space trajectory in terms of the divergence of nearby trajectories was introduced in Henon & Heiles (1964). It was then developed further by Chirikov (1979), Ford (1975), Wolf et al. (1985), Wolf (1986) and others.

Generally, in experimental chaotic dynamics, observations are stored in the form of a time series. The next important step is to assess whether the system behaviour is chaotic or periodic. The Lyapunov exponent offers a quantitative measure of aperiodicity of the system response. Generally Wolf et. al. (1985) are credited with presenting the first algorithm to compute Lyapunov exponents from experimental time series. They provide two useful computer programs to evaluate the two largest Lyapunov exponents. A system with one or more positive Lyapunov exponents is defined to be chaotic. Recently Frank (1992) has modified the algorithm of Wolf et. al. for the improved estimation of the largest Lyapunov exponent in the case of noisy and small data sets. Wolf's algorithm is useful to compute the two largest Lyapunov exponents only. A few other algorithms to compute all Lyapunov exponents have been proposed in literature (e.g. Parker and Chua, 1989).

However, in spite of its limitation, Wolf's algorithm has been widely used by researchers in the area of chaotic dynamics.

1.3 Scope of Present Work

The primary aim of the present investigation is to detect chaos experimentally in a nonlinear offshore structural system. Several numerical studies have been reported on this topic before, but there is generally a lack of supporting experimental work. On the basis of a single degree of freedom model, Aoki, Sawaragi and Isaacson (1993) have reported sub-harmonic and chaotic surge motions in an offshore structural system with geometrically nonlinear moorings and their work is taken as a base for the present experimental investigation. A three degree of freedom system is considered, such that heave and pitch degrees of freedom are included in addition to surge. Displacement measurements at three different locations on the body are made using potentiometers mounted on a rigid aluminum frame, with a system of strings, pulleys and counter-weights used to transmit the structure motions to the potentiometers. The measured displacements are transformed to provide the surge, heave and pitch motions with respect to the centre of gravity of the structure (Appendix A provides a detailed derivation of these transformation equations). The results are presented in the form of time series, phase portraits, spectra, Poincaré maps, and Lyapunov exponents. The influence of various governing parameters on the response is examined. These include a dimensionless wave height, which characterizes the magnitude of the excitation; a relative wave frequency; and gap width and a dimensionless spring stiffness, which characterize the moorings. Finally, the largest Lyapunov exponent is computed for each experimental time series using Wolf's algorithm. An analysis of the results shows that chaos is indeed observed in this nonlinear dynamical system. An analytical approach to the present problem involves solution of the nonlinear equation of motion in time domain. This procedure is described briefly in Appendix B.

Chapter 2

Nonlinear Dynamics and Chaos

Introduction

This chapter provides a brief introduction to the theory of nonlinear dynamics and its applications to chaotic systems. This provides sufficient theoretical background of chaotic dynamics, and discusses methods employed in identifying and quantifying chaotic motions. The ideas discussed in the present chapter will be incorporated directly in subsequent chapters in order to analyze experimental data.

2.1 Nonlinear Dynamics

The spring-mass-dashpot system shown in Fig. 2.1 provides the classic example of a dynamic system exhibiting linear vibrations. In the absence of any external excitation, the undamped system ($\lambda = 0$) vibrates with a frequency ω_0 that is independent of the amplitude of vibration.

$$\omega_0 = \left\{ \frac{k}{M} \right\}^{1/2} \tag{2.1}$$

where, M and K are respectively the mass and stiffness. In this state, energy flows alternately between elastic energy in the spring and kinetic energy in the mass. The presence of damping introduces a decay in the free vibration such that the displacement amplitude of the mass exhibits the following time dependence:

$$x(t) = A_0 e^{-\zeta\omega_n t} \cos\ (\omega_d t - \phi) \tag{2.2}$$

where, x(t) is the instantaneous displacement response, A_0 is the displacement response amplitude, ζ is the damping ratio, ω_d is the damped natural frequency and ϕ is the phase difference between the input excitation and displacement response.

One of the classic phenomena of such a linear system is that of *resonance* under harmonic excitation. For this problem, the differential equation that models the system may be expressed in the form:

$$\ddot{x} + 2\zeta\omega_n\dot{x} + \omega_n^2 x = F_0 \cos \omega t \tag{2.3}$$

where, an overdot represents a time derivative, F_0 and ω are the forcing function amplitude frequency respectively.

If F_o is fixed and the driving frequency ω is varied, the absolute magnitude of the steady state displacement reaches a maximum which is close to the natural frequency ω_n at the damped natural frequency ω_d. This phenomenon is illustrated in Fig. 2.2 as a transfer function plot. The effect is more pronounced when the damping ratio ζ is small. With this background, the behaviour of nonlinear systems is now considered.

2.1.1 Nonlinear Vibration Theory

A classical example of a nonlinear system is one with a nonlinear spring described by the *Duffing* equation.

$$\ddot{x} + 2\zeta\omega_n\dot{x} + \alpha x + \beta x^3 = F(t) \tag{2.4}$$

where, α and β are coefficients of the nonlinear stiffness term.

If the system is acted on by a periodic force, in the classical theory one assumes that the output also will be periodic. When the output has the same frequency as the force, the resonance phenomenon for the linear spring is shown in Fig. 2.3. If the amplitude of the forcing function is held constant, there exist a range of forcing frequencies for which three possible output amplitudes are possible as shown in Fig. 2.3. One can show that the dashed curve in Fig. 2.3 is unstable so that a *hysteretic effect* occurs for increasing and decreasing frequencies. This is called a *jump phenomenon.* Other periodic solutions can also be found such as *sub-harmonic* and *superharmonic* vibrations. Sub-harmonics play an important role in pre-chaotic vibrations.

There exist three classic types of dynamical motion:

- Equlibrium
- Periodic motion or limit cycle
- Quasiperiodic motion

These states are called attractors, since if some form of damping is present the transients decay and the system is *attracted* to one of the above three states. There is another class of motions in nonlinear vibrations that is not one of the above classic attractors. This new class of nonlinear motions is chaotic and is known in literature as a *strange attractor.*

2.2 Identifying Chaotic Vibrations

In this section, a set of diagnostic tests are presented to help in identifying chaotic oscillations in physical systems. Engineers often have to diagnose the source of unwanted oscillations in physical systems. The ability to classify the nature of oscillations can provide a clue as to how to control them. For example, if the system is thought to be *linear*, large periodic oscillations may be traced to a *resonance* effect. However, if the system is non-

linear, a limit cycle may be the source of periodic vibration, which in turn may be traced to some dynamic instability in the system.

A checklist to identify chaotic or non-periodic motion is compiled below:

Qualitative Methods

- Identifying a nonlinear element in the system
- Check for sources of random input in the system
- Observe the time history of the measured signal
- Examine the phase plane history
- Examine the Fourier spectrum of the signal
- Obtain the Poincaré map of the signal.
- Vary the system parameters (routes to chaos)

Quantitative Method

- Compute the Lyapunov exponents

A diagnosis of chaotic vibrations implies that one has a clear definition of such motions. However, as research uncovers more complexities in nonlinear dynamics, rigorous definitions seem to be limited to certain classes of mathematical problem. An experimentalist may find this rather difficult to achieve, so that one is encouraged to use two or more tests to obtain a consistent picture of the chaos.

Characteristics of Chaotic Vibrations

Following are some of the important characteristics of chaotic vibrations:

- Sensitivity to initial conditions
- Broad spectrum of Fourier transform when motion is generated by a single frequency

- Fractal properties of motion in phase space which denote a strange attractor
- Increasing complexity of regular motions as some experimental parameter is changed
- Transient or intermittent chaotic motion; nonperiodic bursts of irregular motion (intermittency) or initially randomlike motion that eventually settles down into a regular motion

Tests to identify chaotic motion can be divided into two categories, viz., *qualitative* methods and *quantitative* methods. Each of these methods will be discussed separately in following sections.

2.2.1 Nonlinear System Elements

A chaotic system must have nonlinear elements or properties. This is a necessary but not a sufficient condition. A linear system cannot exhibit chaotic vibrations. In a linear system, periodic inputs produce periodic outputs of the same frequency after transients have decayed. In mechanical systems, nonlinearities may exist as a result of:

- Nonlinear elastic or spring elements
- Nonlinear damping
- Most systems with fluids
- Nonlinear boundary conditions

Nonlinear elastic effects can be associated with either material or geometric properties.

2.2.2 Random Inputs

In chaotic vibrations, the excitation is assumed to be deterministic. By definition, chaotic vibrations arise from nonlinear deterministic physical systems or nonlinear deterministic differential or difference equations. It is presumed that large non-periodic signals do not

arise from very small input noise. Thus, a large output signal to input noise ratio is required if one is to attribute a non-periodic response to a deterministic system behaviour.

2.2.3 Observation of Time Series

Usually, the first clue that a physical model exhibits chaotic vibrations arises from an observation of the time series of the output signal. The motion is observed to exhibit no pattern or periodicity. However, this test is not very reliable, since a motion could have a long-period behaviour that is not easily detected. Also, some nonlinear systems exhibit quasi-periodic vibrations where two or more incommensurate signals are present. Here the signal may appear to be non-periodic but can be broken down into the sum of two or more periodic signals.

2.2.4 Phase Portrait

Consider a single degree of freedom system with displacement x(t) and velocity v(t). The phase plane is defined as the set of points (x,v). When the motion is periodic, the phase plane orbit traces a closed curve. For example, the forced oscillations of a linear spring-mass-dashpot system exhibit an elliptical orbit. However, a forced nonlinear system with cubic spring element may show an orbit that crosses itself but is still closed corresponding to sub-harmonic oscillations.

On the other hand, chaotic motions correspond to orbits that never close or repeat. Thus, the trajectory of the orbits in the phase space will tend to fill up a section of the phase space. Although this wandering of orbits provides a clue to chaos, continuous phase plane plots provide relatively little information, and a modified phase plane technique called the *Poincaré mapping* should rather be used.

2.2.5 Fourier Spectrum

The appearance of a broad spectrum of frequencies in the output signal is another characteristic of chaotic vibrations. This feature becomes more important if the system is of low dimension (one to three degrees of freedom). Often, if there is an initial dominant frequency component ω_0, a precursor to chaos is the appearance of sub-harmonics at frequencies ω_0/n in the frequency spectrum. In addition, harmonics of this frequency will also be present, i.e. at $m\omega_0/n$.

However, it may be erroneous to conclude that multi-harmonic outputs imply chaotic vibrations, since the system in question may turn out to posses many degrees of freedom. In systems with many degrees-of-freedom, the Fourier spectrum may not be of much value in detecting chaotic vibrations, unless one can observe changes in the spectrum as one varies some parameter such as driving amplitude or frequency.

2.2.6 Poincaré Map

The theoretical basis for Poincaré maps was introduced by Poincaré (1898). The recent widespread use of computers with graphics facilities for examining chaotic behaviour in dynamical systems has led to the method of Poincaré maps becoming one of the most popular and illustrative methods.

Consider, the motion of a point with time as displayed in the phase plane (displacement, velocity). Rather than viewing the continuous motion of the point, it is convenient to view the point at discrete times so that the motion appears as a sequence of dots in the phase plane. If $x_n = x(t_n)$ and $y_n = \dot{x}(t_n)$, this sequence in the phase plane represents a *two-dimensional* map, which when the sampling time t_n is chosen according to certain rules is called a *Poincaré Map*. When the exciting motion is periodic with period T, an obvious sampling rule for a Poincaré map is to choose $t_n = nT + \tau_0$, where τ_0 is an arbitrarily chosen

time delay. This allows one to distinguish between periodic motions and non-periodic motions.

A Poincaré map enables the study of continuous time systems to be reduced to the study of an associated discrete time system. The construction of the Poincaré map involves elimination of at least one of the variables of the system, resulting in a lower dimensional problem to be studied. In lower dimensional problems numerically computed Poincaré maps provide an insightful display of the global behaviour of the system. Unfortunately, there exists no general method of constructing the Poincaré maps associated with arbitrary ordinary differential equations, since this construction requires some knowledge of the geometrical structure of the phase space of the ordinary differential equation.

2.2.7 System Parameter Variation

In examining a system for chaotic response, it is useful to vary one or more of the control parameters of the system, so that one may examine the presence of a steady or periodic response for some range of parameter space. In this way one can have confidence that the system is deterministic and that there are no hidden inputs and sources of truly random noise.

In changing a parameter, one looks for a pattern of periodic responses. A response characteristic precursor to chaotic motion is the appearance of a sub-harmonic periodic response and by varying the system parameters, such sub-harmonic vibrations may change into chaotic motion.

2.2.8 Lyapunov Exponents

Lyapunov exponents are perhaps the most useful diagnostic tool for detecting a chaotic response. Lyapunov exponents measure the mean rate of divergence of adjacent trajectories. They were introduced in a form adapted to the theory of dynamical systems and to ergodic theory in the late sixties, when Oseledec (1968) published his non-communicative ergodic theorem which provides a general and simple way to compute all Lyapunov exponents. In the general case, there are as many exponents as phase-space dimensions, though a particular Lyapunov exponent is not associated with a unique direction in phase space. An excellent coverage of Lyapunov exponents may be found in Wolf (1986). Positive Lyapunov exponents indicate divergence and chaos, while negative or zero Lyapunov exponents are characteristic of regular behaviour.

Chaos in deterministic systems implies a sensitive dependence on initial conditions. This means that, if two trajectories start close to one another in phase space, they will move exponentially away from each other for small times on the average. If L_0 is the initial distance between the two starting points, at a small time later the distance changes to

$$L(t) = L_0 \, 2^{\lambda t} \tag{2.5}$$

where, λ is the Lyapunov exponent. The choice of base '2' is arbitrary but convenient.

The divergence of chaotic orbits can only be locally exponential, since if the system is bounded, as most physical experiments are, L(t) cannot go to infinity. In order to define this divergence of orbits, the exponential growth may be averaged at many points along the trajectory as shown in Fig. 2.5. The process involves beginning with a reference trajectory (called a *fiduciary*) and a point on a nearby trajectory, and measuring $L(t)/L_0$. When L(t) becomes too large (i.e. the growth departs from exponential behaviour), a new nearby

trajectory is chosen and a new $L_0(t)$ is defined. Hence, the first Lyapunov exponent is defined as

$$\lambda = \lim_{N \to \infty} \frac{1}{t_N - t_0} \sum_{k=1}^{N} \log_2 \left\{ \frac{L(t_k)}{L_0(t_{k-1})} \right\} \tag{2.6}$$

where k is an iteration number. The limit of large N is necessary to obtain a quantity that both describes long-term behaviour and is independent of initial conditions. The motion is considered chaotic, if $\lambda > 0$ and regular if $\lambda \leq 0$.

This procedure can also be used to estimate Lyapunov exponents from an experimental time series as described in section 2.2.9.

2.2.9 Estimation of Lyapunov exponents from experimental time series

As mentioned earlier, there are as many exponents as phase-space dimensions. For an experimental time series, the number of phase-space dimensions may not be known in advance. In such a case, the technique of phase-space reconstruction with delay coordinates makes it possible to obtain Lyapunov spectrum from discrete time samples of almost any dynamical observable. An m-dimensional phase portrait of a time series x(t) can be constructed by the delay co-ordinates method. A point on the attractor is given by $\{x(t), x(t+\tau), \ldots, x(t+(m-1)\tau)\}$, where τ is the almost arbitrarily chosen delay time. The nearest neighbour in the Euclidean sense to the initial point $\{ x(t_0), x(t_0+\tau), \ldots, x(t_0+(m-1)\tau) \}$ is chosen, with the distance between these two points denoted as $L(t_0)$. After time t_1, the initial length will have evolved to the length $L'(t_1)$. The length element is propagated through the attractor for a time short enough so that only a small-scale attractor structure is likely to be examined. If the evolution time is too large L' shrinks as the two trajectories that define its pass through a folding region of the attractor. In this case there is an

underestimation of λ_1, so that a new data point must be selected that satisfies the following two criteria:

- Its distance from the evolved fiducial point is small
- the angular separation between the evolved and replacement elements is small.

This procedure is described in Fig. 2.6. When the proper replacement point cannot be found, the points that were being used are retained. This procedure is repeated until the fiducial trajectory has traversed the entire data file, at which point λ_1 may be estimated:

$$\lambda_1 = \lim_{n \to \infty} \frac{1}{t_n - t_0} \ln \frac{L'(t_k)}{L'(t_{k-1})} \tag{2.7}$$

as the maximum Lyapunov exponent.

Wolf et. al. (1985) provide a useful computer program to compute the largest Lyapunov exponent from experimental time series. This program has been used in the present investigation.

In Chapter 4, the methods discussed above will be applied to the experimental observations.

Chapter 3

Experimental Investigation

Introduction

As mentioned earlier, one of the aims of present research is the demonstration of the chaotic response of floating structures with nonlinear moorings. Keeping this objective in mind, a series of experiments were carried out at the Hydraulics Laboratory of the Civil Engineering Department, UBC. This chapter gives a detailed account of this experimental investigation. A numerical approach to the present problem involves solving the nonlinear equation of motion in the time domain using appropriate time stepping procedure. Appendix B may be referred for a brief description of the procedure involved.

The floating structure model is a rectangular plywood box. The nonlinear spring action is simulated by two cantilever beams placed on either side of the box. The cantilever beam is not in immediate contact with the box, but leave some gap between the box and itself. GEDAP software developed by NRC is used for wave generator control and data acquisition.

3.1 Dimensional Analysis

Dimensional analysis provides an important preliminary step to any experimental investigation and may be used to identify key non-dimensional parameters of the problem at hand. In the present case, the response in any degree of freedom may be expressed as a

function of parameters characterizing the incident wave conditions, structural and fluid properties. Hence, for a monochromatic wave train we may write

$$R = f\,(H, T, d, B, d_g, k, K, M, \rho, g, \zeta) \tag{3.1}$$

where, H, T and d are the incident wave height, incident wave period and water depth respectively. Also d_g, k, K and M are the gap width, spring stiffness, stiffness ratio and mass respectively; and ρ, g and ζ are the water density, gravitational acceleration and damping ratio respectively.

Dimensional analysis yields

$$\frac{R}{H} = f\left\{ \frac{H}{gT^2}, \frac{d}{H}, \frac{B}{H}, \frac{d_g}{H}, \frac{M}{\rho H^3}, \frac{\omega}{\omega_n}, \zeta, K \right\} \tag{3.2}$$

Similarly, for a bichromatic incident wave train, we can write

$$R = f\,(H, T, d, B, d_g, k, K, M, \zeta, \Delta T, \rho, g) \tag{3.3}$$

where, ΔT is the difference in the incident wave periods.

which gives

$$\frac{R}{H} = f\left\{ \frac{H}{gT^2}, \frac{d}{H}, \frac{B}{H}, \frac{d_g}{H}, \frac{M}{\rho H^3}, \frac{\omega}{\omega_n}, \frac{\Delta T}{T}, \zeta, K \right\} \tag{3.4}$$

3.2 Natural Frequency in Surge

For a linear dynamical system, the undamped natural frequency is constant and is given by

$$\omega_n = \sqrt{\frac{k}{M}} \tag{3.5}$$

In contrast to this, for a nonlinear dynamical system the undamped natural frequency is not constant, but is a function of the initial displacement. For the present problem involving a floating box with nonlinear stiffness, an expression for the undamped natural frequency in surge motion may be derived as indicated below.

Let the initial compression of the spring K_1 be δ_1. Hence, the potential energy stored in the spring will be

$$PE = \frac{1}{2} k_1 \delta_1^2 \tag{3.6}$$

Assuming no energy loss, and from the principle of conservation of energy, the potential energy PE stored in the spring must be equal to the kinetic energy of the box. Hence, we may write

$$KE = \frac{1}{2} MV^2 = \frac{1}{2} k_1 \delta_1^2 \tag{3.7}$$

which gives

$$V = \sqrt{\frac{k_1}{M}}\, \delta_1 \tag{3.8}$$

The time required to uncompress spring k_1 is $T_1/4$, where T_1 is the natural period of vibration of the spring k_1. As the box loses contact with spring k_1, it travels a distance of $d_{g1}+d_{g2}$ with a constant velocity V as there is no energy loss. The kinetic energy of the box is still 1/2 MV^2. The box then compresses spring k_2 and the maximum compression of the spring k_2 is

$$\delta_2 = \sqrt{\frac{M}{k_2}}\, V \tag{3.9}$$

Hence, the total time required to complete one cycle is

$$T_n = \frac{T_1}{2} + 2\,\frac{d_{g1}+d_{g2}}{V} + \frac{T_2}{2} \tag{3.10}$$

Since, $V = \omega_1 \delta_1$, $T_1 = 2\pi/\omega_1$ and $T_2 = 2\pi/\omega_2$, we may rewrite Eq. (3.10) as

$$T_n = \frac{\pi}{\omega_1}\left[1 + \frac{\omega_1}{\omega_2} + 2\,\frac{d_{g1}+d_{g2}}{\delta_1} \right] \tag{3.11}$$

where, T_n is the natural period in surge. Hence, the natural frequency ω_n in surge is

$$\omega_n = \frac{2\,\omega_1}{\left[1 + \frac{\omega_1}{\omega_2} + 2\,\frac{d_{g1}+d_{g2}}{\delta_1} \right]} \tag{3.12}$$

Eq. (3.12) indicates the dependence of natural frequency on the initial displacement δ_1. It may be noted that natural frequency decreases with an increasing gap width and increases for an increasing initial displacement.

For a linear system, with $k_1 = k_2$ and $d_{g1} = d_{g2} = 0$, the natural frequency ω_n reduces to ω_1 as expected.

3.3 Location of Centre of Gravity

Responses in the surge, heave and pitch degrees of freedom are defined as the displacements of the centre of gravity of the system with respect to these three degrees of freedom. Hence, it is important to know the location of the centre of gravity. This may be accomplished as described below.

The box is idealized as a set of discrete masses $m_1..m_4$ as indicated in Fig. 3.2. Referring to Fig. 3.2, m_1, m_2 and m_3 are the masses of upstream/downstream side pieces, lateral pieces and bottom piece respectively. The "m_4" is the external mass added to the system.

Due to symmetry, the centre of gravity will be located on a vertical axis passing through the centre of the box as shown in Fig. 3.2. Hence, the x coordinate of the centre of gravity with respect to the lower bottom corner of the box is B/2, where B is the beam length. The y coordinate can be computed by taking moments of the masses about the bottom edge of the box. Hence, we may write

$$G_y = \left\{ \frac{(2m_1 + m_2)\, d_1 + 2m_4\, d_3}{2m_1 + m_2 + m_3 + 2m_4} \right\} \tag{3.13}$$

3.4 Measurement of Spring Stiffness

As mentioned earlier, aluminum cantilever beams were used to simulate nonlinear spring action. The load-deflection curve for these aluminum cantilever beams was found to be linear. Fig. 3.3 shows a schematic diagram of the procedure used to obtain the load-deflection curve.

A load P is applied at a distance z from the fixed end of the beam. Deflection δ of the beam at the point of application of load P is measured. The procedure is repeated for different load values. The load-deflection values are as shown in Table 3.1. The deflection in column 3 is calculated from applied load 'P' as, $\delta = Pz^3/3EI$. It is evident from Table 3.1 that, the load-deflection behaviour is quite linear and there is a good agreement between experimental and calculated values (Fig. 3.4). Hence for calculating ω/ω_n and K, the computed values of spring stiffness are used.

3.5 Experimental Setup

3.5.1 General

Fig. 3.5 shows a schematic sketch of the entire experimental setup. The floating object is a hollow plywood box of size 30" X 10" X 8" (76 cm X 25 cm X 20 cm) suitably coated with waterproof paint to avoid water seepage. The empty box has a mass of 4.1 kg. Provision is made to add extra weights to the box so as to vary its mass and mass moment of inertia. These extra weights, each of mass 6.25 kg, are kept at 6 cm from the plane of symmetry of the box as shown in the figure. Two Plexiglas plates limit motion of the box to three degrees of freedom, viz., *surge*, *heave* and *pitch*. Eight ball bearings mounted on longer sides minimize friction between Plexiglas plates and the box which otherwise would have had an adverse effect on the experiments. Two cantilever beams are used to simulate the nonlinear springs, with different size beams used to vary the effective spring constant.

Displacement measurements at three different locations on the body are carried out using displacement probes. These probes consist of strings, about 1.5 m long with one end attached to the point of measurement on the box. These strings run over three pulleys fitted with potentiometers and are mounted on a rigid aluminum frame. Small weights ($\approx$ 100 gm) are attached to the free ends of the strings to keep them under tension at all times and to prevent slippage. The potentiometers require a $\pm$ 5 V regulated DC supply. The gap width d_g may be varied as required. During the experiments, spurious high frequency spring vibrations were initially observed, and were eliminated by the use of rubber bands acting as vibration dampers.

3.5.2 Wave Flume and Wave Generator

The Hydraulics Laboratory Wave Flume measures 20 m X 0.5 m X 0.75 m. An artificial beach is located at its downstream end. This beach is an essential component of the wave

flume as it helps in reducing the degree of wave reflection. During the experimental program, the water depth was maintained at 55 cm. (Depths above 65 cm are not recommended as there is a possibility of water spilling out of the flume.) Waves are produced by a single paddle wave generator located at upstream end of the flume. It is capable of generating both regular and random waves. This generator is controlled by a DEC VAXstation-3200 minicomputer using GEDAP† software developed by the National Research Council (NRC) of Canada. This generator is capable of producing waves of height up to 30 cm and a minimum period of 0.5 s. In the present investigation wave heights ranging from 6 cm to 16 cm are used. The range of wave periods used is 2.0 s to 3.0 s.

3.5.3 GEDAP Software

The GEDAP software was used extensively during all stages of the experimental investigation. GEDAP stands for GEneral purpose Data-acquisition and Analysis Program. This is a general purpose software package available on Digital Equipment Corporation's VAX computers for the analysis and management of laboratory data, including real-time experimental control and data acquisition functions. GEDAP is a fully-integrated, modular system which is linked together by a common data file structure. GEDAP maintains a standard data file format so that any GEDAP program is able to process data generated by any other GEDAP program. This package also includes an extensive set of data analysis programs so that most laboratory projects can be handled with little or no project-specific programming. The most rewarding feature of GEDAP is its fully-integrated interactive graphics capability, such that results can be conveniently examined at any stage of the data synthesis or analysis process. The GEDAP package also includes a vast collection of utility programs. These consist of data manipulation software routines, frequency domain analysis routines, and statistical and time-domain analysis routines. The RTC_SIG (Real Time

† GEDAP is a registered mark of the National Research Council of Canada.

Control - SIGnal generator) and RTC_DAS (Real Time Control - Data Acquisition System) are two important routines of this software package. The program RTC_SIG generates the control signal necessary to drive the wave paddle, while the routine RTC_DAS reads the data acquisition unit channels and stores the information in GEDAP binary format compatible with other GEDAP utility programs.

3.6 Experimental Procedure

3.6.1 Calibration of Potentiometers

Before carrying out the experiments, it is necessary to calibrate the potentiometers used to measure structural displacements. The calibration is carried out as described below.

The diameter of the pulley mounted on the potentiometer is measured. The pulley is then rotated through precisely 180 degrees and the resulting voltage across the potentiometer is measured. This procedure is repeated for four more steps of 180 degree rotation. A graph of the known displacement vs. measured voltage is then plotted. The slope of straight line fit is stored as the calibration factor for that particular potentiometer. The remaining two potentiometers are also calibrated in a similar fashion.

3.6.2 Wave Generator Signal File

The wave generator requires a signal file in order to generate waves of the desired wave height and period and the GEDAP program RWREP2 is used to create the corresponding signal file. This program requires four main input parameters, viz., wave generator calibration file, water depth, desired wave height and period. RWREP2 stores the computed driving signal in a format readable by the wave generator controller program RTC_SIG.

3.6.3 The Experiment

After setting up the box in the flume with the springs installed at desired separation, the water in the flume is allowed to calm down; the Data Acquisition System Channels are then initialized. After this initialization procedure, the GEDAP wave generation and data acquisition programs (RTC_SIG and RTC_DAS respectively) are invoked. The program RTC_SIG generates waves of desired height and period using an appropriate driving signal file, and the data acquisition program RTC_DAS reads the channels assigned to displacement probes and stores the data in a suitable format. After the desired duration RTC_SIG ramps down the wave generator motion. The RTC_DAS output data file is then de-multiplexed to separate the three wave probe measurements. These measurements are then transformed into displacements of the centre of gravity of the box using suitable transformation equations given in section 3.7.

3.7 Computation of Response

Surge, heave and pitch responses of the floating body are defined as the displacements of the centre of gravity in these three degrees of freedom. Since the wave probes do not measure the displacement of centre of gravity, a suitable set of transformation equations must be established to compute the response from the measurements.

Referring to Fig. 3.6, the equations relating the measured displacements d_1, d_2 and d_3 with surge, heave and pitch response, u_g, w_g, and θ respectively, are as follows:

$$d_1 = L_1 - \left\{ (u_g + A \sin\theta)^2 + (L_1 + A - w_g - A\cos\theta)^2 \right\}^{\frac{1}{2}} \qquad (3.15)$$

$$d_2 = L_2 - \left\{ (u_g - B/2 + R_2 \cos(\Delta_2-\theta))^2 + (L_2 + A - w_g - R_2 \sin(\Delta_2-\theta))^2 \right\}^{\frac{1}{2}} \qquad (3.16)$$

$$d_3 = L_3 - \left\{ (L_3 + B/2 - u_g + R_3 \cos(\Delta_3-\theta))^2 + (w_g - Z_{PI} + R_3 \sin(\Delta_3-\theta))^2 \right\}^{\frac{1}{2}} \qquad (3.17)$$

Eqs. (3.5)-(3.7) represent exact transformation equations. However, they are nonlinear and hence difficult to solve. Nevertheless, under certain conditions, these equations may be linearized.

If L_1, L_2, L_3 are sufficiently large compared to the measurements d_1, d_2, d_3 and responses u_g and w_g then eq. (3.15)-(3.17) may be linearized to:

$$d_1 = (w_g - A) + A \cos\theta \tag{3.18}$$

$$d_2 = (w_g - A) + R_2 \sin(\Delta_2 - \theta) \tag{3.19}$$

$$d_3 = u_g + R_3 \cos(\Delta_3 - \theta) \tag{3.20}$$

Solving for u_g, w_g, and θ:

$$\theta = -\sin^{-1}\left\{\frac{d_2 - d_1}{\mu}\right\} \tag{3.21}$$

and

$$w_g = d_1 + A\,(1 - \cos\theta) \tag{3.23}$$

$$u_g = d_3 + \frac{B}{2} - R_3 \cos(\Delta_3 - \theta) \tag{3.24}$$

where

$$m = \sqrt{(R_2 \sin\Delta_2 - A)^2 + (R_2 \cos\Delta_2)^2} \tag{3.22}$$

Eqns. (3.21)-(3.24) may now be used to evaluate the *pitch*, *heave* and *surge* responses respectively. The linearized surge, heave and pitch responses are found to be quite acceptable for further analysis. The above equations have been derived in detail in Appendix A.

Chapter 4

Results and Discussion

This chapter describes the results obtained from the experiments. The results have been presented in the form of time series, phase portraits and Fourier spectra. Due to the immense storage requirement, a Poincaré map is drawn for one measured time series only. The largest Lyapunov exponents have been computed for all experimental time series.

4.1 Time Series, Phase Portraits and Spectra

The time series, phase portrait and Fourier spectrum are the most important qualitative tests used in detecting chaos in nonlinear systems and these are shown in Fig. 4.1 for the surge response corresponding to T = 2.5 s, H = 13 cm and K = 4.25. The time series shown in Fig. 4.1a appears to be chaotic and the corresponding phase portrait shown in Fig. 4.1b also suggests that the system behaviour is not periodic. Fig. 4.2 shows corresponding results for the case in which the incident wave height is increased by 2 cm and indicates that a drastic change in surge response occurs. In particular, the time series in Fig. 4.2a that, the system behaviour has changed from non-periodic to periodic; and the corresponding Fourier spectrum shown in Fig. 4.2c is now composed of peaks at integral multiples of incident wave frequency, confirming the periodic nature of the response.

Fig. 4.3 shows results for H = 14 cm, T = 2.5 s, a = 0.423, K = 4.25 and d_g = 11.5 cm. These results show an interesting phenomenon in that there is a sudden change in response

characteristics from non-periodic to periodic. Such a phenomenon is called *transient chaos*. Initially the motion appears to be quite irregular but soon settles down to a periodic response.

Figs. 4.4 - 4.7 show effect of wave period variation on surge response. The incident wave period is varied while maintaining the other controlling parameters constant. Fig. 4.4, which corresponds to H = 13 cm and T = 2.0 s, exhibits some sub-harmonic response. When the incident wave period was increased by 0.2 s, a significant spectra peak at 1/4th of incident wave frequency appears as shown in Fig. 4.5d. Phenomenon of transient chaos can be observed for a wave period of 2.8 s. The response is changed from non-periodic to periodic after about 250 s (Fig. 4.6). Fig. 4.7 shows time series, phase portrait and Fourier spectra for T = 3.0 s. The observed response is periodic. The phase portrait is nearly a closed loop and the Fourier spectrum is composed of spectral peaks at integral multiples of incident wave frequency, thus confirming periodic nature of the response.

For an incident wave with H = 11 cm and T = 2.8 s very significant sub-harmonic response is observed. The time series shown in Fig. 4.8 clearly indicates presence of multiple frequency components. In addition to a peak at the incident wave frequency, a significant second peak is observed at 1/3rd of the incident frequency. A very periodic response is observed for H = 15 cm and T = 2.8 s (Fig. 4.9). No sub-harmonic response is observed in this case.

Some sub-harmonic response is observed for H = 11 cm and T = 2.0 s as shown in Fig. 4.10. A very significant sub-harmonic spectral peak is observed for H = 11 cm and T = 2.2 s (Fig. 4.11).

Both chaotic and periodic/sub-harmonic responses were observed for bichromatic wave excitation. Ten experiments were conducted to study the model's response to bichromatic waves. The observed response to $H_1 = H_2 = 7$ cm, $T_1 = 2.2$ s and $T_2 = 2.5$ s is very non-

periodic (Fig. 4.12). A considerable sub-harmonic response is observed in this case. The spectra shows a number of sub-harmonic peaks at multiples of the incident wave period. Considerably more sub-harmonic response is observed for bichromatic waves than for the monochromatic wave excitation. Fig. 4.13 shows an example of the periodic response for bichromatic excitation.

4.2 Effect of Wave Height

The wave height appears to be an important governing parameter of the system behaviour. Tests with four different wave heights (11, 12, 13, 14 and 15 cm) were carried out, while maintaining a constant wave period (2.5 s) and the other controlling parameters held constant. Fig. 4.14 shows the effect of various wave heights on the surge response. Chaotic motion was observed for wave heights of 12 and 13 cm, whereas for heights of 11 and 14 cm the observed motion was periodic, as is evident from Fig. 4.14. For a wave height of 11 cm, hardly any spring action was observed. This phenomenon could be attributed to the fact that the incident wave had insufficient energy to produce required surge to cover the gap width so that no chaotic motion was observed. For a wave height of 14 cm, the observed response was completely periodic, as if the system was linear. This observation may be explained as follows. Since, the total energy of a regular sinusoidal wave is proportional to the wave height cubed, the 14 cm wave has more energy by a factor of two than the one with 11 cm wave height. Hence, the 14 cm wave produced enough surge to cover the gap width. For wave heights between 11 and 14 cm, intermittent contact with springs was observed and the resulting response was very aperiodic.

4.3 Effect of Wave Period

Wave period was also observed to have a similar effect as the wave height on the surge response. Figure 4.15 shows surge response time series for various values of incident wave period T. The wave height (13 cm) and the other system parameters were kept constant. For an incident wave with wave period of 2.0 s, the observed response was relatively periodic and hardly any spring action was observed. In this case, the wave period was not sufficient enough to produce horizontal displacement comparable to the gap width. Hence, spring action was absent and so was the chaotic motion. On the other hand, the surge response for wave period of 3.0 s was very periodic with full spring action. The system behaviour appeared to be very linear. The gap width had hardly any effect on the response. This may also be explained by applying the same logic as in the previous case. The incident wave in this case induced sufficient horizontal displacement to produce enough restoring force resulting in periodic system behaviour. In the intermediate case with wave period of 2.5 s, the spring action was intermittent and the system behaviour appeared very non-periodic.

4.4 Effect of Spring Stiffness and Gap Width

A wider gap width was observed to produce a slight drift in the equilibrium position. At the end of the experiment, the floating box was observed to come to rest not at its initial position but a different position in the downstream direction. For example, for a gap with of 14 cm, the observed drift was of the order of 10 cm. Interestingly, no appreciable drift was observed for gap width of 7 cm. Fig. 4.16 shows a plot of response amplitude vs. gap width. It can be seen from the graph that, the response amplitude falls sharply with increase in the gap width.

Spring stiffness also was observed to be an important factor in deciding the surge response characteristics. It was observed that for lower values of frequency ratio (α) the response tends to be periodic. For higher values of α some sub-harmonic response was observed.

4.5 Non-dimensional Plots

Fig. 4.17 - 4.19 show plots of the non-dimensional response as a function of various non-dimensional input parameters, viz., wave height, wave period, frequency ratio and gap width.

Fig. 4.17 is a graph of R/H vs. B/gT^2. Chaotic response was observed for B/gT^2 between 0.012 and 0.020. For smaller values of B/GT^2 (or larger values of wave period) response was periodic.

Fig. 4.18 is a plot of R/gT^2 vs. B/H. As can be seen from the plot, chaotic response was observed for values of B/H lying between 5.5 and 6.5. Response was periodic beyond this range of B/H.

Frequency ratio α has been observed to be one of the very important deciding factors of the system behaviour. As is clear from fig. 4.19, chaotic response was observed for values of α between 0.4 and 0.6. For α below 0.4, the response was periodic. This is in confirmation with the numerical prediction of Aoki, Sawaragi and Isaacson (1993).

4.6 Poincaré Map

As indicated in Chapter 2, the Poincaré map is a discrete time view of a continuous phase portrait. In order to observe a fractal-like structure of a strange attractor on a Poincaré map,

a very long response time series is needed. In numerical experiments, it is possible to obtain response time series of any required length, although in physical tests this may not always be feasible owing to experimental limitations. For example, in present case, due to immense disk space requirement, only one time series of 40 min length was measured. The largest Lyapunov exponent for this particular time series is positive indicating chaos. Fig. 4.20 - 4.22 show Poincaré maps for various values of "phase". Strange attractor is visible in Fig. 4.20(a). Fig. 4.20(b) shows two distinct patches indicating presence of two dominant frequency components (Moon, 1987). On the other hand, a Poincaré map of periodic response lacks any fractal structure. Points tend to concentrate in certain regions of the phase space unlike the case of a Poincaré map of chaotic response. Finally, positive Lyapunov exponent confirms the chaotic nature of the former response.

4.7 Lyapunov Exponent

Lyapunov exponents are of interest in the study of dynamic systems in order to characterize quantitatively the average exponential divergence or convergence of nearby trajectories. Since, they can be computed either from a mathematical model or from experimental data, they are widely used for the classification of attractors. Negative or zero Lyapunov exponents signal periodic orbits, while at least one positive exponent indicates chaotic orbit. and divergence of initially neighboring trajectories.

Computation of all Lyapunov exponents is computationally very demanding. As a matter of fact, one doesn't need all the Lyapunov exponents to decide whether the system behaviour is periodic or chaotic, because presence of a single positive Lyapunov exponent is sufficient enough evidence to declare the motion as chaotic. Hence in reality, one needs only the largest Lyapunov exponent. Various numerical algorithms have been proposed in literature to compute the largest Lyapunov exponent. An algorithm developed by Wolf et al.

(1985) is used in the present investigation. Wolf et. al. have also given a computer program based on their algorithm.

4.7.1 Fixed Evolution Time Program for λ_1

A time series of given duration is read from a data file, along with the parameters necessary to reconstruct the attractor, viz., the dimension of the phase space reconstruction, the reconstruction time delay and the time between data samples, required for normalization of the exponent. Three other input parameters are required: length scales that we consider to be too large and too small and a constant propagation time between replacement attempts. We also supply a maximum angular error to be accepted at replacement time, but it is not considered as a free parameter as its selection is not likely to have much effect on exponent estimates. It is usually fixed at 0.2 or 0.3 radians.

The calculation is initiated by carrying out an exhaustive search of the data file to locate the nearest neighbor to the first point (also known as the *fiducial point*), omitting points closer than a pre-assigned minimum distance. The main program loop, which carries out repeated cycles of propagating and replacing the principal axis is now entered. The current pair of points is propagated through a preset evolution steps through the attractor and its final separation is computed. The logarithm of the ratio of final to initial separation of this pair updates a running average rate of orbital divergence. A replacement step is then attempted. The distance of each delay coordinate point to the evolved fiducial point is then determined. Points closer than certain minimum but further away than certain maximum distance, are examined to see if the change in angular orientation is less than maximum allowable angular orientation. If more than one candidate point is found, the point defining the smallest angular change is used for replacement. If no points satisfy these criteria, we loosen the larger distance criterion to accept replacement points as far as twice the maximum allowable distance. If necessary the large distance criterion is relaxed several more times, at

which point we tighten this constraint and relax the angular acceptance criterion. Continued failure will eventually result in our keeping the pair of points we had started out with, as this pair results in no change whatsoever in phase space orientation. We now go back to the top of main loop where new points are propagated. This process is repeated until the fiducial trajectory reaches the end of the data file, by which time we hope to see stationary behaviour of λ_1.

This computer program was used to compute the largest Lyapunov exponents from experimental time series. It has been observed (Wolf et. al., 1985) that attractors reconstructed using smaller values of dimension (m) often yield reliable Lyapunov exponents. Hence, m was chosen to be equal to 3 in this case. The time series in present case is practically noise-free, hence the largest and smallest length scales may be chosen arbitrarily. The reconstruction time delay (τ) is chosen neither so small that the attractor stretches out, nor so large that $m\tau$ is much larger than the orbital period. The reconstruction time delay in present case is chosen equal to the mean orbital period. Decisions about propagation times and replacement steps depend upon additional input parameters or on the operator's judgment. Too frequent replacements cause a dramatic loss of phase space orientation, and too infrequent replacements allow volume elements to grow overly large and exhibit folding. It has been recommended that the evolution time in the range of 1/2 to 3/2 orbits almost always provides stable exponent estimates. In the present case an evolution time of 1/2 the mean orbital period is used. In order to make sure that the Lyapunov exponent computed by the program is reasonable, the program is fed with a perfectly periodic time series having the same period as the observed experimental time series and approximately the same average amplitude. A combination of program input parameters giving zero Lyapunov exponent value is then used as parameters for the experimentally measured time series. This initialization procedure makes sure that the Lyapunov exponent is indeed the one which is being sought for. Tables 4.1 and 4.2 give the largest Lyapunov exponents computed using the above program.

Chapter 5

Conclusion and Scope for Further Research

As mentioned earlier, the primary aim of this study was to demonstrate chaos experimentally in nonlinearly moored offshore structures. Experiments were carried out on a hollow plywood box of size 76 cm x 20 cm x 25 cm. Two aluminum cantilever beams were used to model nonlinear spring action. The motion of the model was restricted to three degrees of freedom only, viz., surge, heave and pitch. Displacement measurements at three different locations on the body were made using potentiometers mounted on a rigid aluminum frame, with a system of strings, pulleys and counter-weights used to transmit the structure motions to potentiometers. Measured displacements were transformed to provide surge, heave and pitch motions with respect to the centre of gravity of the structure. From the analysis of the experimental data, it appears that the goal has been achieved.

Wave height, wave period, spring stiffness and gap width dictate the behaviour of the system. For a certain range of wave height and period, the observed response is chaotic. The effect of gap width is in general coupled with the other parameters. If the other three quantities are held constant, a wider gap width is more likely to generate chaotic response than a narrower one, as a reduction in the gap width causes a corresponding decrease in the system's nonlinearity. In addition to chaotic response, a sub-harmonic response was observed in some cases. Interestingly, for particular threshold values of wave height and period, a sudden transition from chaotic to periodic response is observed. This phenomenon has been referred to in literature as *transient chaos*. It would be of interest to investigate this

transition phenomenon in more detail. Further research effort in this area may lead to a better understanding of the parameters responsible for occurrence of this phenomenon.

Lyapunov exponents appear to offer the most suitable quantitative estimate of chaos such that presence of even a single positive Lyapunov exponent is sufficient evidence to declare the motion as chaotic. As mentioned earlier, Wolf's computer program for estimating the largest Lyapunov exponent has been tested with a perfectly periodic time series, and was then used with the experimental time series. The presence of positive Lyapunov exponents in some of these tests confirm the chaotic response.

In the previous numerical study conducted by Aoki, Sawaragi and Isaacson (1993), a single degree of freedom model (surge) was developed, whereas the study reported here deals with a three degrees of freedom model (surge, heave and pitch). It would be useful use the mathematical formulation developed (Appendix B) to compare the numerical results to the experiments and to study the effects of the other two degrees of freedom on the surge response by comparing such results with those of the single degree of freedom model. The present work deals only with geometrical nonlinearity. As an extension to this work, one could study the effect of material nonlinearity on response of the floating box which has not been studied here.

Application of chaotic dynamics to ocean structures is still in a developmental stage. Much can be done in this new area of ocean engineering. The present case is a very idealized case of geometric nonlinearity. Geometric stiffness characteristics of catenary moorings are somewhat different than the case considered here. Careful numerical and prototype experiments performed taking into account the catenary effects may shed additional light on this phenomenon.

References

Aoki, S. I., Sawaragi, H., and Isaacson, M. (1993) "Wave-Induced Low Frequency Motions of Compliant Offshore Structures with Nonlinear Moorings", *Proceedings of the 3rd International Offshore and Polar Engineering Conference*, Singapore, June, **1**, pp. 369-376.

Bishop, S. R. and Virgin, L. N. (1987) "The Onset of Chaotic Motions of a Moored Semi-Submersible, *Proceedings of 6th International Offshore Mechanics and Arctic Engineering Conference,* Houston, **2**, pp. 319-323.

Bishop, S. R. and Virgin, L. N. (1988) "Catchment Regions of Multiple Dynamic Responses in Nonlinear Problems of Offshore Mechanics", *Proceedings of 7th International Offshore Mechanics and Arctic Engineering Conference*, Houston, **2**, pp. 15-22.

Chirikov, B. V. (1979) "A Universal Instability of Many Dimensional Oscillator Systems", *Phys. Reps.*, **52**, pp. 263-379.

Ford, J. (1975) "The Statistical Mechanics of Classical Analytic Dynamics", In *Fundamental Problems in Statistical Mechanics*, E. G. D. Cohen (ed), North-Holland, Amsterdam, **3**, pp. 215-255.

Gottlieb, O. and Yim, S. C. S. (1990) "Onset of Chaos in a Multi-point Mooring System", *Proceedings of the First European Offshore Mechanics Symposium*, Trondheim, Norway, pp. 6-12.

Kapitaniak, T. (1991) *Chaotic Oscillations in Mechanical Systems*, Manchester University Press, Manchester, U.K.

Lau, S. L.; Ji, Z. and Ng, C. O. (1990) "Dynamics of an Elastically Moored Floating Body by the Three-Dimensional Infinite Element Method", *Ocean Engineering*, **17**, No. 5, pp. 499-516.

Lorenz, E. N. (1963) "Deterministic Nonperiodic Flow", *Journal of Atmospheric Science*, **20**, 130-41.

Miles, M. D. (1989) "Guide to Using GEDAP on VAX/VMS", Hydraulics Laboratory, *National Research Council of Canada*, Ottawa, Canada.

Moon, F. C. (1987) *Chaotic Vibrations: An Introduction for Scientists and Engineers*, John Wiley & Sons, New York.

Oseledec, V. I. (1968) "A Multiple Ergodic Theorem: Lyapunov Characteristics for Dynamical Systems", *Transactions of Moscow Mathematical Society*, **19**, pp. 197-231.

Papoulias, F. A. and Bernitsas, M. M. (1988) "Autonomous Oscillations, Bifurcations, and Chaotic Response of Moored Vessels", *Journal of Ship Research,* **32**, No. 3, pp. 220-228.

Parker, T. S., and Chua, L. O. (1989) *Practical Numerical Algorithms for Chaotic Systems*, Springer-Verlag, New York.

Poincaré, H. (1890) "Sur les équations de la dynamique et le problème de trois corps.", *Acta Math.*, **13**, 1-270

Poincaré, H. (1898) *Les Methodes Nouvelles de la Méchanique Celeste*, **1-3**, Gauthier-Villars, Paris.

Sumanuskajonkul, S and Hu, S. James (1992) "Responses of Bilinear and Impacting Systems Subjected to Regular Waves", *Proceedings of 9th Conference on Engineering Mechanics*, ASCE, NY, pp. 196-199.

Sarpkaya, T. and Isaacson, M. (1981) *Mechanics of Wave Forces on Offshore Structures*, Van Nostrand Reinhold Company, New York.

Schuster, Heinz G. (1988) *Deterministic Chaos: An Introduction*, VCH Verlaggesellschaft mbH, Weinheim, FRG.

Ueda, Y. (1979) "Randomly transitional phenomenon in the system governed by Duffing's equation", *Journal of Statistical Physics*, **20**, pp. 181-196.

Wolf, A., Swift, J. B., Swinney, H. L., and Vastano, J. A. (1985) "Determining Lyapunov Exponents from a Time Series", *Physica,* **16D,** North-Holland, Amsterdam, pp. 285-317.

Wolf, A. (1986) "Quantifying Chaos with Lyapunov Exponents", *Nonlinear Science: Theory and Applications*, ed. A. V. Holden, Manchester University Press, pp. 273-290

Yim, S. C. S. and Lin, H. (1991) "Chaotic and Stochastic Dynamics of Offshore Equipment", *Proceedings of the First International Offshore and Polar Engineering Conference*, Edinburgh, U.K., **3**, pp. 420-427.

Appendix - A

Transformation Equations

The displacement probes measure displacement of three different points on the floating body. The surge, heave and pitch responses of the floating body are defined as the displacements of its centre of gravity in these three degrees of freedom. The present experimental setup does not allow the surge, heave and pitch response to be measured directly. Hence it is necessary to transform these displacements from their present points of measurement to the centre of gravity. These equations may be derived as shown below.

Let d_1 be the potentiometer reading at time t corresponding to displacement probe #1. Referring to Fig. A-1, we can express d_1 in terms of L_1 and L_1' as,

$$d_1 = L_1 - L_1' \tag{A1}$$

L_1' may itself be expressed in terms of u_g, w_g and θ as

$$L_1' = \sqrt{(u_g + A \sin\theta)^2 + (L_1 + A - w_g - A \cos\theta)^2} \tag{A2}$$

Substituting in equation (A1):

$$d_1 = L_1 - \sqrt{(u_g + A \sin\theta)^2 + (L_1 + A - w_g - A \cos\theta)^2} \tag{A3}$$

similarly, referring to Figs. (A2) and (A3), corresponding expressions for d_2 and d_3 are

$$d_2 = L_2 - \sqrt{[u_g - B/2 + R_2 \cos(\Delta_2 - \theta)]^2 + [L_2 + A - w_g - R_2 \sin(\Delta_2 - \theta)]^2} \tag{A4}$$

and

$$d_3 = L_3 - \sqrt{[w_g - Z_{PI} + R_3 \cos(\Delta_3 - \theta)]^2 + [L_3 + B/2 - u_g - R_3 \sin(\Delta_3 - \theta)]^2} \qquad \text{(A5)}$$

Equations (A3), (A4) and (A5) in their present form are difficult to solve due to the presence of nonlinearity. Attempts to solve these equations failed as the solution procedure produced very unstable results. A closed-form solution of linearized equations is a possibility. Following assumptions are involved in the linearization procedure.

- lengths L_1, L_2 and L_3 are sufficiently large compared to u_g and w_g
- Angle θ is small compared to Δ_2 and Δ_3

Using above assumptions, equations (A3), (A4) and (A5) may be linearized to:

$$d_1 = L_1 - (w_g - A) + A \cos\theta \qquad \text{(A6)}$$

$$d_2 = L_2 - (w_g - A) + R_2 \sin(\Delta_2 - \theta) \qquad \text{(A7)}$$

$$d_3 = u_g - R_3 \sin(\Delta_3 - \theta) - \frac{B}{2} \qquad \text{(A8)}$$

Equations (A6)-(A8) can be solved for u_g, w_g and θ. Hence we get,

$$\theta = -\sin^{-1}\left\{\frac{d_2 - d_1}{\mu}\right\} \qquad \text{(A9)}$$

where, $\mu = \sqrt{(R_2 \sin\Delta_2 - A)^2 + (R_2 \cos\Delta_2)^2}$ and similarly ,

$$w_g = d_1 + A - A\cos\theta \qquad \text{(A10)}$$

$$u_g = d_3 + \frac{B}{2} - R_3 \sin(\Delta_3 - \theta) \qquad \text{(A11)}$$

In order to assess appropriateness of linearization, the linearized values of u_g, w_g and θ were substituted back into the exact equations and new values of d_1, d_2 and d_3 were obtained. The new values were then compared with the original d_1, d_2 and d_3 values as shown in Fig.

(A-4), (A-5) and (A-6). Evidently, the comparison is quite good especially for the displacement probe #3. Hence, we can conclude that, u_g, w_g and θ obtained from the linearized equations can be used in subsequent development of the problem without sacrificing accuracy.

Appendix B

Mathematical Formulation of Hydrodynamic Coefficients

A numerical approach to the present problem requires an initial calculation of added mass, hydrodynamic damping coefficients and wave forces. Once these hydrodynamic coefficients are known, the response may then be obtained by solving the nonlinear equations of motion in the time domain using an appropriate time-stepping procedure. The following paragraphs briefly describe the procedure involved.

Fig. B-1 shows a definition sketch of a moored two-dimensional floating body of arbitrary shape, while Fig. B-2 shows a corresponding mathematical model of this body. Two coordinate systems are defined. O-X-Z and G-X'-Z' are *fixed* and *moving* coordinate systems respectively, as indicated in Fig. B-1. The origin O of the fixed system is defined as the point of intersection of SWL and the vertical through G when the body is in its equilibrium position. The origin G of the moving system is the centre of gravity of the body. Note that in the equilibrium position Z and Z' axes overlap.

The equation of motion for the moored two-dimensional body may be written as

$$[M]\{\ddot{\xi}\} + [\lambda]\{\dot{\xi}\} + [K(\xi)]\{\xi\} = F(t) \qquad \text{(B-1)}$$

Where [M], [λ] and [K(ξ)] are the mass, damping and stiffness matrix respectively. It may be noted that, equation (B-1) is a nonlinear equation since the stiffness matrix is a function of the displacement {ξ}. The excitation F(t) may be computed from linear diffraction theory. The system properties, viz., the added mass [μ], damping matrix [λ], mass matrix [M], and the stiffness matrix [K] can be individually evaluated.

The evaluation of incident wave force F(t) is quite classical. This incident wave force may be easily computed using linear diffraction theory. Since the problem is linear, the velocity potential can be represented as a sum of three separate components.

$$\phi = \phi_w + \phi_s + \phi_f \tag{B-2}$$

where, ϕ_w, ϕ_s, and ϕ_f are the incident, scattered and forced velocity potentials respectively. These three components separately satisfy the Laplace equation, together with the bottom and free surface boundary conditions, and ϕ_s, ϕ_f must also satisfy the radiation condition.

The boundary condition at the body surface must account for the velocity of the body itself and is given by,

$$\frac{\partial \phi_w}{\partial n} + \frac{\partial \phi_s}{\partial n} + \frac{\partial \phi_f}{\partial n} = V_n \tag{B-3}$$

where V_n is the velocity of the body surface in the direction 'n' normal to itself. Since, the motions are small, this condition is applied at the equilibrium surface S_o taken at the rest position, rather than at the instantaneous position. Equation (B-3) may be broken down into two equations

$$\frac{\partial \phi_w}{\partial n} + \frac{\partial \phi_s}{\partial n} = 0 \qquad \text{at } S_o \tag{B-4}$$

as in a fixed body case, together with,

$$\frac{\partial \phi_f}{\partial n} = V_n \qquad \text{at } S_o \tag{B-5}$$

The problem defining ϕ_s is identical to that for the fixed body case and ϕ_s thus may be determined in exactly the same way as the fixed body case. Many a times, ϕ_s is not needed explicitly since it will be possible to express the wave forces directly in terms of ϕ_f.

The velocity V_n is the velocity of the body surface in the direction. Hence, we may write,

$$V_n = \sum_{j=1}^{3} \frac{\partial \phi_f}{\partial t} n_j \tag{B-6}$$

where, n_j is given as, $n_1 = n_x$, $n_2 = n_z$ and $n_3 = xn_z - zn_x$. n_x, n_z are the direction cosines of the normal to the surface. In order to apply the boundary conditions, it is convenient to decompose ϕ_f into three components associated with each degree of freedom and each proportional to displacement amplitude ξ_j. Hence, we may write

$$\phi_f = \sum_{j=1}^{3} \xi_j \, \phi_j^{(f)} \tag{B-7}$$

The coefficients $\phi_j^{(f)}$ are generally complex. This representation enables the body surface boundary conditions to be written in terms of $\phi_j^{(f)}$ and independent of ξ_j as,

$$\frac{\partial \phi_j^{(f)}}{\partial n} = -i\omega n_j \qquad \text{on } S_o \qquad j=1,..3 \tag{B-8}$$

The right-hand-sides of these equations are known and the three functions may be found in the same manner as is the scattered potential ϕ_s.

The forces and moments associated with ϕ_w and ϕ_s comprise the exciting force $F^{(e)}$ on the body. Application of Green's theorem makes it possible to express the exciting force directly in terms of the incident and forced potentials. Such expressions are called Haskind relations. They may be given in the form

$$F_i^{(e)} = \rho \int_{S_o} \left[\phi_w \frac{\partial \phi_i^{(f)}}{\partial n} - \phi_i^{(f)} \frac{\partial \phi_w}{\partial n} \right] dS \tag{B-9}$$

Hence, one can evaluate $F_i^{(e)}$ from the knowledge of $\phi_i^{(f)}$ calculated to obtain the added-mass and damping coefficients.

There are three components $F_i^{(f)}$ corresponding to each mode motion, and each of these may be written as (Sarpkaya and Isaacson, 1981),

$$F_i^{(f)} = \rho \int_{S_o} \frac{\partial \phi_f}{\partial t} n_i \, dS = -i\omega\rho \sum_{j=1}^{3} \left(\int_{S_o} \phi_j^{(f)} n_i \, dS \right) \xi_j \qquad \text{(B-10)}$$

Above equation may be decomposed into components in phase with the velocity and the acceleration of each mode and we put

$$F_i^{(f)} = - \sum_{j=1}^{3} \left(\mu_{ij} \frac{\partial^2 \xi_j}{\partial t^2} + \lambda_{ij} \frac{\partial \xi_j}{\partial t} \right) \qquad i=1,..3 \qquad \text{(B-11)}$$

where the coefficients μ_{ij} and λ_{ij} are taken as real and are called the *added mass* and *damping coefficient* respectively. Hence the rearranged equation of motion may be written as

$$(m_{ij} + \mu_{ij}) \frac{\partial^2 \xi_j}{\partial t^2} + \lambda_{ij} \frac{\partial x_j}{\partial t} + K_{ij} \xi_j = F_i^{(e)} \qquad \text{(B-12)}$$

In the above equation λ_{ij} represents only the hydrodynamic damping. In cases where structural damping or viscous damping are important, these would need to be included in additional terms alongside the λ_{ij} terms. Likewise $F_i^{(e)}$ represents only the force due to wave field, and if external forces are present these would need to be included alongside $F_i^{(e)}$. Application of the body surface boundary condition gives following explicit expressions for the added mass and damping coefficients

$$\mu_{ij} = \frac{\rho}{\omega} \int_{S_o} \mathrm{Im}[\phi_j^{(f)}] \, n_i \, dS \qquad \text{(B-13)}$$

$$\lambda_{ij} = -\rho \int_{S_o} \mathrm{Re}[\phi_j^{(f)}]\, n_i \, dS \tag{B-14}$$

Now a consequence of Green's theorem is that the added mass and damping coefficients are symmetric. Finally, it should be noted that both the added mass and damping coefficients are frequency dependent.

Solution of the linearized diffraction problem always results in the wave elevation η of the form

$$\eta(t) = A \cos(\omega t) \tag{B-15}$$

where, A is the wave amplitude. Hence, the exciting force corresponding to $\eta(t)$ may be written as

$$F(t) = A\, F^*(t) \cos(\omega t + \delta(\omega)) \tag{B-16}$$

where, $F^*(\omega)$ is a transfer function of the first order exciting force and $\delta(\omega)$ is the phase lag between $\eta(t)$ and F(t), both of which may be obtained using linear diffraction theory.

For a bichromatic wave train with frequency components ω_1 and ω_2, the free surface elevation my be expressed as

$$\eta(t) = A_1 \cos(\omega_1 t) + A_2 \cos(\omega_2 t + \varepsilon) \tag{B-17}$$

where, A_1 and A_2 are the two component amplitudes, ω_1 and ω_2 are the component frequencies and ε is the phase difference between the two components. The corresponding exciting force F(t) may be written in the form

$$F(t) = A_1 F_1^* \cos(\omega_1 t + \delta(\omega_1)) + A_2 F_1^*(\omega_2) \cos(\omega_2 t + \varepsilon + \delta(\omega_2)) +$$

$$A_1 A_2 \frac{1}{2} \rho g\, C_d \left(\frac{\omega_1 + \omega_2}{2}\right) \cos\Big((\omega_1 - \omega_2)t - \varepsilon + \delta_L(\omega_1, \omega_2)\Big) \tag{B-18}$$

Where $C_d(\omega)$ is the steady drift coefficient which may be obtained from the results of linear diffraction theory. In a particular case of component wave having same amplitude and phase, $A_1 = A_2 = A$ and $\varepsilon = 0$, the wave exciting force F(t) given by Eq. (B-18) may be simplified to:

$$F(t) = 2AF^*(\omega)\cos\left(\frac{\Delta\omega t}{2}\right)\cos(\omega t + \delta(\omega)) + \frac{1}{2}\rho g A^2 C_d(\omega)\cos(\Delta\omega t) \qquad \text{(B-19)}$$

where, $\omega = (\omega_1 + \omega_2)/2$ as before and $\Delta\omega = \omega_1 - \omega_2$.

The mass matrix for the problem can be easily set by lumping masses corresponding to the three degrees of freedom, viz., surge, heave and pitch respectively. Hence we can write,

$$[m] = \begin{bmatrix} m & 0 & 0 \\ 0 & m & 0 \\ 0 & 0 & I \end{bmatrix} \qquad \text{(B-20)}$$

Here, m is the mass of the floating body and I is the mass moment of inertia of the body about the axis passing through the centre of gravity. The total mass matrix is the sum of real and added mass matrix. Hence, we may write $[M] = [m] + [\mu]$

The restoring force on the body is developed as a result of the combined effect of mooring stiffness and hydrostatic effect. Stiffness characteristic of the spring is as shown in Fig. B-3. Note that, the spring action becomes effective only after certain displacement d_s of the body. Hence, the spring stiffness matrix $K_S(\xi)$ may be written as,

$$K_S(\xi) = \left\{ \begin{array}{ll} k_1 & \xi \le d_g \\ 0 & -d_g \le \xi \le d_g \\ k_2 & \xi \ge d_g \end{array} \right\} \qquad \text{(B-21)}$$

Hence, the total stiffness matrix [K] due to combined contribution from spring effects and hydrostatics may be given as:

$$[K] = [K_H] + \delta(\xi)\,[K_S] \tag{B-22}$$

Where, δ is the well known *Kronecker delta function* defined as

$$\delta(\xi) = \left\{ \begin{array}{ll} 0 & \text{if } \xi \leq d_s \\ 1 & \text{if } \xi > d_s \end{array} \right\} \tag{B-23}$$

A detailed derivation of $[K_H]$ and $[K_S]$ may be found in Lau et. al. (1990). It should however be noted that, due to presence of nonlinearity in the stiffness term, a compatibility condition must be satisfied at all times. Equation (B-1) may now be solved using a suitable time stepping procedure to obtain the response $\{\xi\}$.

Load P (N)	Deflection (cm)	Calculated Deflection
12.29	0.8	0.75
24.58	1.5	1.5
36.88	2.1	2.3
49.17	2.8	3.0

Table 3.1 - Measured and calculated load-deflection values for spring #4

Spring #	Width (mm)	Thickness (mm)	MI (mm^4)	Stiffness (N/m)
1	50	6	900.00	251.88
2	63	6	1134.00	317.37
3	76	6	1386.00	382.86
4	63	9	3827.25	1071.12

Table 3.2 - Spring characteristics

Test No.	H (cm)	T (sec)	α	K	d_g (cm)	Lyapunov Exponent
1	13	2.5	0.423	4.25	11.5	-0.4567
2	11	2.5	0.423	4.25	11.5	-0.0499
3	12	2.5	0.423	4.25	11.5	-0.5570
4	14	2.5	0.423	4.25	11.5	0.0622
5	15	2.5	0.423	4.25	11.5	0.1276
6	13	2.0	0.529	4.25	11.5	-0.1293
7	13	2.2	0.481	4.25	11.5	-0.9745
8	13	2.8	0.378	4.25	11.5	-0.0143
9	13	3.0	0.353	4.25	11.5	-0.8034
10	11	2.8	0.378	4.25	11.5	-0.1795
11	15	2.8	0.378	4.25	11.5	-0.0985
12	11	3.0	0.353	4.25	11.5	-0.5016
13	11	2.0	0.529	4.25	11.5	-0.2330
14	15	2.0	0.529	4.25	11.5	0.1180
15	11	2.2	0.481	4.25	11.5	0.5998
16	15	2.2	0.481	4.25	11.5	0.4185
17	13	2.5	0.708	1.00	11.5	0.2448
18	13	2.5	0.778	1.00	11.5	-0.3956
19	13	2.5	0.873	1.00	11.5	-0.2724
20	13	2.5	0.423	1.00	11.5	-0.0487
21	13	2.5	0.423	4.25	7.0	-0.1740
22	13	2.5	0.423	4.25	14.0	0.0271

Table 4.1 - Input parameters and Lyapunov exponents - monochromatic excitation

Test No.	H_1 (cm)	H_2 (cm)	T_1 (s)	T_2 (s)	α	K	Lyapunov Exponent
1	7.0	7.0	2.3	2.7	0.423	4.25	0.880
2	7.0	7.0	2.0	3.0	0.423	4.25	0.519
3	8.0	8.0	2.0	3.0	0.423	4.25	-0.557
4	8.0	8.0	2.2	2.8	0.423	4.25	-0.451
5	9.0	9.0	2.2	2.8	0.423	4.25	-
6	7.0	7.0	2.3	2.7	0.778	1.0	0.028
7	7.0	7.0	2.0	3.0	0.778	1.0	0.616
8	8.0	8.0	2.0	3.0	0.778	1.0	-0.358
9	8.0	8.0	2.2	2.8	0.778	1.0	0.206

Table 4.2 - Input parameters and Lyapunov exponents - bichromatic excitation

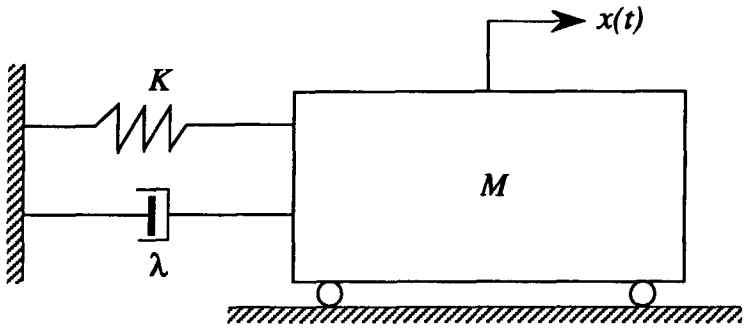

Fig. 2.1 Idealization of the classical spring-mass-dashpot oscillator

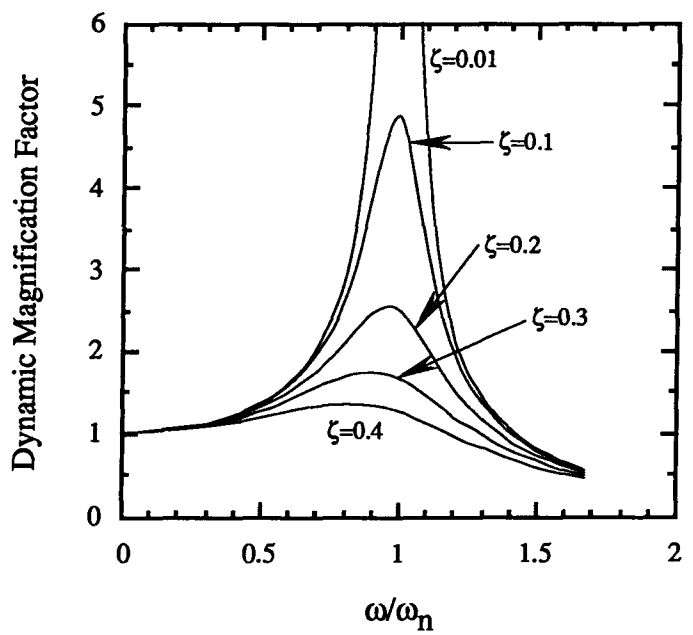

Fig. 2.2 Classical resonance curves of a linear single degree of freedom system

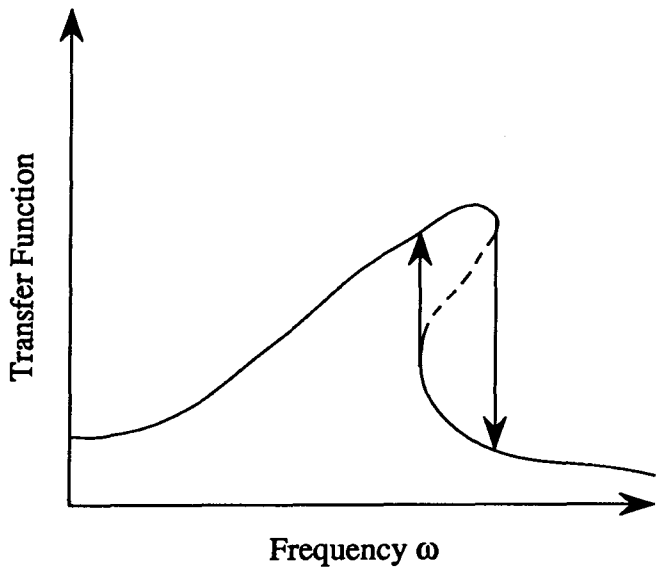

Fig. 2.3 Classical resonance curve for a nonlinear oscillator

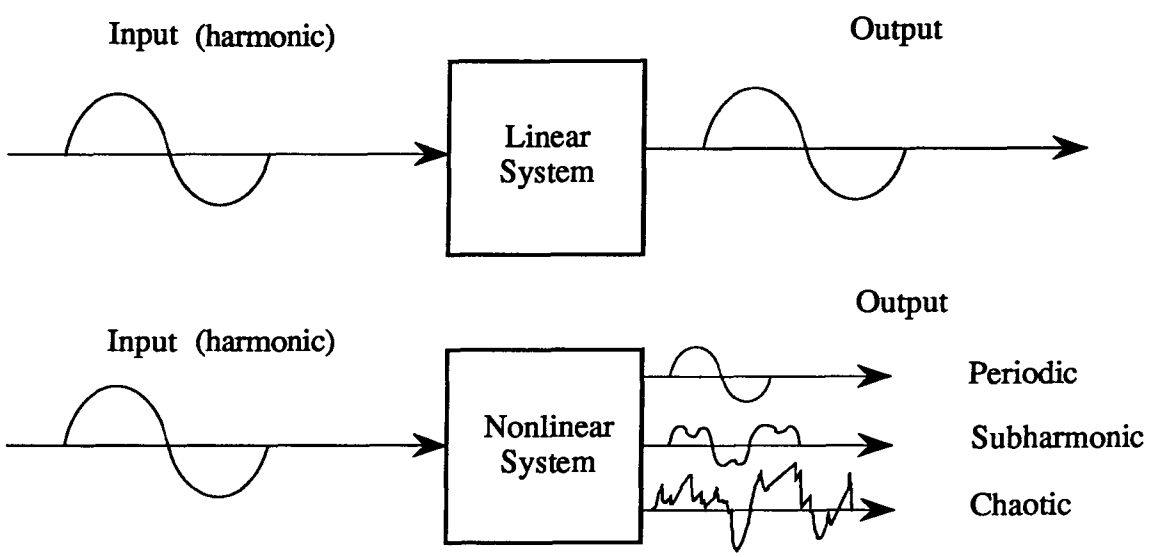

Fig. 2.4 Comparison of linear and nonlinear systems

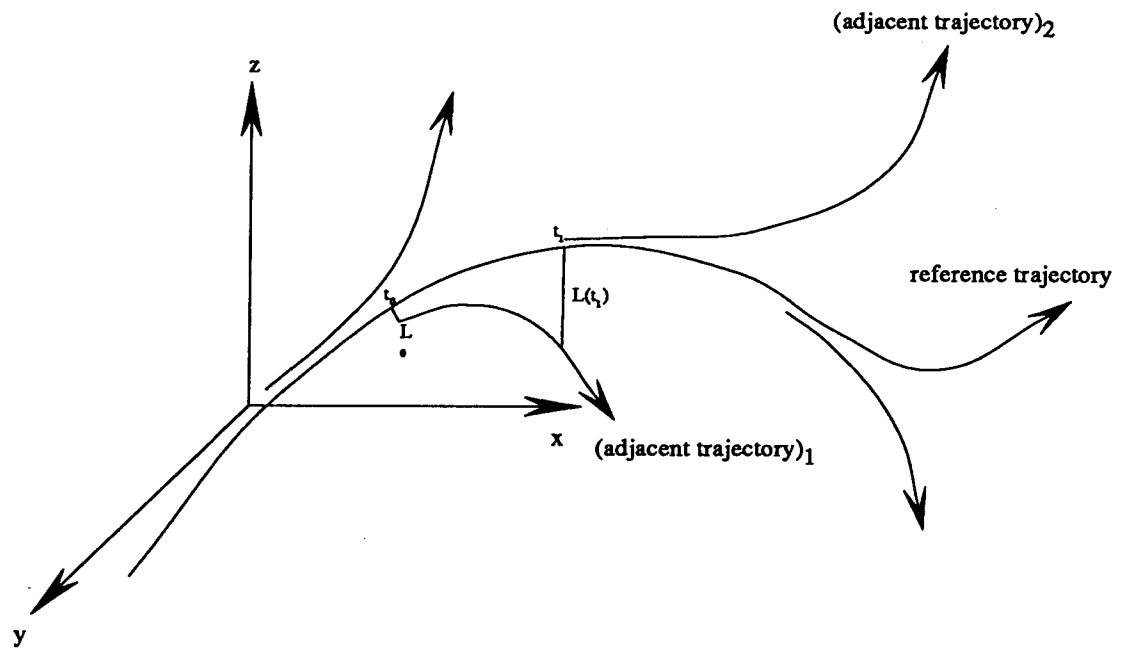

Fig. 2.5 Divergence of nearby orbits.

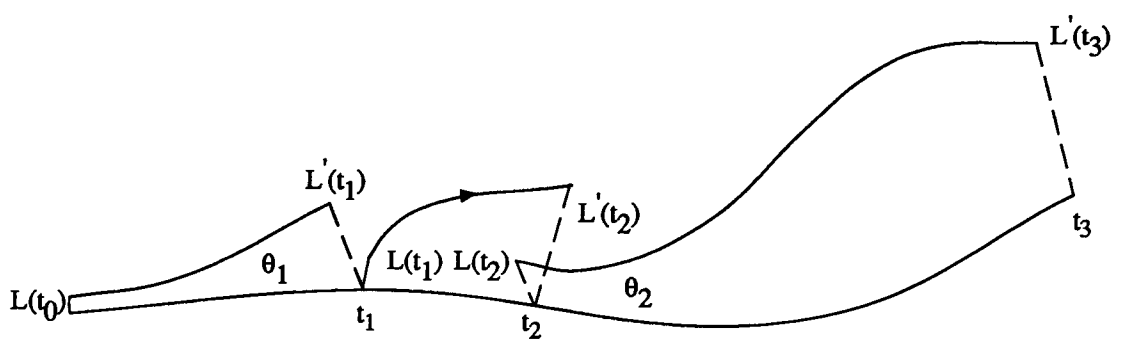

Fig 2.6 Calculation of the largest Lyapunov exponent from time series [Kapitaniak (1991)]

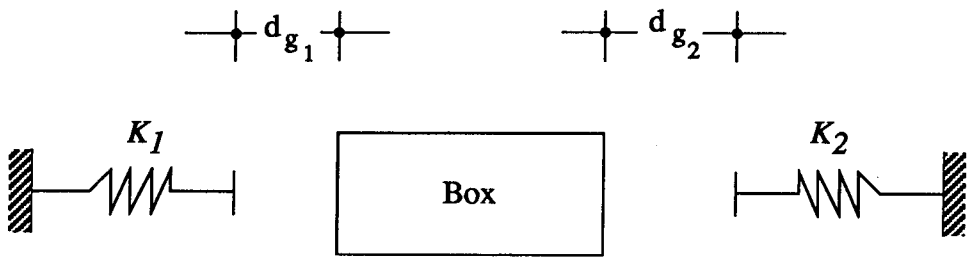

Fig. 3.1 Mathematical model of surge motions of the box

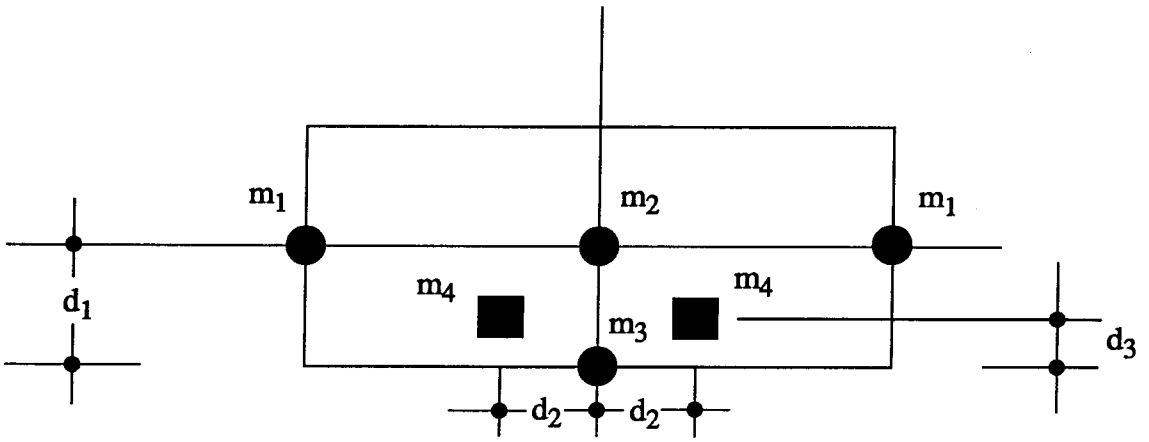

Fig. 3.2 Definition sketch for estimating the location of the centre of gravity.

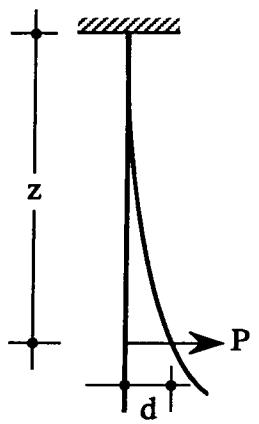

Fig. 3.3 Definition sketch for calculation of cantilever beam stiffness

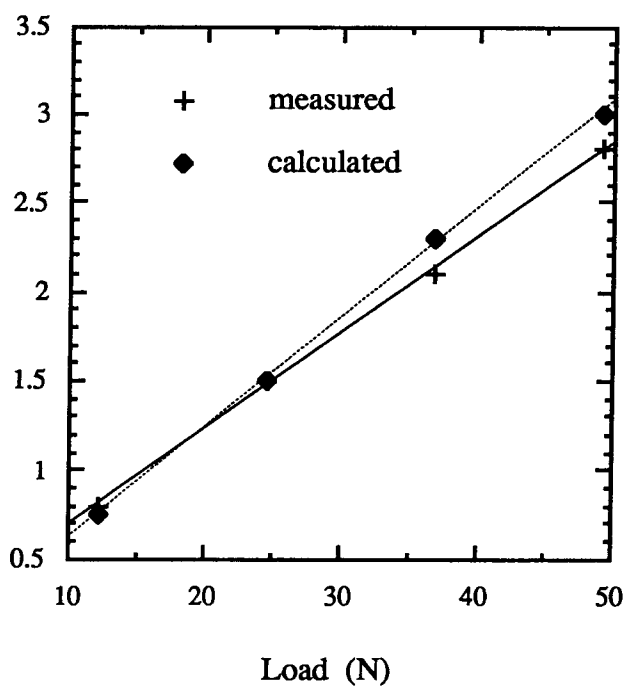

Fig. 3.4 Comparison of measured and calculated values of cantilever beam deflection

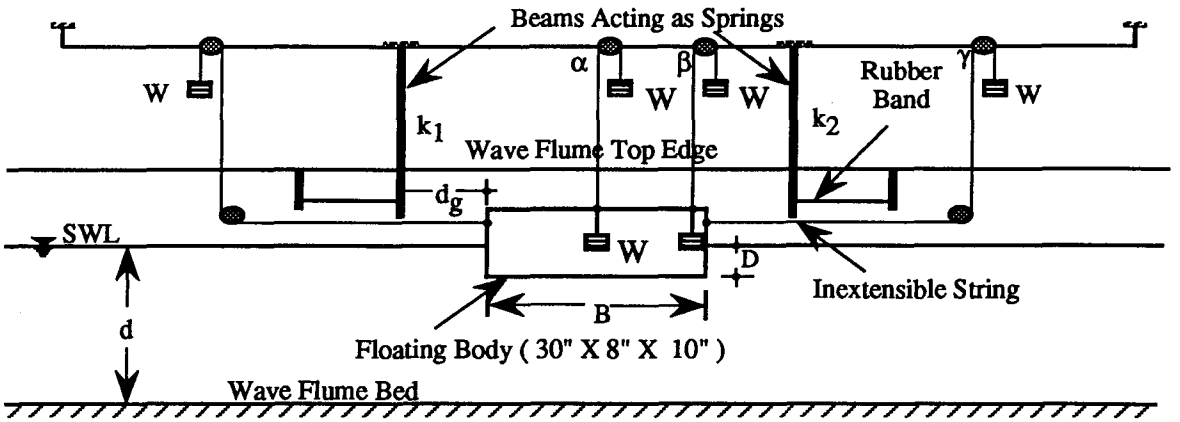

Nomenclature:

B - Beam = 76 cm
D - Draft = 10.5 cm
d - Water Depth = 55 cm
W - Small weight attached to the string
k_1, k_2 - Spring Stiffness
α, β, γ – Pulleys fitted with Potentiometers
d_g - Gap Width

Fig. 3.5 Sketch of experimental setup

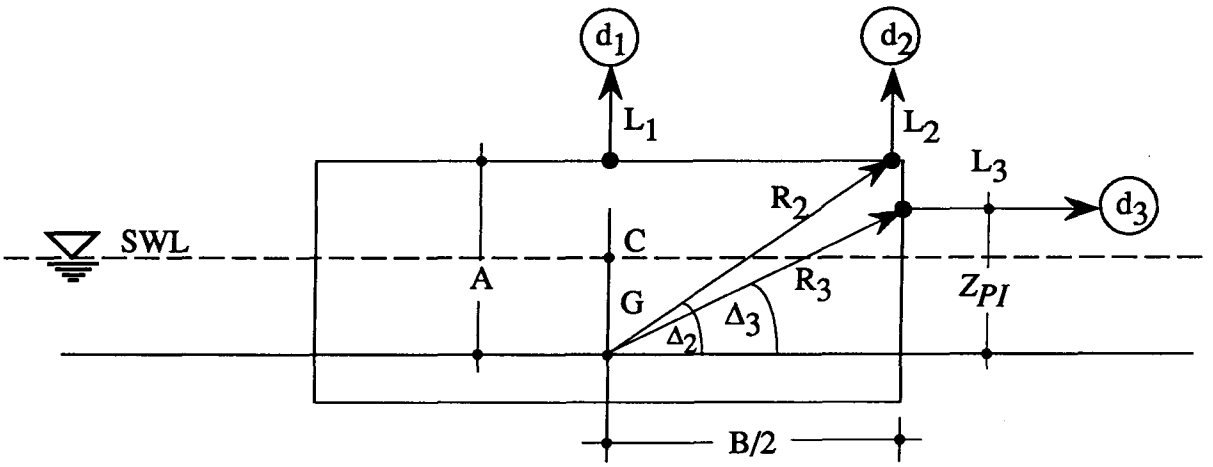

Fig. 3.6 Definition sketch - transformation equations

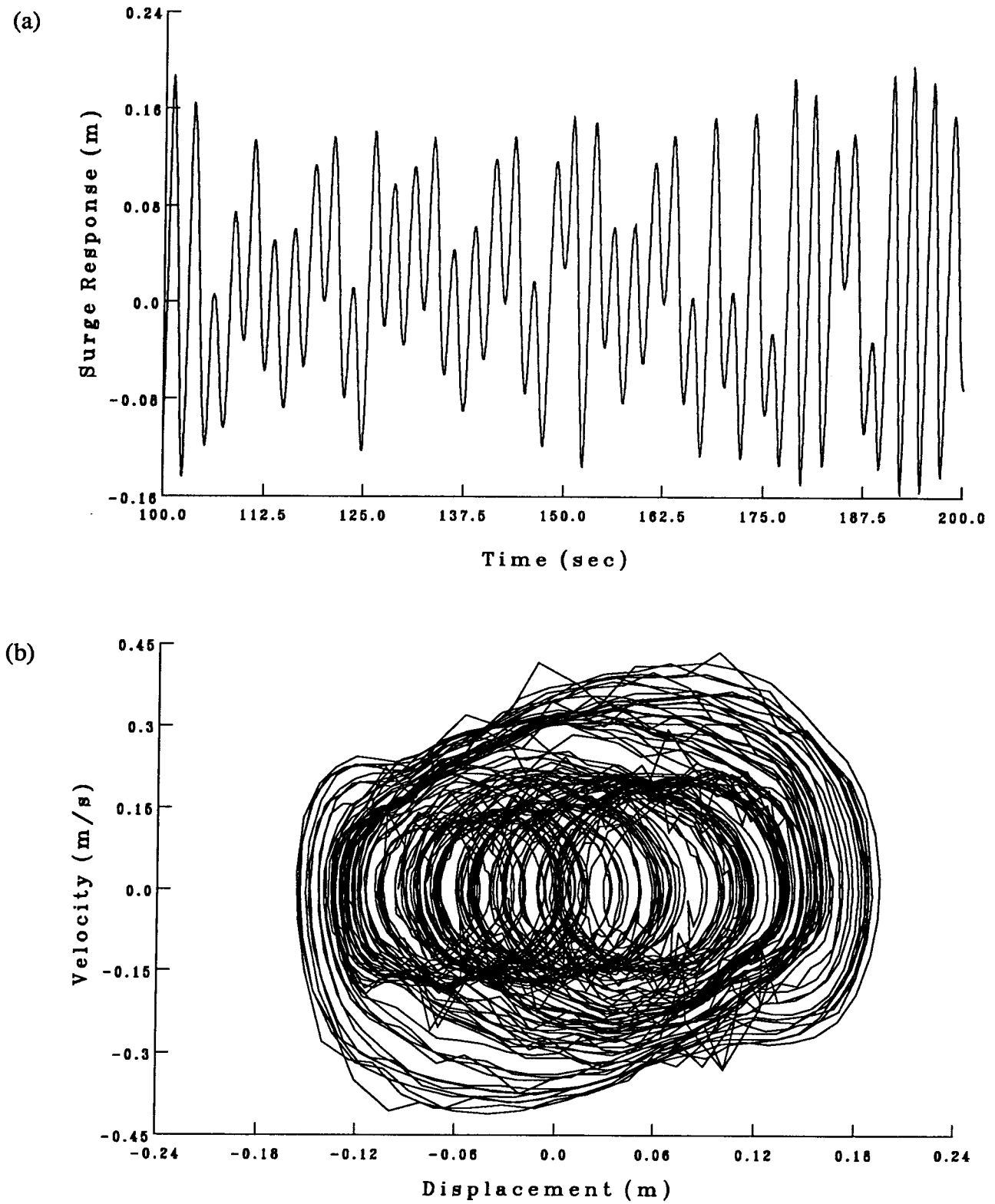

Fig 4.1 - Surge response for monochromatic excitation
(a) Time series (b) Phase portrait (c) Spectrum - logarithmic (d) Spectrum - linear
$H = 13$ cm, $T = 2.5$ s, $\alpha = 0.423$, $K = 4.25$, $d_g = 11.5$ cm

(c)

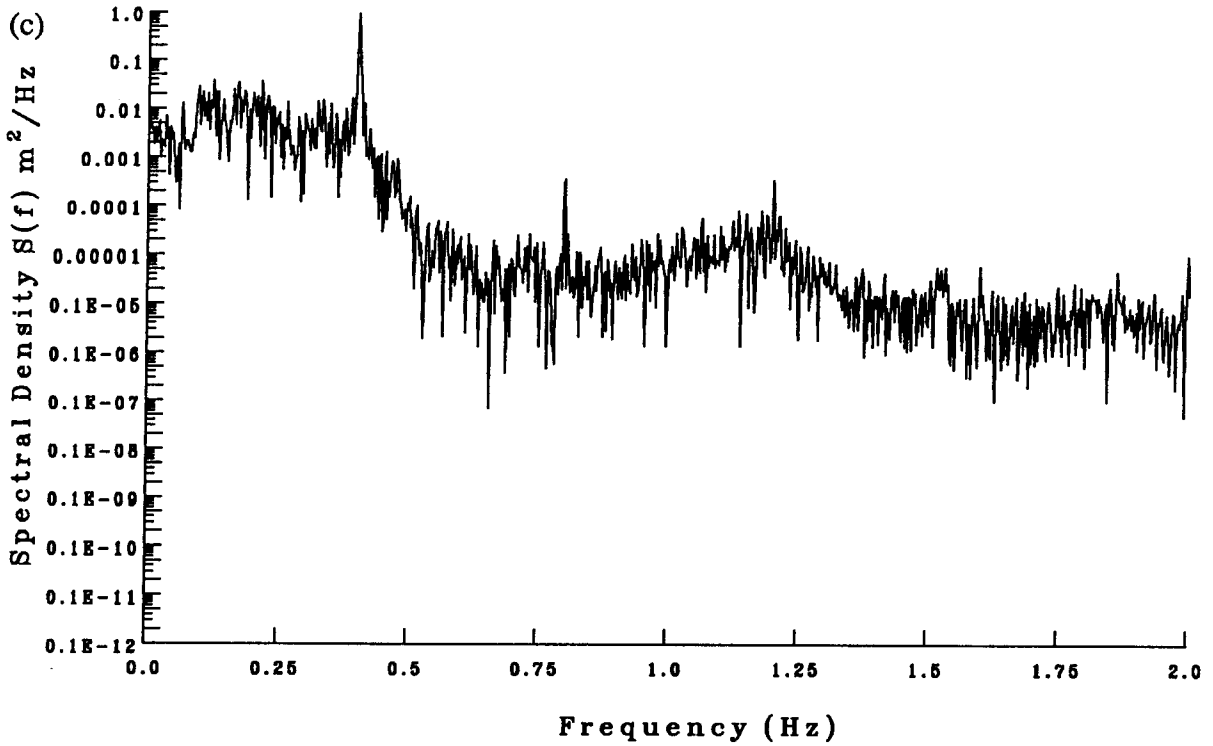
Spectral Density S(f) m²/Hz
1.0
0.1
0.01
0.001
0.0001
0.00001
0.1E-05
0.1E-06
0.1E-07
0.1E-08
0.1E-09
0.1E-10
0.1E-11
0.1E-12
0.0
0.25
0.5
0.75
1.0
1.25
1.5
1.75
2.0
Frequency (Hz)

(d)

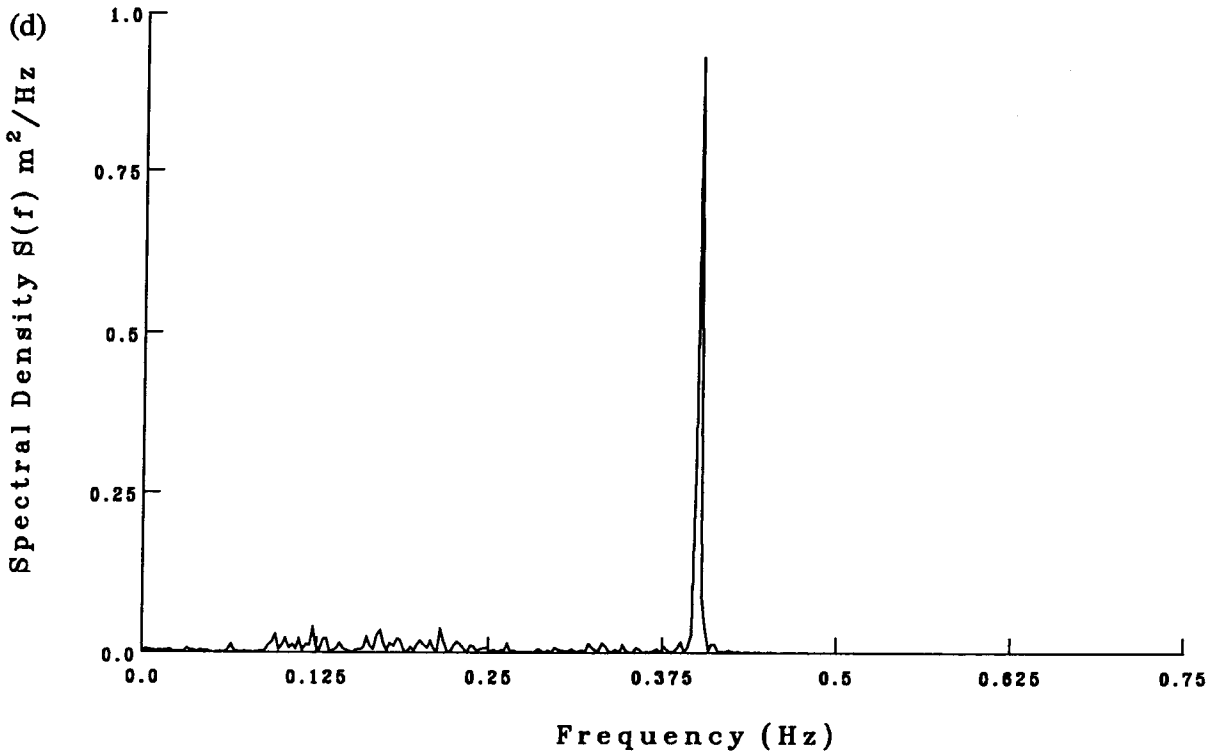
Spectral Density S(f) m²/Hz
1.0
0.75
0.5
0.25
0.0
0.0
0.125
0.25
0.375
0.5
0.625
0.75
Frequency (Hz)

(a)

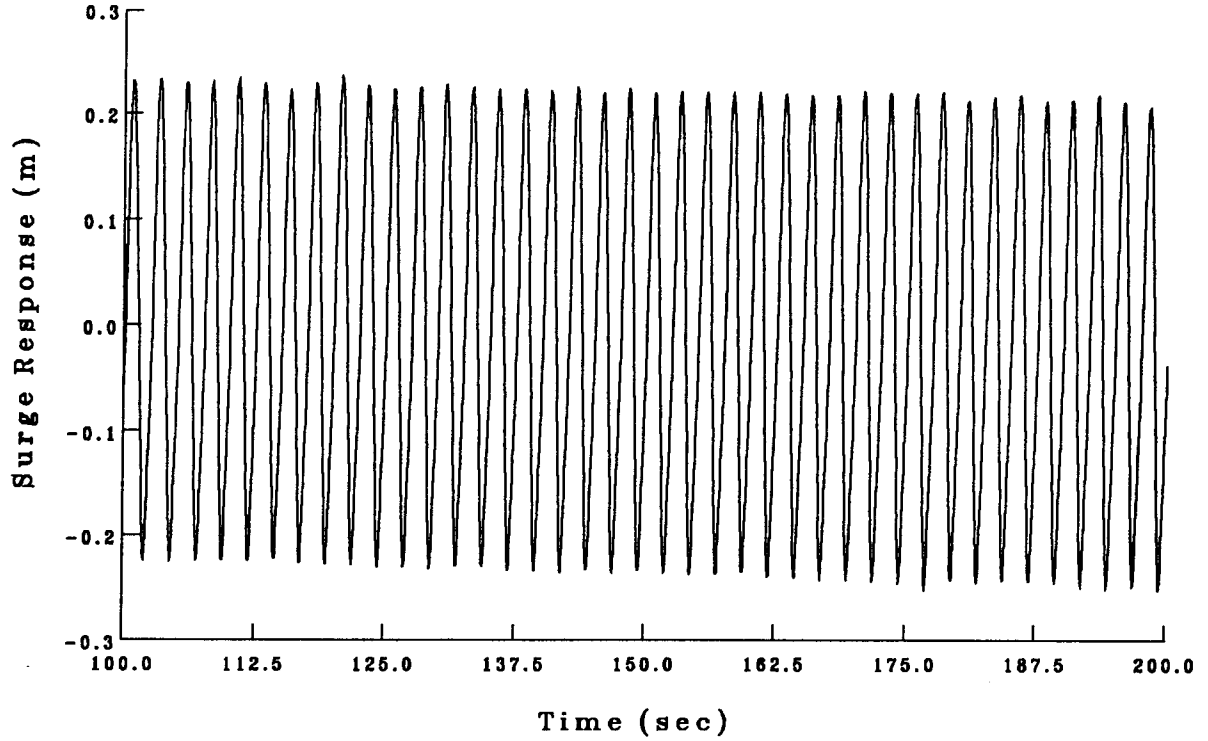

(b)

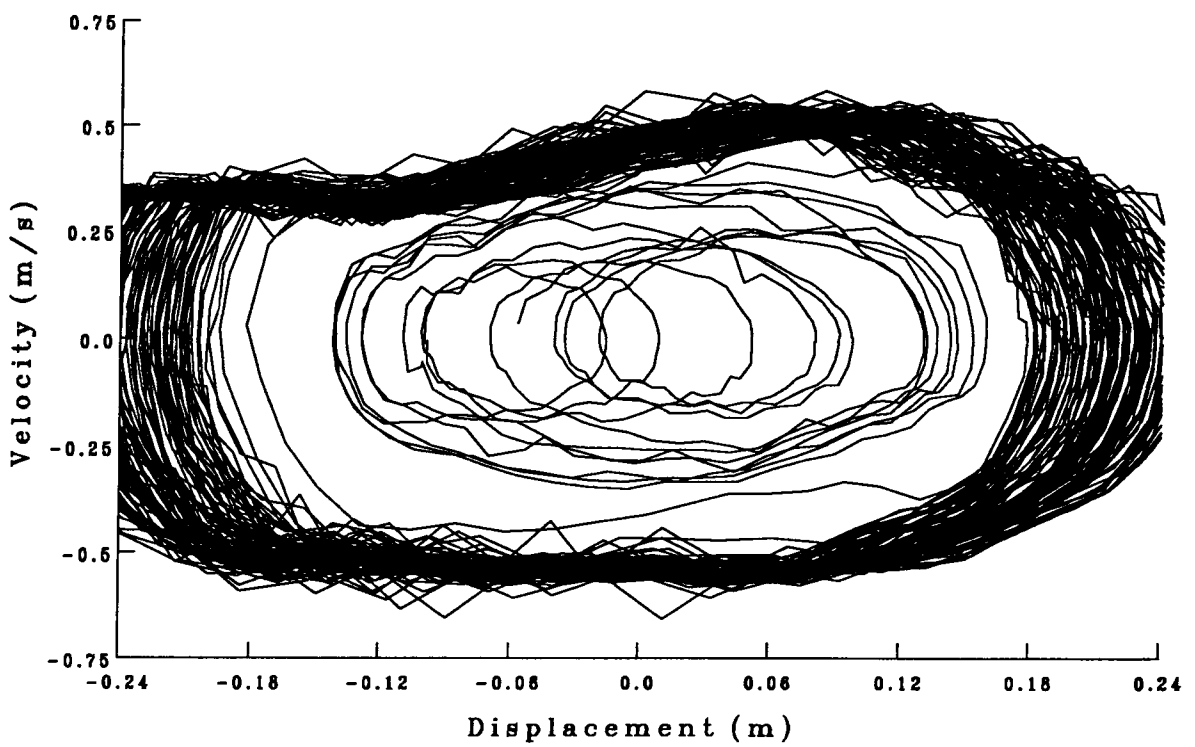

Fig 4.2 - Surge response for monochromatic excitation
(a) Time series (b) Phase portrait (c) Spectrum - logarithmic (d) Spectrum - linear
$H = 15$ cm, $T = 2.5$ s, $\alpha = 0.423$, $K = 4.25$, $d_g = 11.5$ cm

(c)

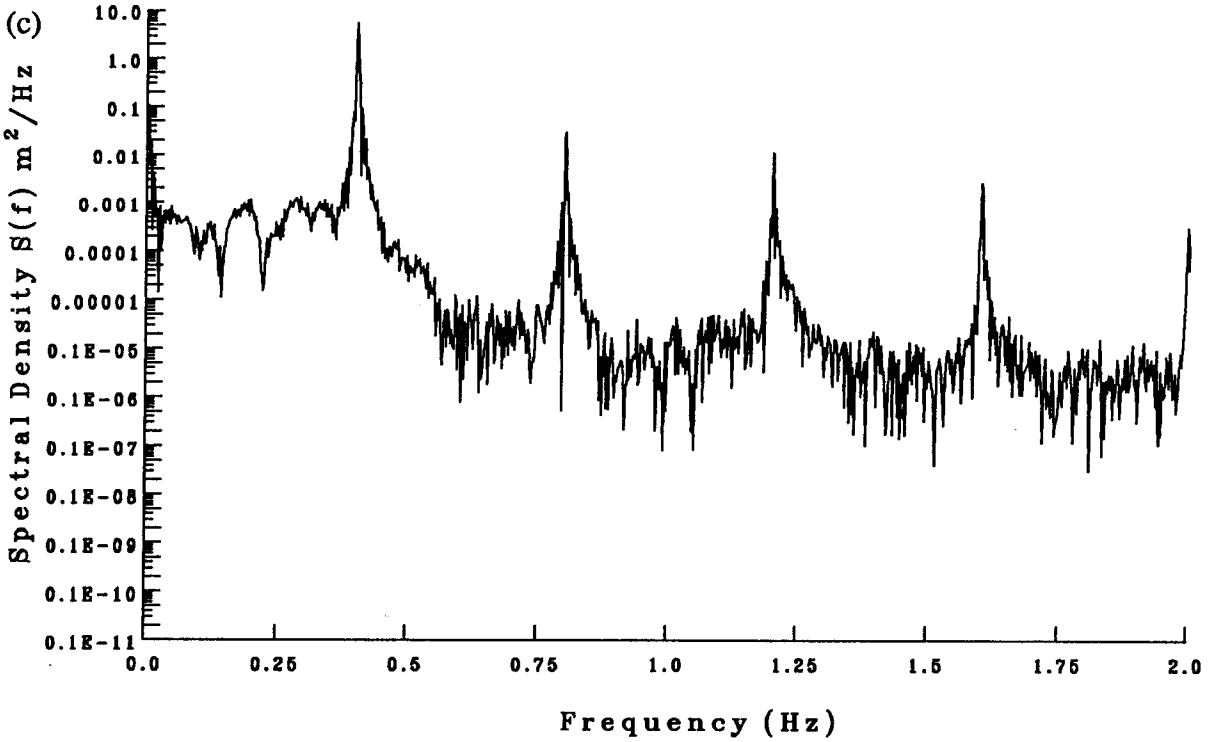
Spectral Density S(f) m²/Hz
10.0
1.0
0.1
0.01
0.001
0.0001
0.00001
0.1E-05
0.1E-06
0.1E-07
0.1E-08
0.1E-09
0.1E-10
0.1E-11
0.0
0.25
0.5
0.75
1.0
1.25
1.5
1.75
2.0
Frequency (Hz)

(d)

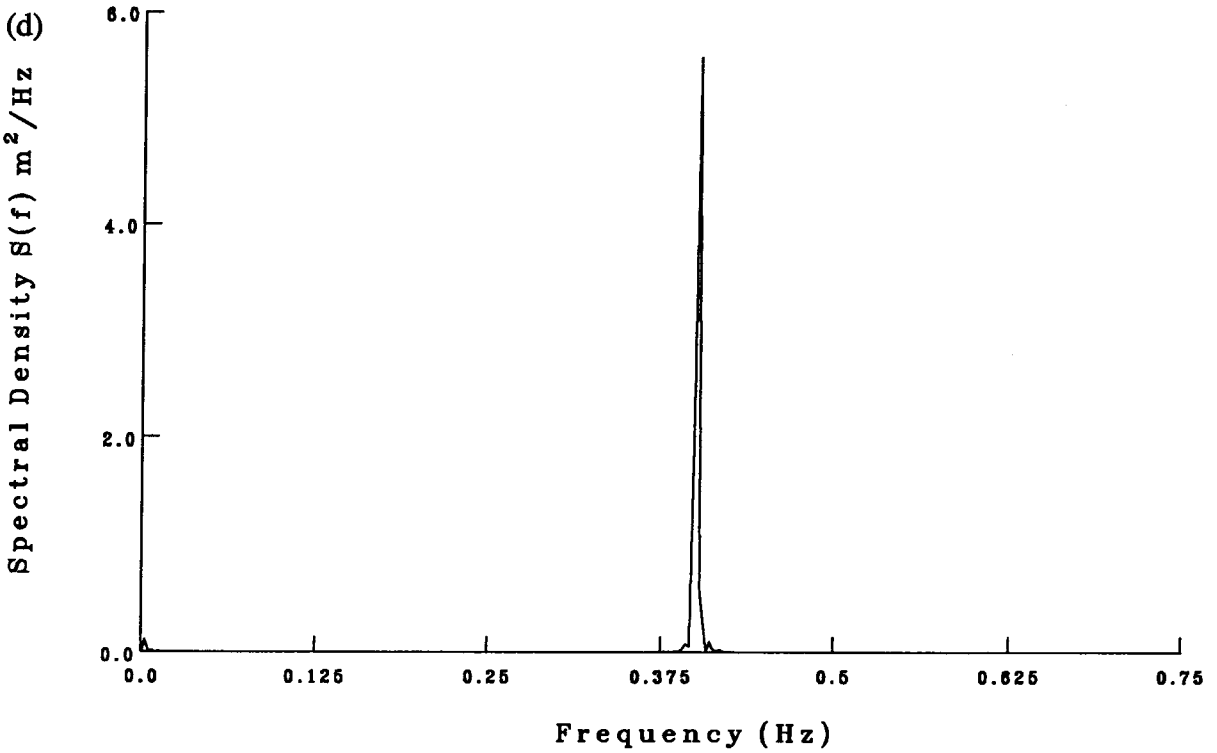
Spectral Density S(f) m²/Hz
6.0
4.0
2.0
0.0
0.0
0.125
0.25
0.375
0.5
0.625
0.75
Frequency (Hz)

(a)

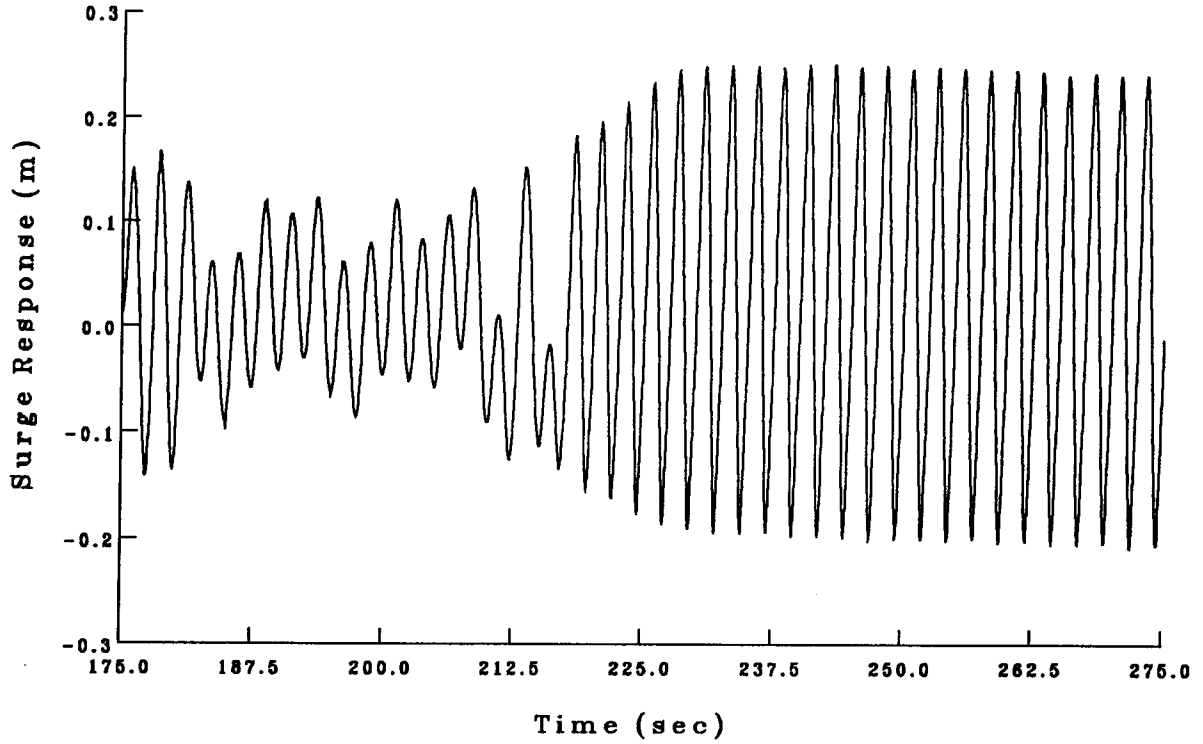

(b)

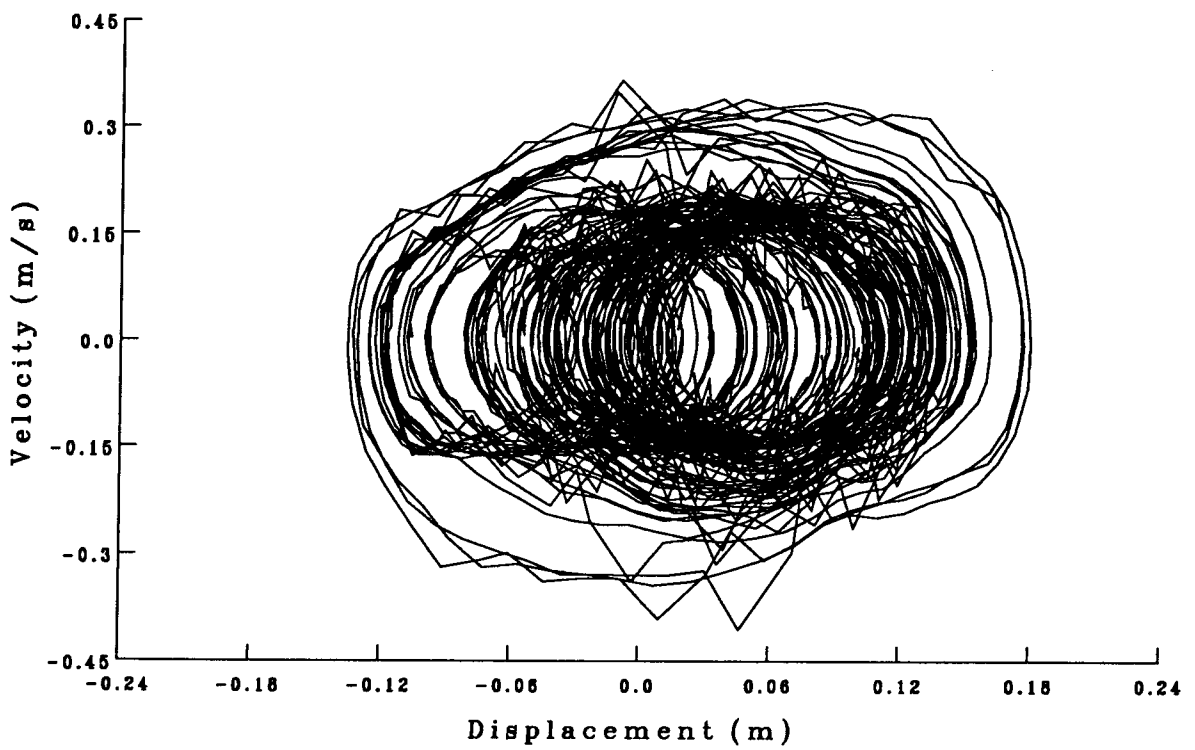

Fig 4.3 - Surge response for monochromatic excitation
(a) Time series (b) Phase portrait (c) Spectrum - logarithmic (d) Spectrum - linear
$H = 14$ cm, $T = 2.5$ s, $\alpha = 0.423$, $K = 4.25$, $d_g = 11.5$ cm

(c)

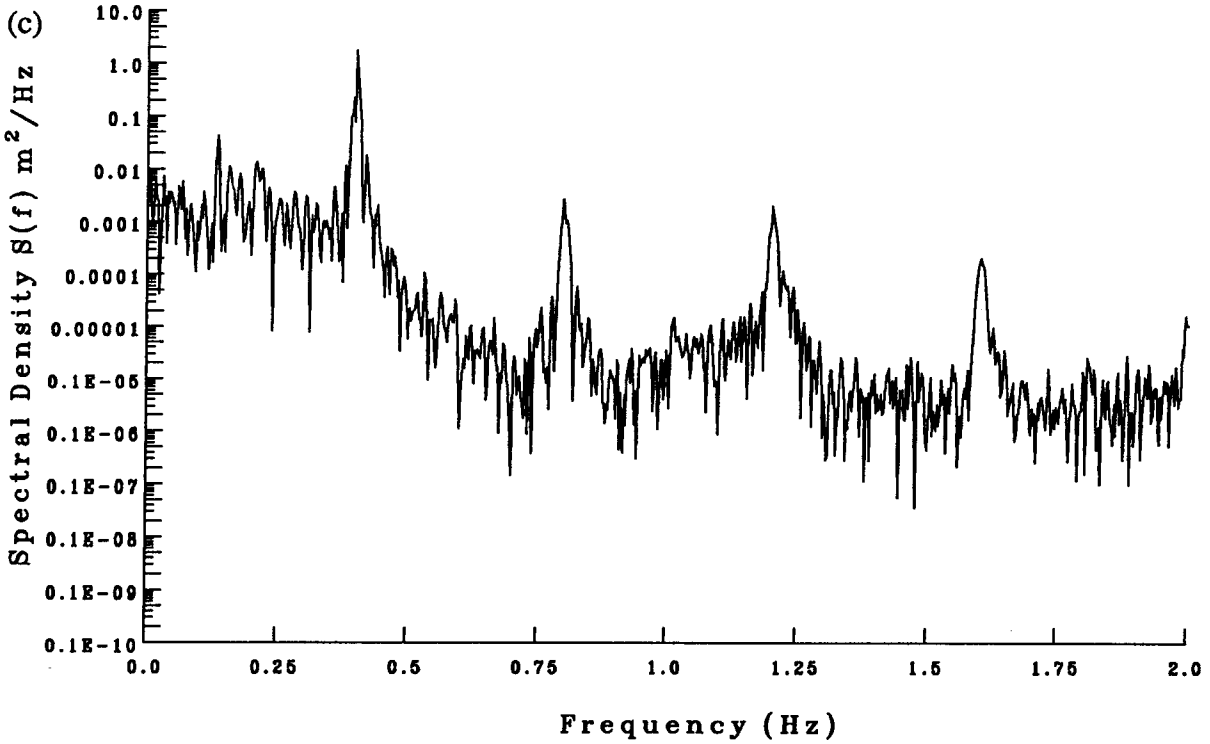
Spectral Density S(f) m²/Hz
10.0
1.0
0.1
0.01
0.001
0.0001
0.00001
0.1E-05
0.1E-06
0.1E-07
0.1E-08
0.1E-09
0.1E-10
0.0
0.25
0.5
0.75
1.0
1.25
1.5
1.75
2.0
Frequency (Hz)

(d)

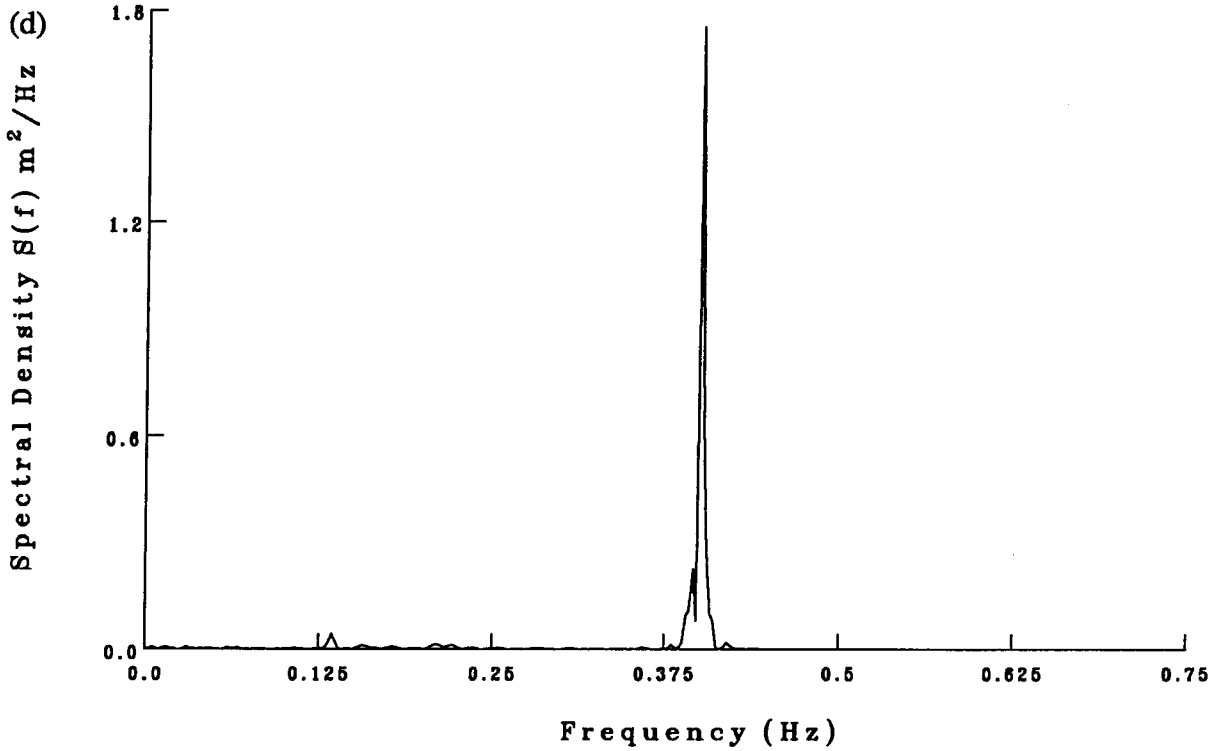
Spectral Density S(f) m²/Hz
1.8
1.2
0.6
0.0
0.0
0.125
0.25
0.375
0.5
0.625
0.75
Frequency (Hz)

(a)

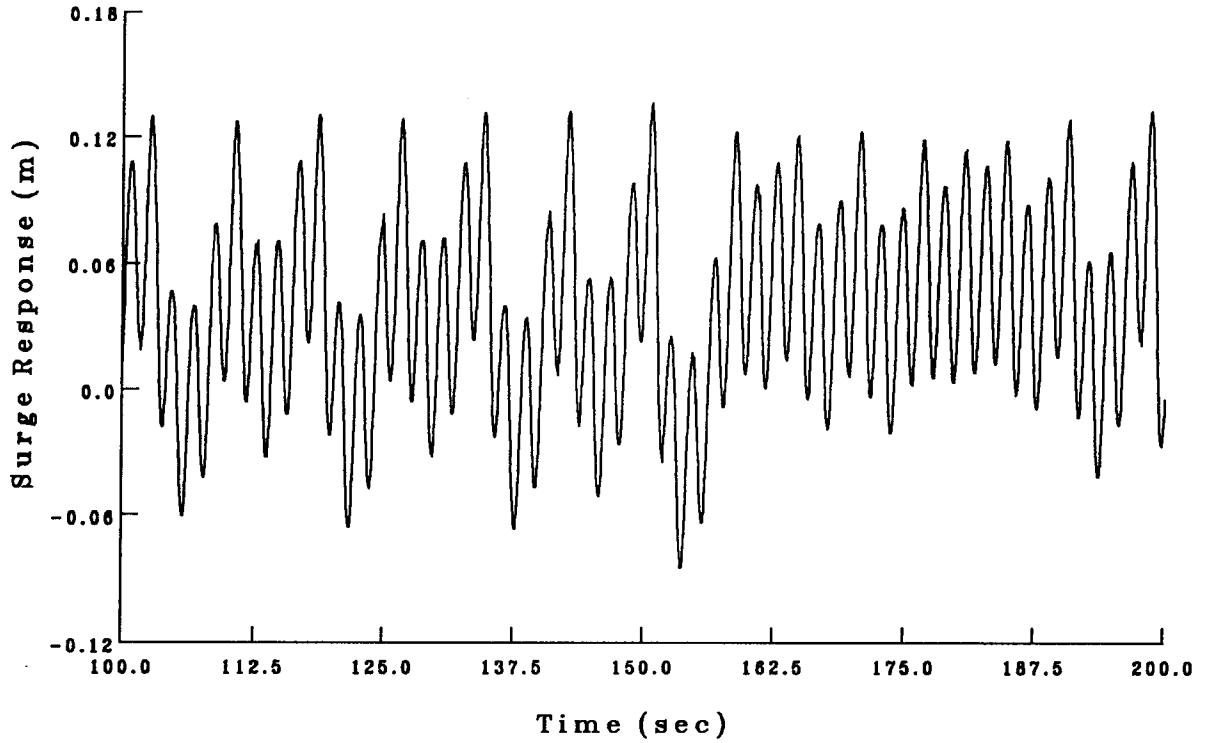

(b)

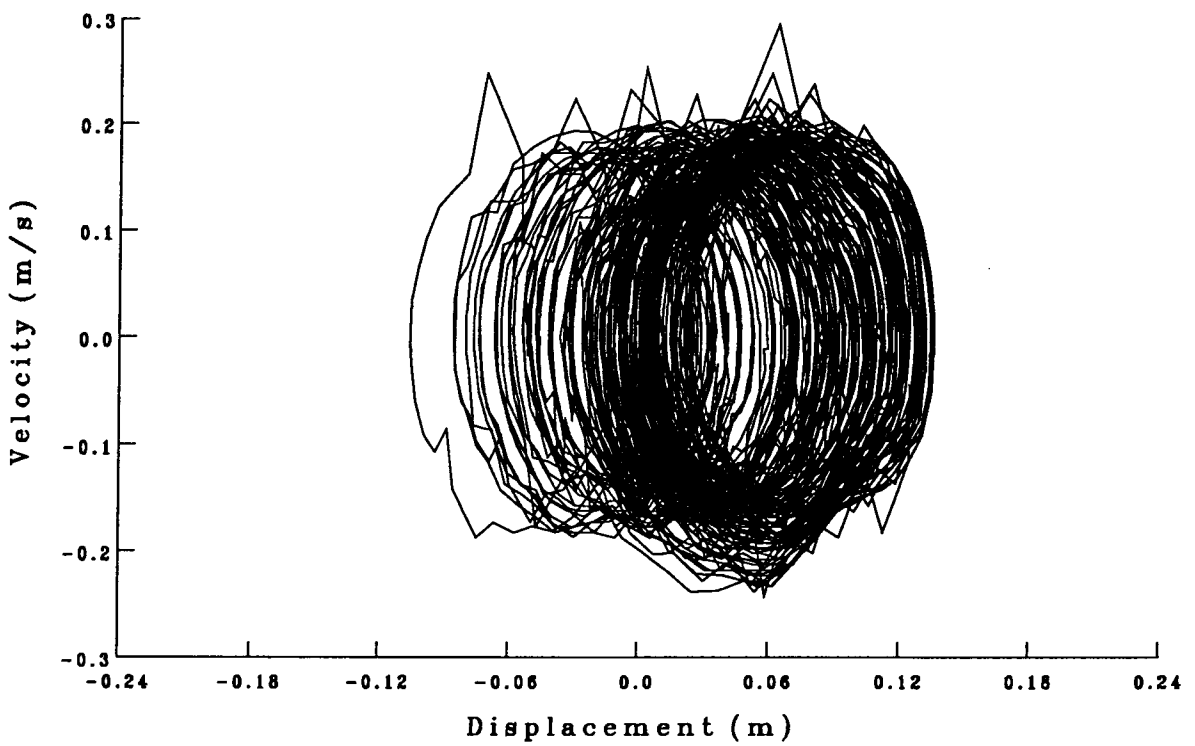

Fig 4.4 - Surge response for monochromatic excitation
(a) Time series (b) Phase portrait (c) Spectrum - lograrithmic (d) Spectrum - linear
$H = 13$ cm, $T = 2.0$ s, $\alpha = 0.529$, $K = 4.25$, $d_g = 11.5$ cm

(c)

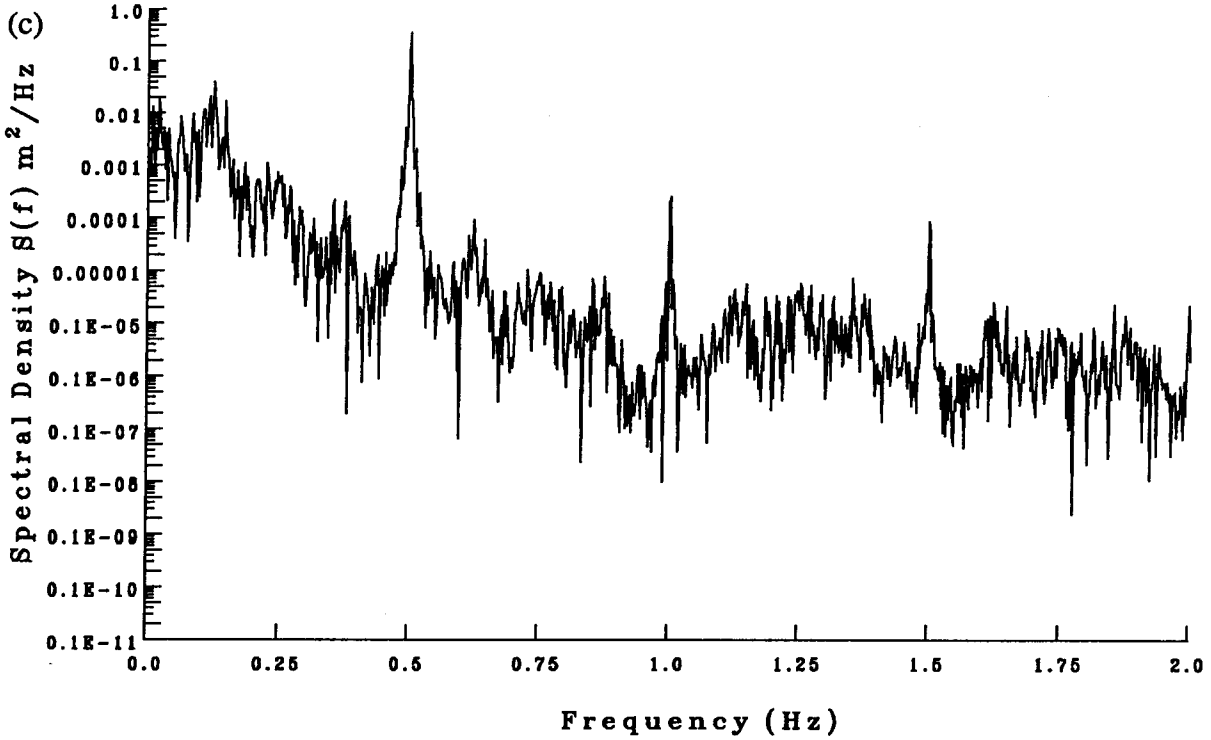
Spectral Density S(f) m²/Hz
1.0
0.1
0.01
0.001
0.0001
0.00001
0.1E-05
0.1E-06
0.1E-07
0.1E-08
0.1E-09
0.1E-10
0.1E-11
0.0
0.25
0.5
0.75
1.0
1.25
1.5
1.75
2.0
Frequency (Hz)

(d)

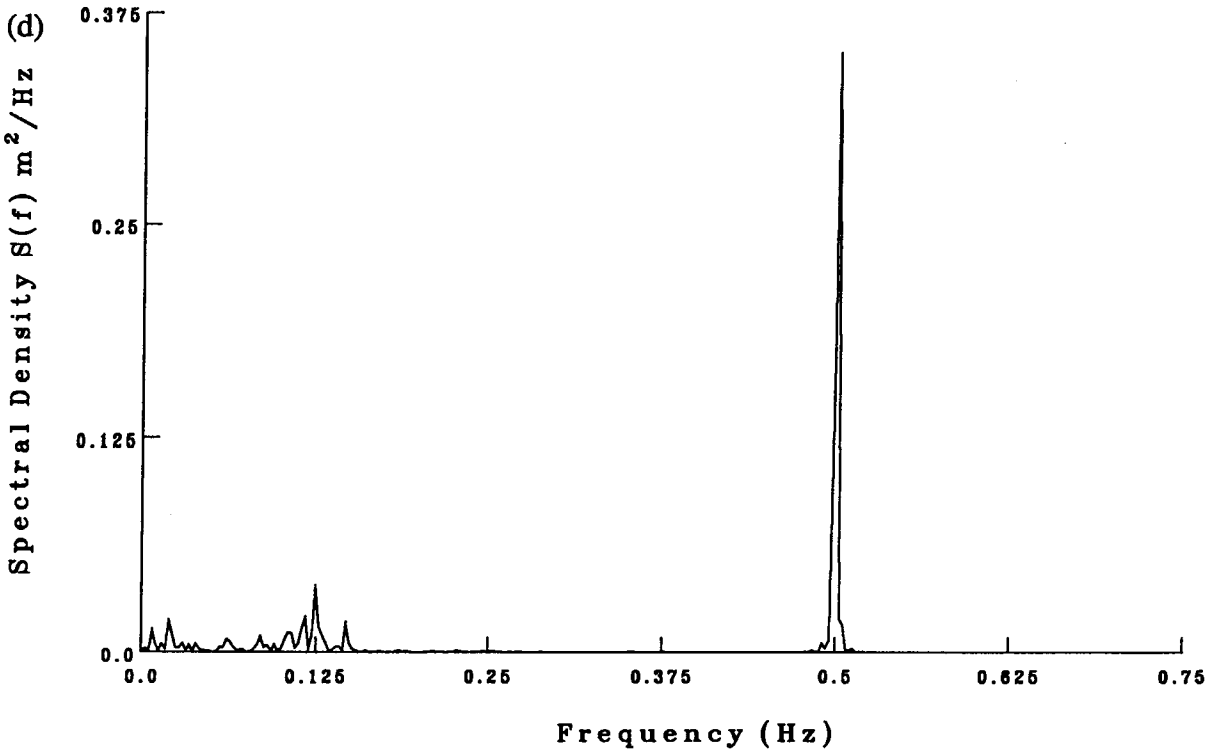
Spectral Density S(f) m²/Hz
0.375
0.25
0.125
0.0
0.0
0.125
0.25
0.375
0.5
0.625
0.75
Frequency (Hz)

(a)

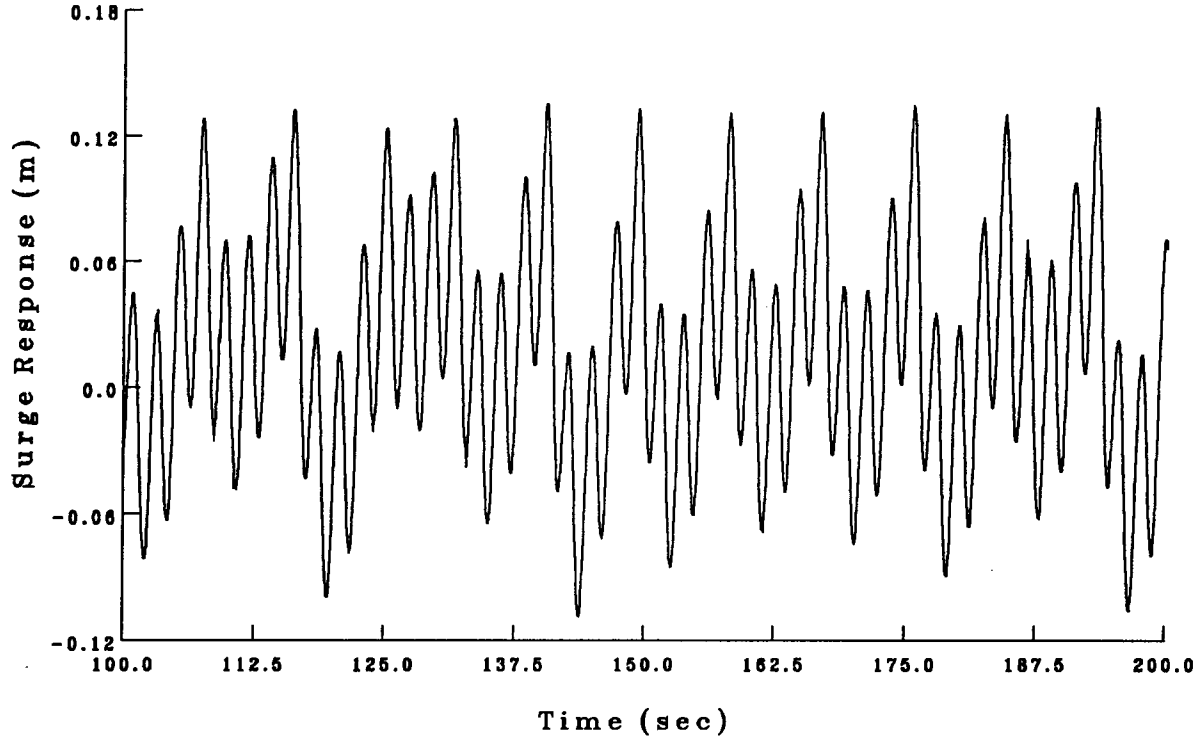

(b)

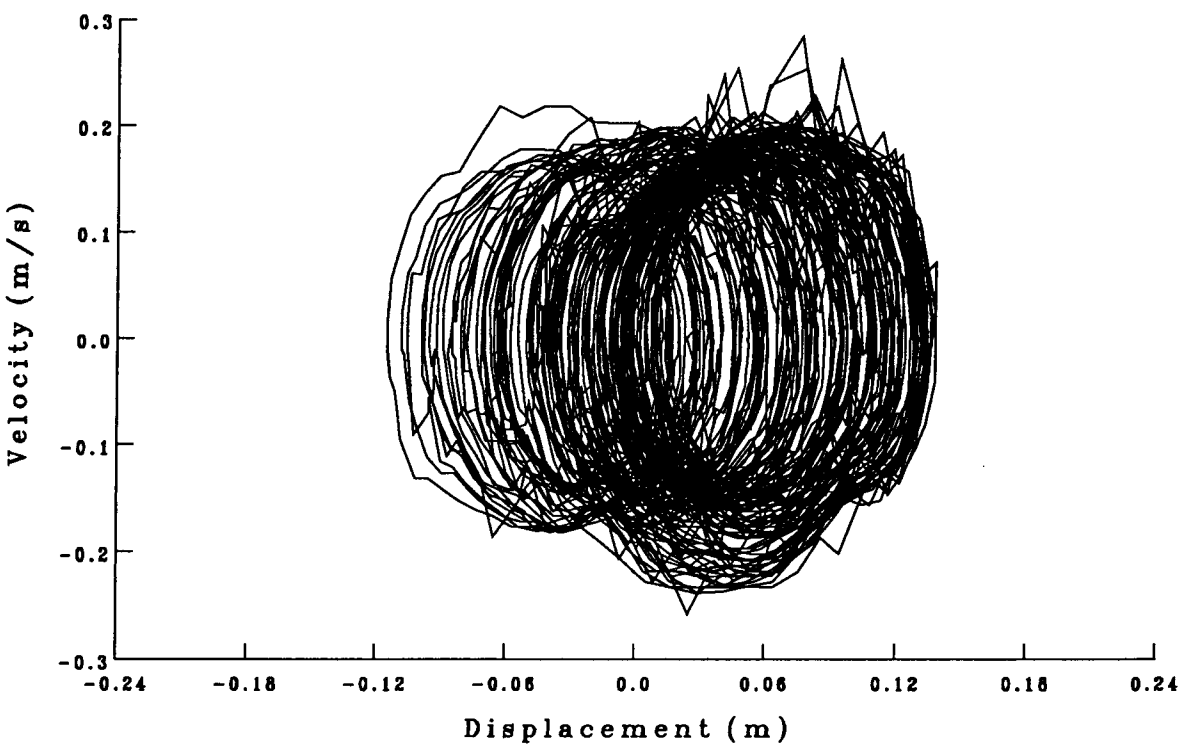

Fig 4.5 - Surge response for monochromatic excitation
(a) Time series (b) Phase portrait (c) Spectrum - lograrithmic (d) Spectrum - linear
$H = 13$ cm, $T = 2.2$ s, $\alpha = 0.481$, $K = 4.25$, $d_g = 11.5$ cm

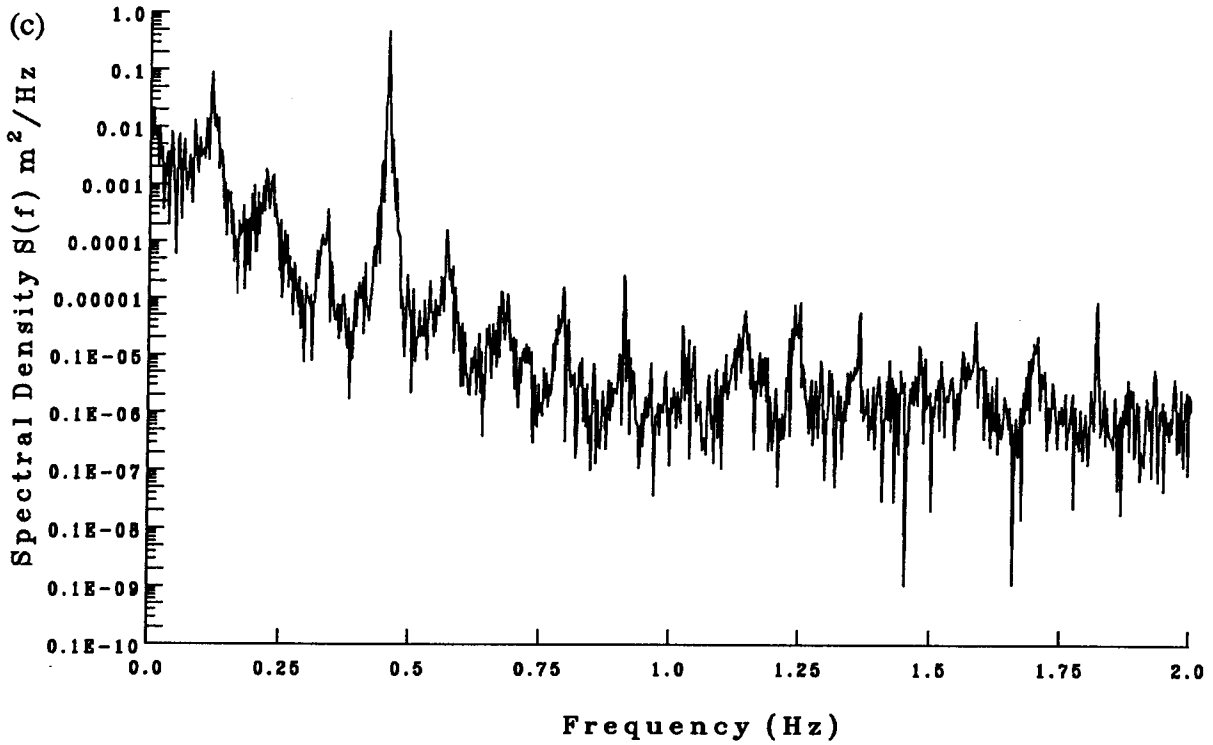
(c)
Spectral Density S(f) m²/Hz
1.0
0.1
0.01
0.001
0.0001
0.00001
0.1E-05
0.1E-06
0.1E-07
0.1E-08
0.1E-09
0.1E-10
0.0
0.25
0.5
0.75
1.0
1.25
1.5
1.75
2.0
Frequency (Hz)

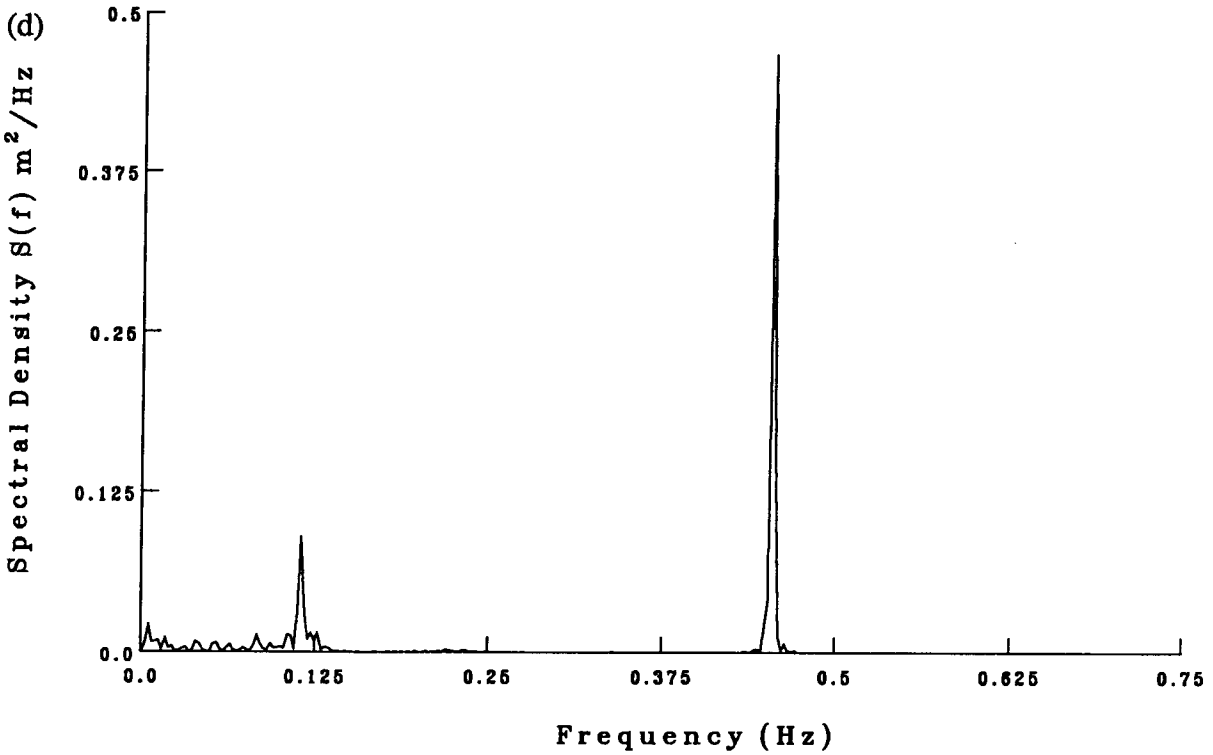
(d)
Spectral Density S(f) m²/Hz
0.5
0.375
0.25
0.125
0.0
0.0
0.125
0.25
0.375
0.5
0.625
0.75
Frequency (Hz)

(a)

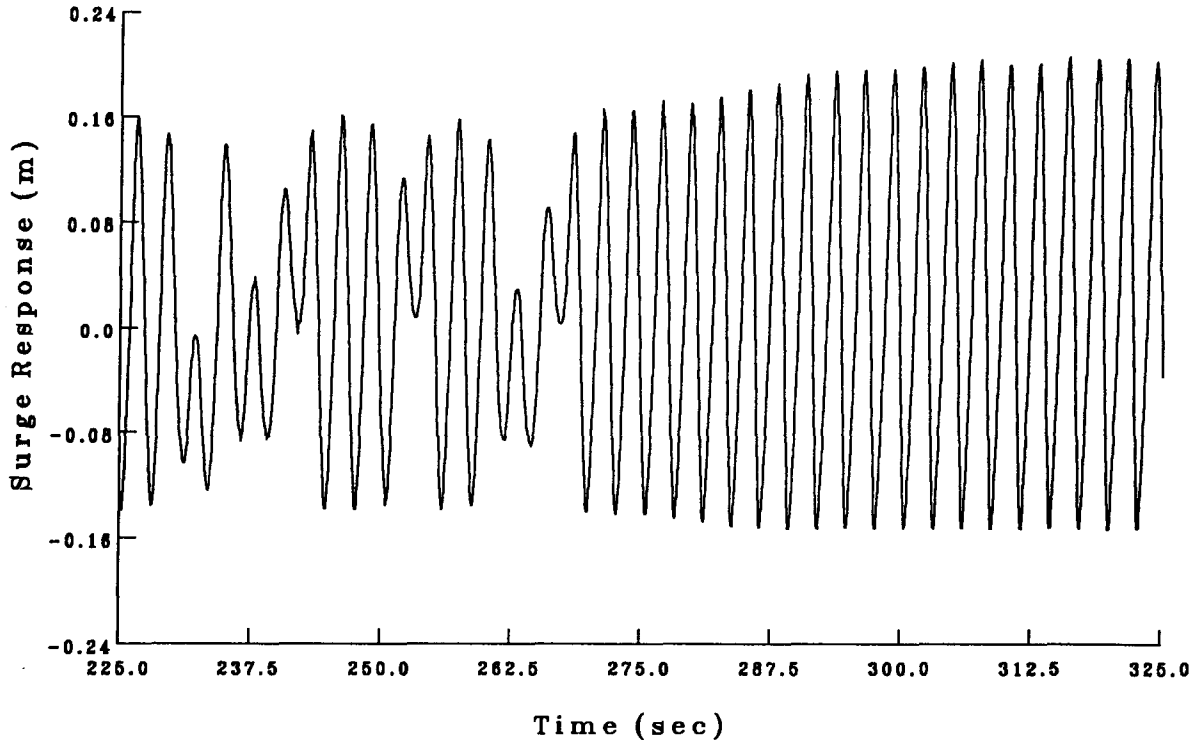

(b)

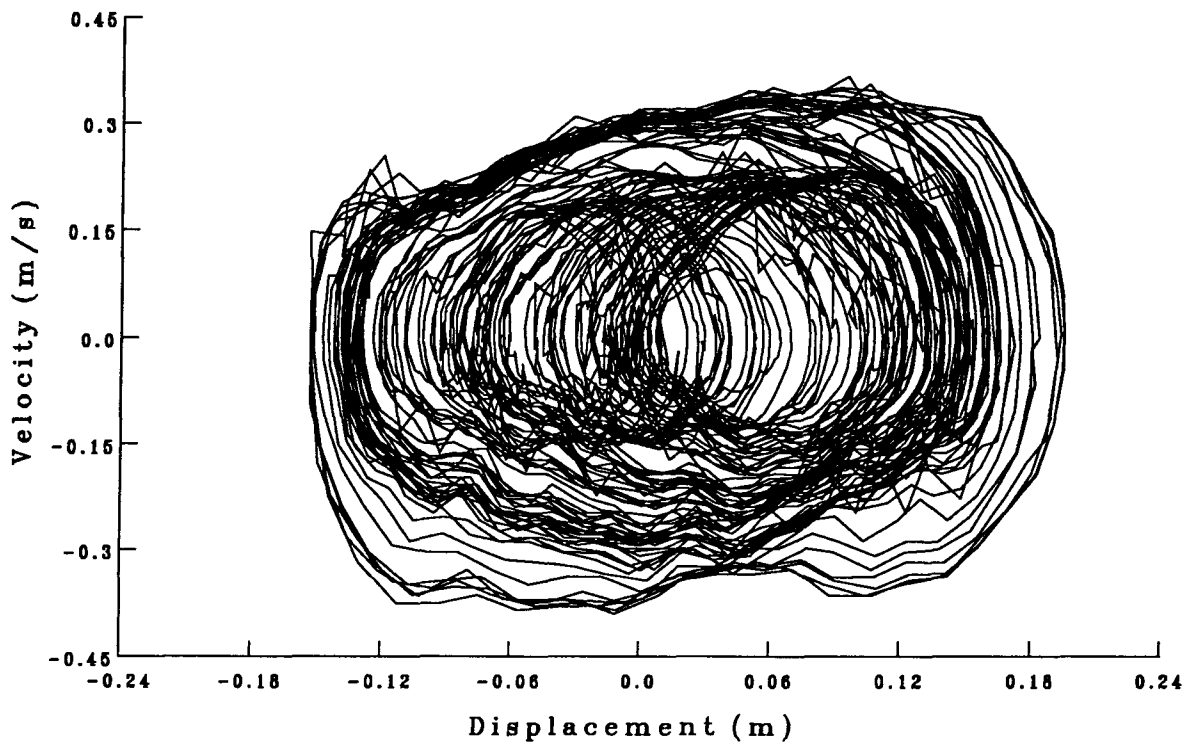

Fig 4.6 - Surge response for monochromatic excitation
(a) Time series (b) Phase portrait (c) Spectrum - lograrithmic (d) Spectrum - linear
$H = 13$ cm, $T = 2.8$ s, $\alpha = 0.378$, $K = 4.25$, $d_g = 11.5$ cm

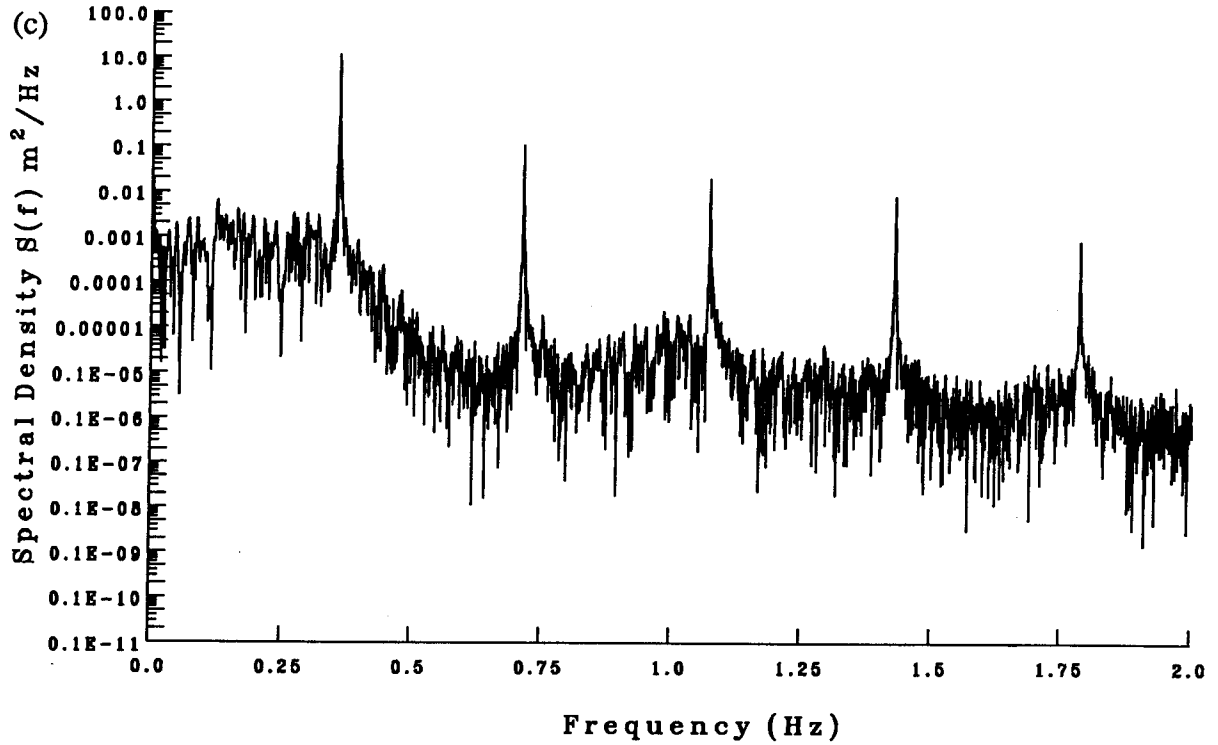
(c)
Spectral Density S(f) m²/Hz
100.0
10.0
1.0
0.1
0.01
0.001
0.0001
0.00001
0.1E-05
0.1E-06
0.1E-07
0.1E-08
0.1E-09
0.1E-10
0.1E-11
0.0
0.25
0.5
0.75
1.0
1.25
1.5
1.75
2.0
Frequency (Hz)

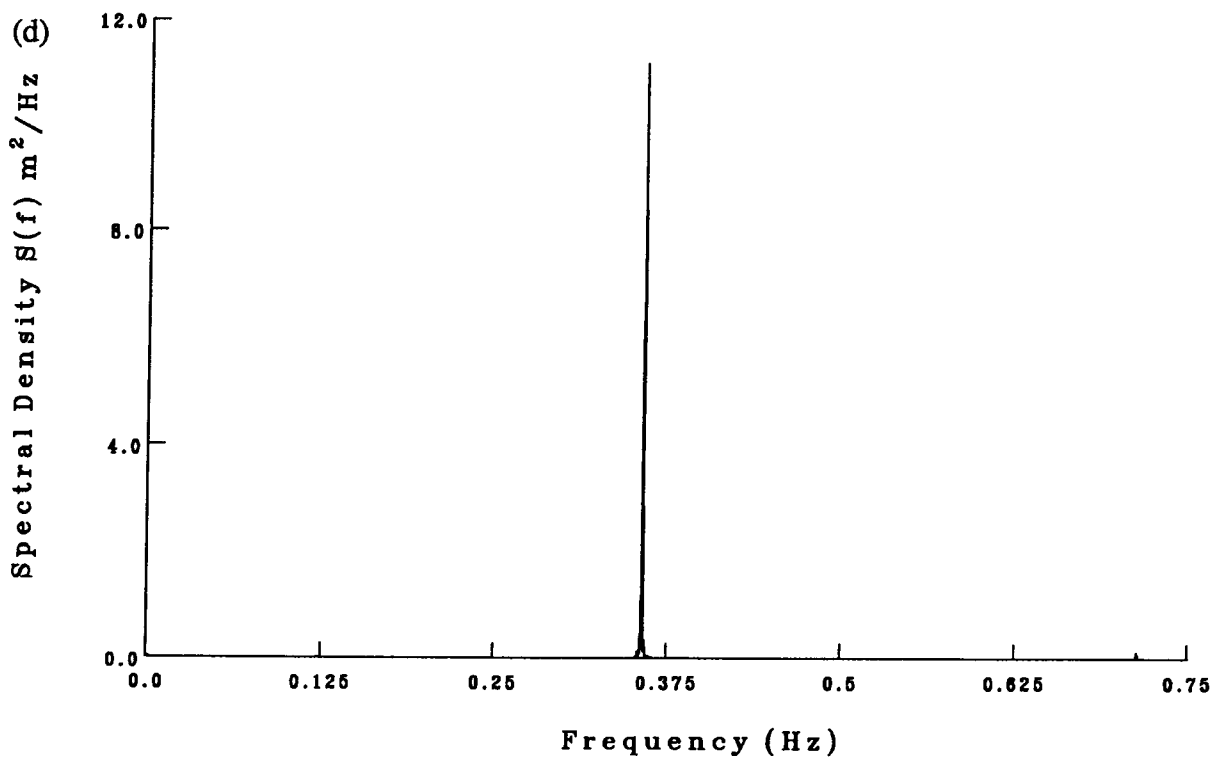
(d)
Spectral Density S(f) m²/Hz
12.0
8.0
4.0
0.0
0.0
0.125
0.25
0.375
0.5
0.625
0.75
Frequency (Hz)

(a)

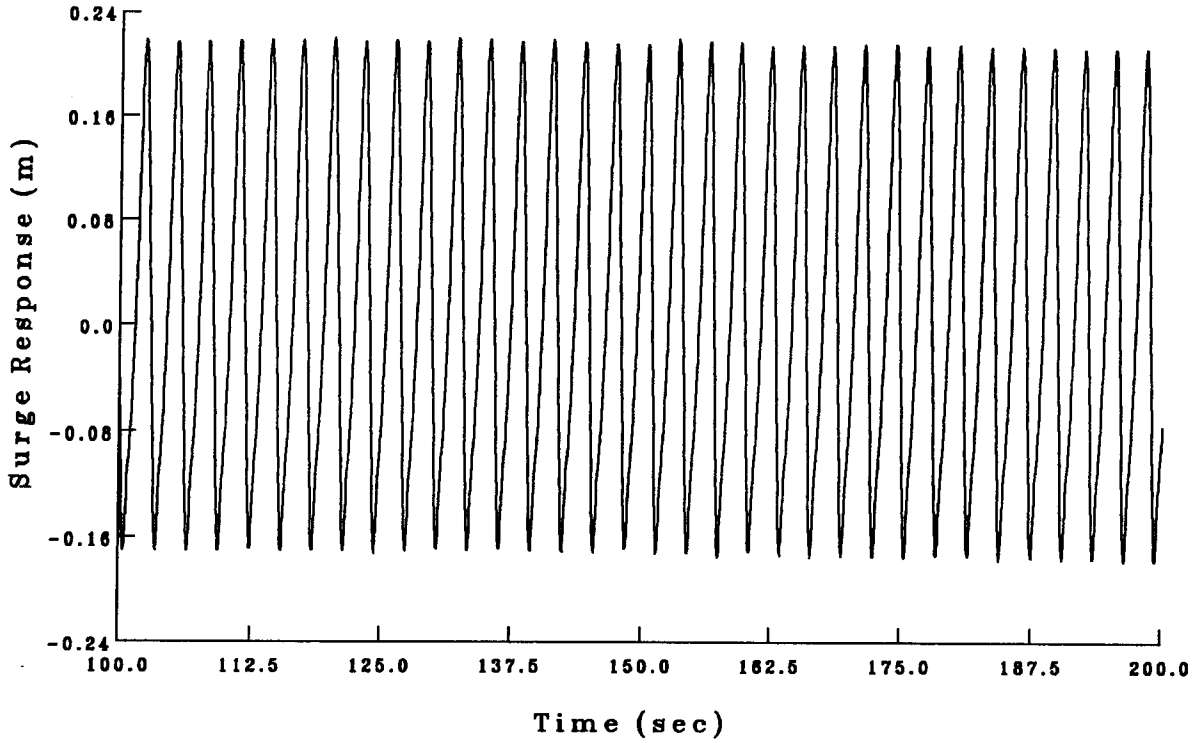

(b)

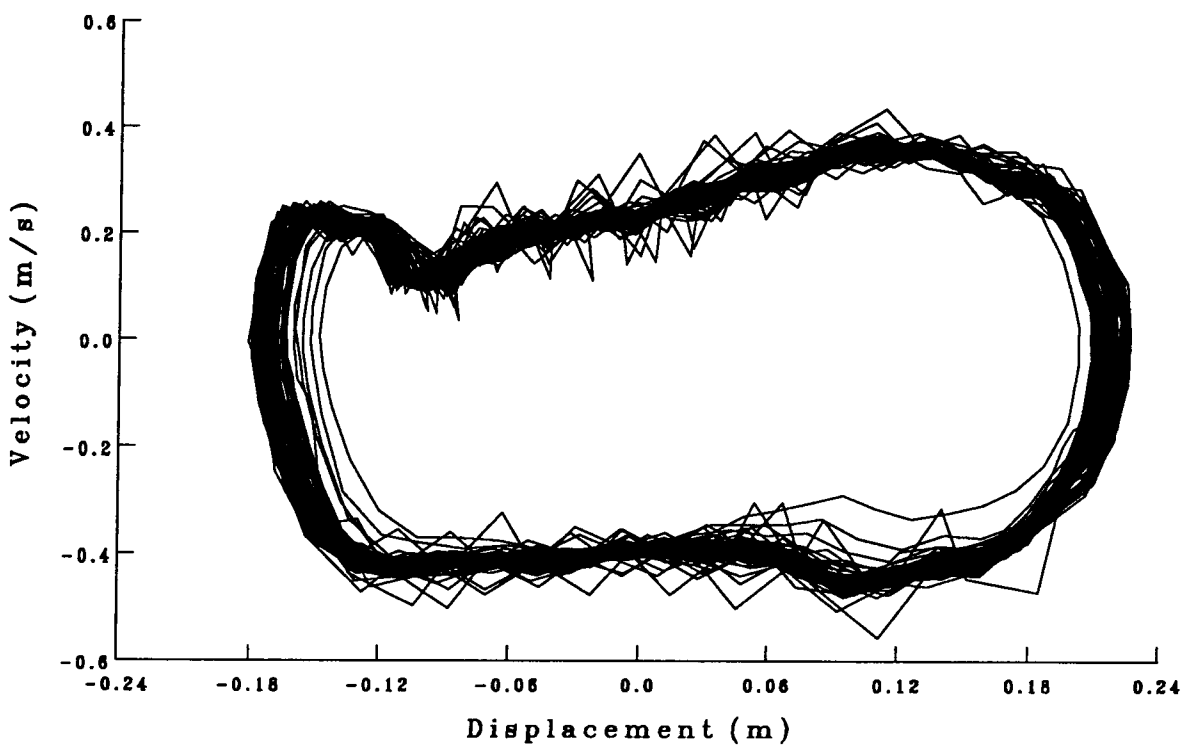

Fig 4.7 - Surge response for monochromatic excitation
(a) Time series (b) Phase portrait (c) Spectrum - lograrithmic (d) Spectrum - linear
$H = 13$ cm, $T = 3.0$ s, $\alpha = 0.353$, $K = 4.25$, $d_g = 11.5$ cm

(c)

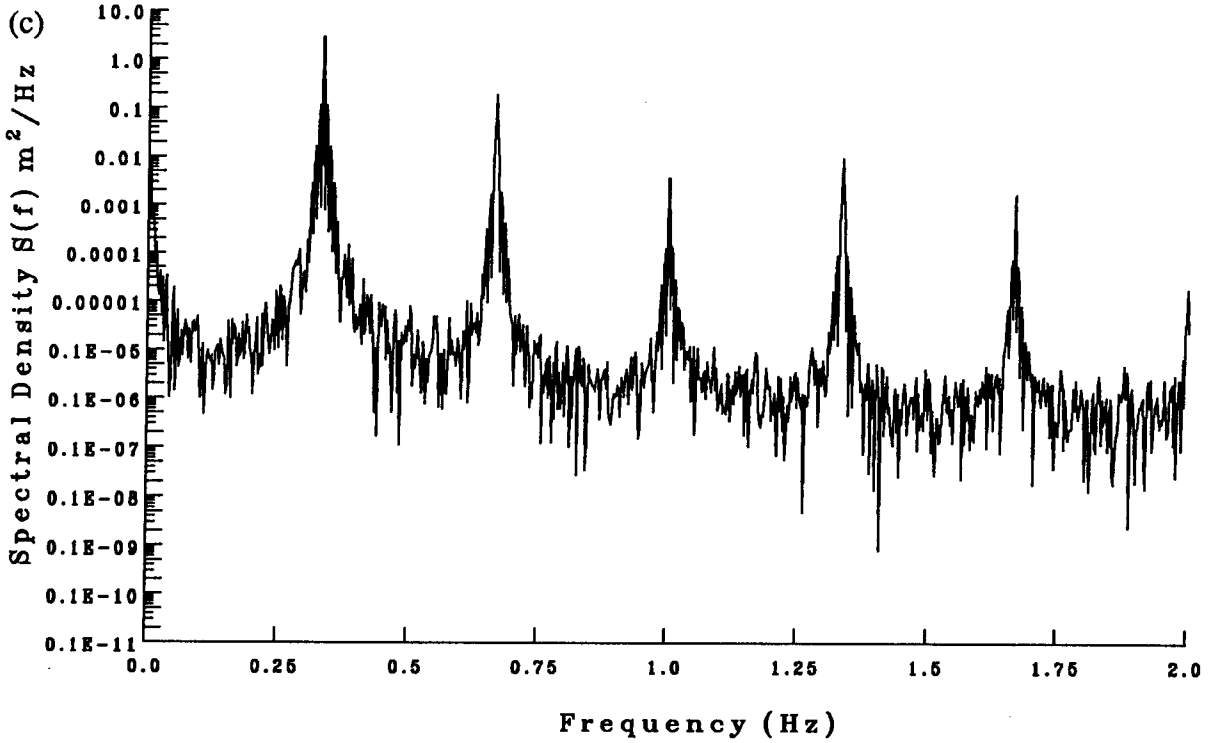
Spectral Density S(f) m²/Hz
10.0
1.0
0.1
0.01
0.001
0.0001
0.00001
0.1E-05
0.1E-06
0.1E-07
0.1E-08
0.1E-09
0.1E-10
0.1E-11
0.0
0.25
0.5
0.75
1.0
1.25
1.5
1.75
2.0
Frequency (Hz)

(d)

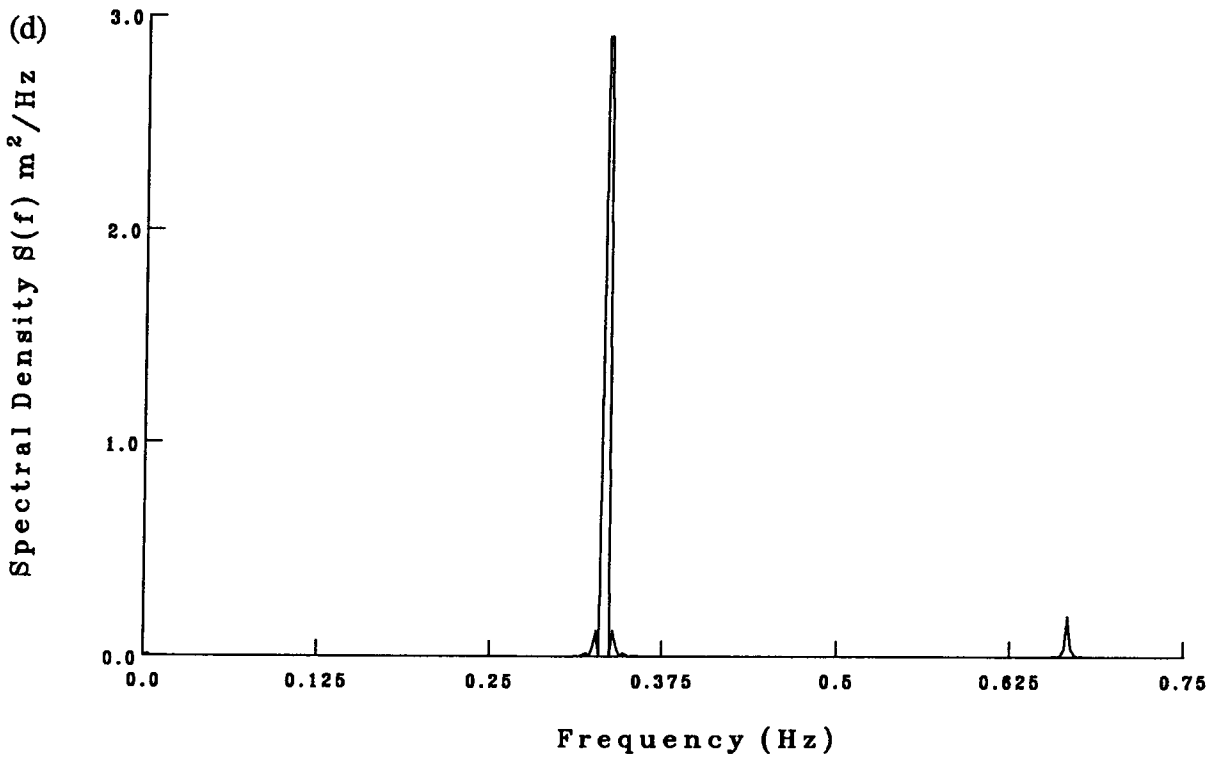
Spectral Density S(f) m²/Hz
3.0
2.0
1.0
0.0
0.0
0.125
0.25
0.375
0.5
0.625
0.75
Frequency (Hz)

(a)

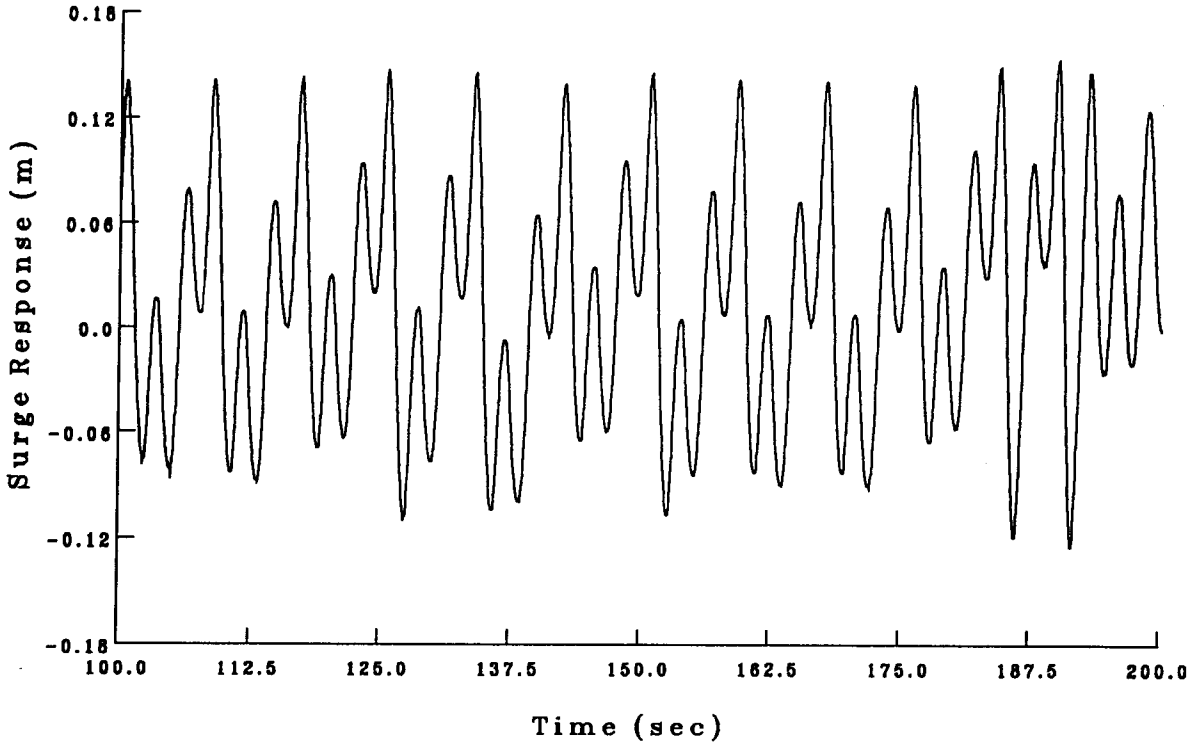

(b)

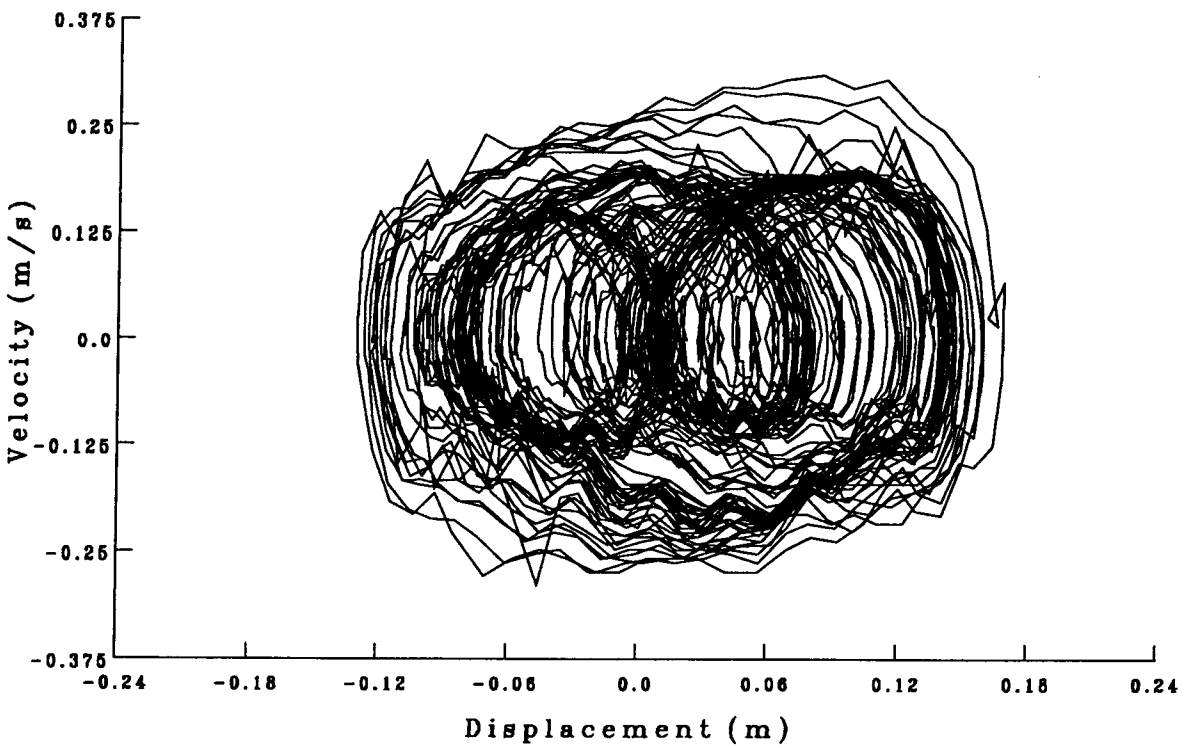

Fig 4.8 - Surge response for monochromatic Excitation
(a) Time series (b) Phase portrait (c) Spectrum - logarithmic (d) Spectrum - linear
H = 11 cm, T = 2.8 s, α =0.378, K = 4.25, d_g= 11.5 cm

(c)

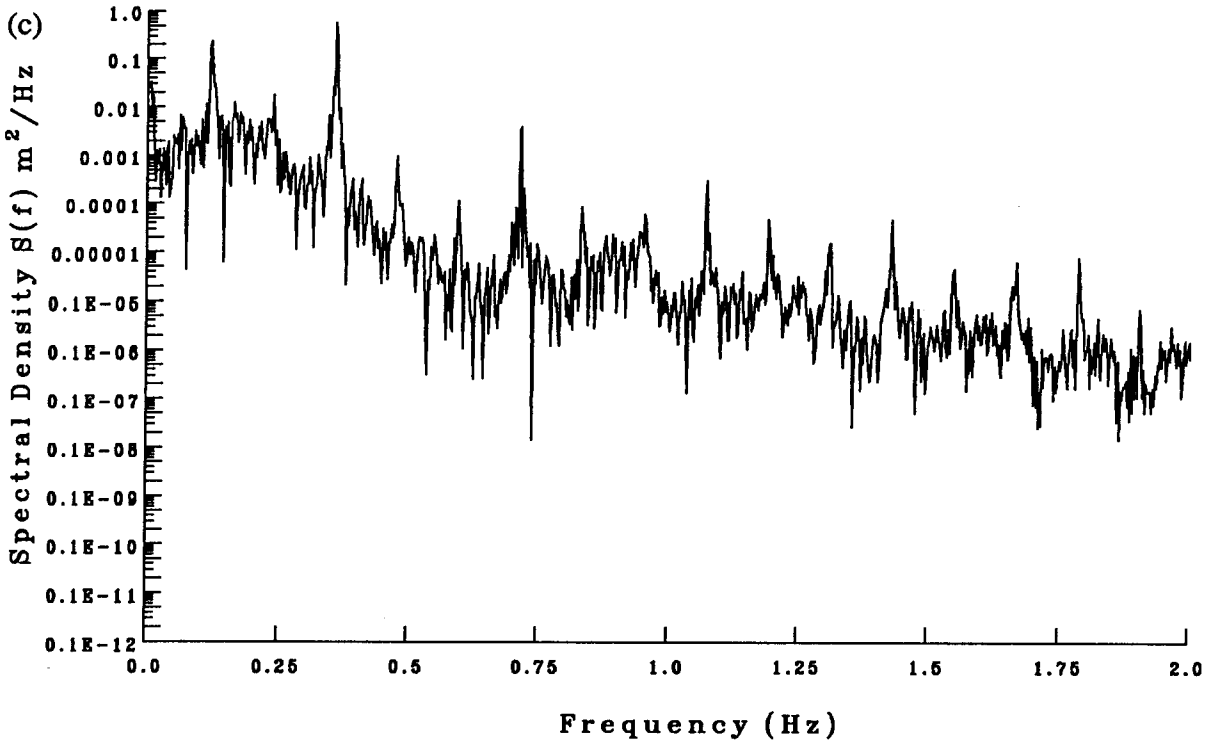
Spectral Density S(f) m²/Hz
1.0
0.1
0.01
0.001
0.0001
0.00001
0.1E-05
0.1E-06
0.1E-07
0.1E-08
0.1E-09
0.1E-10
0.1E-11
0.1E-12
0.0
0.25
0.5
0.75
1.0
1.25
1.5
1.75
2.0
Frequency (Hz)

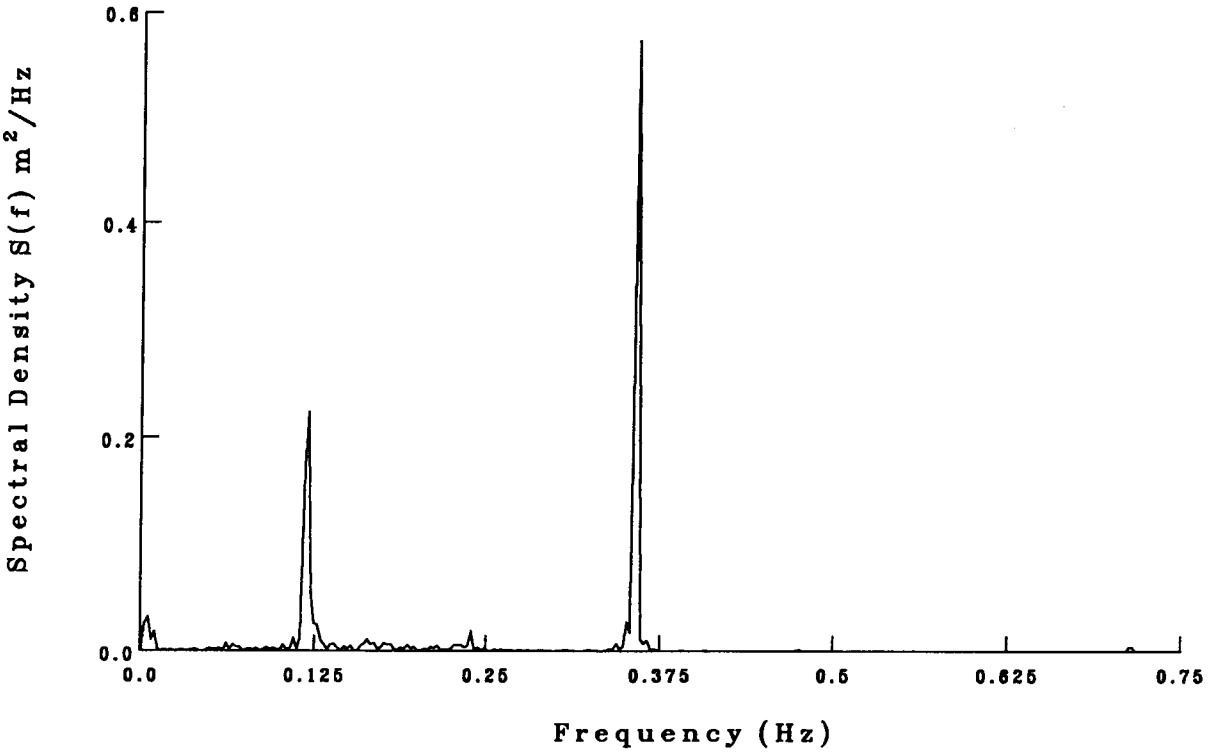
Spectral Density S(f) m²/Hz
0.6
0.4
0.2
0.0
0.0
0.125
0.25
0.375
0.5
0.625
0.75
Frequency (Hz)

(a)

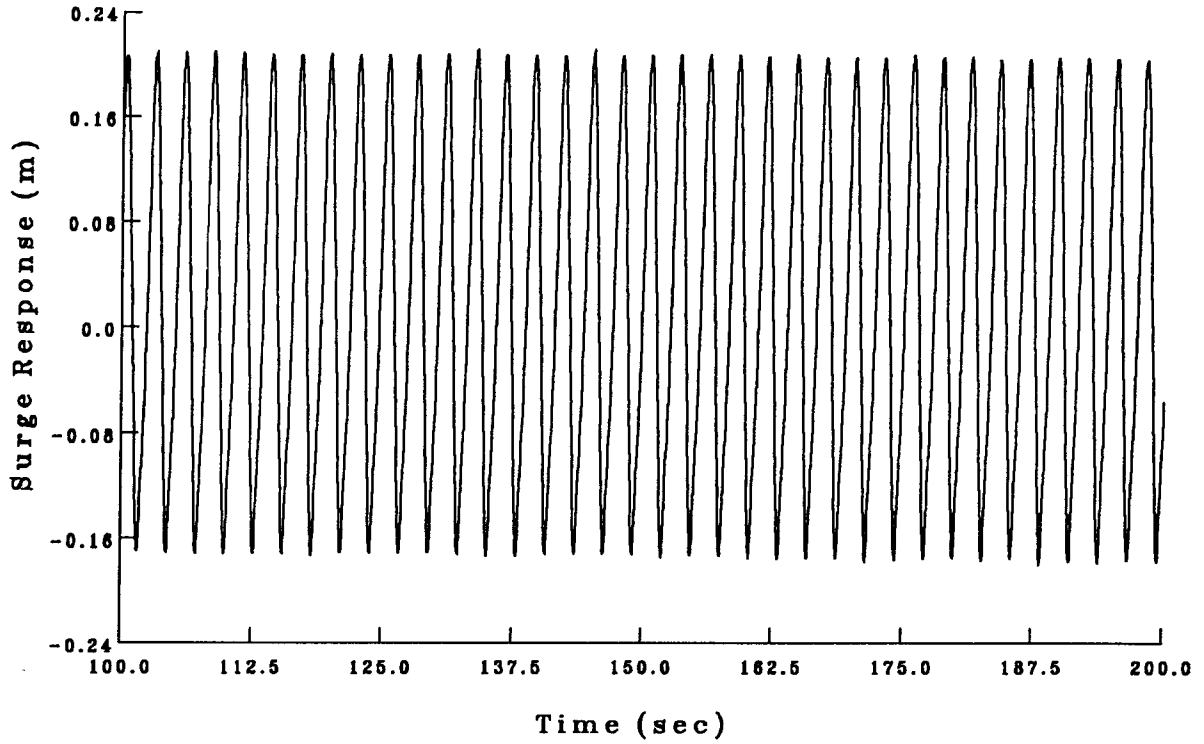

(b)

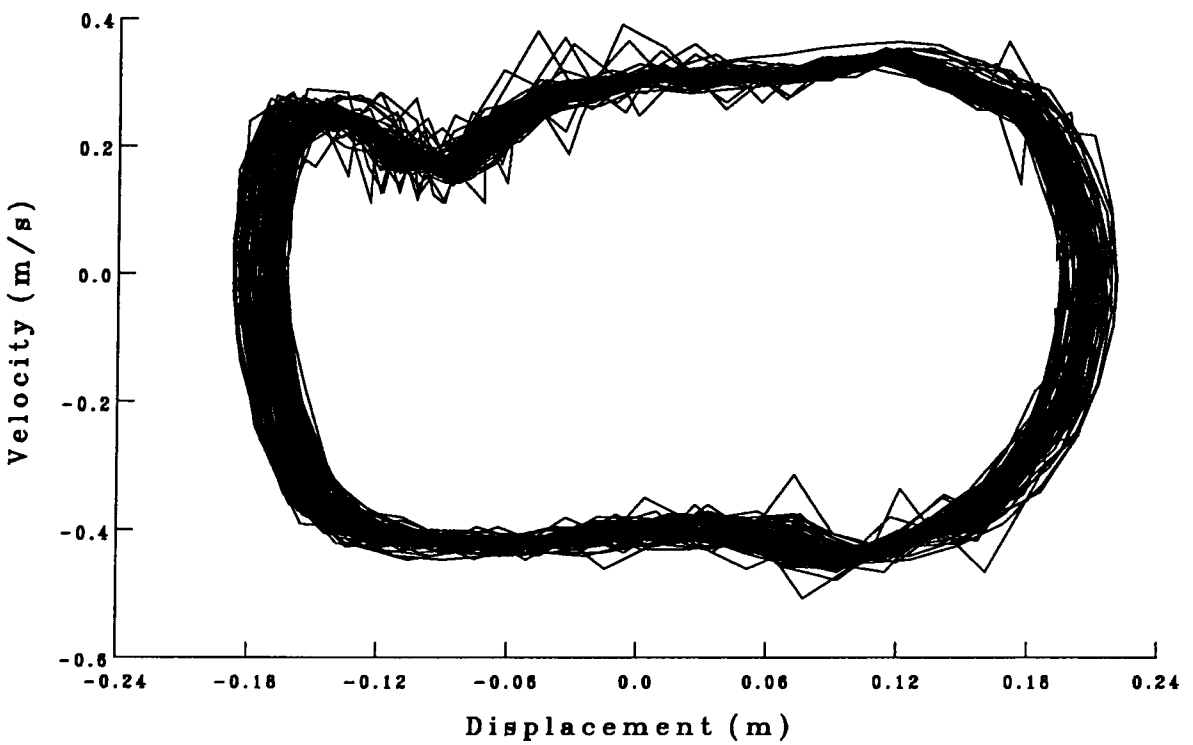

Fig 4.9 - Surge response for monochromatic Excitation
(a) Time series (b) Phase portrait (c) Spectrum - logarithmic (d) Spectrum - linear
H = 15 cm, T = 2.8 s, α = 0.378, K = 4.25, d_g= 11.5 cm

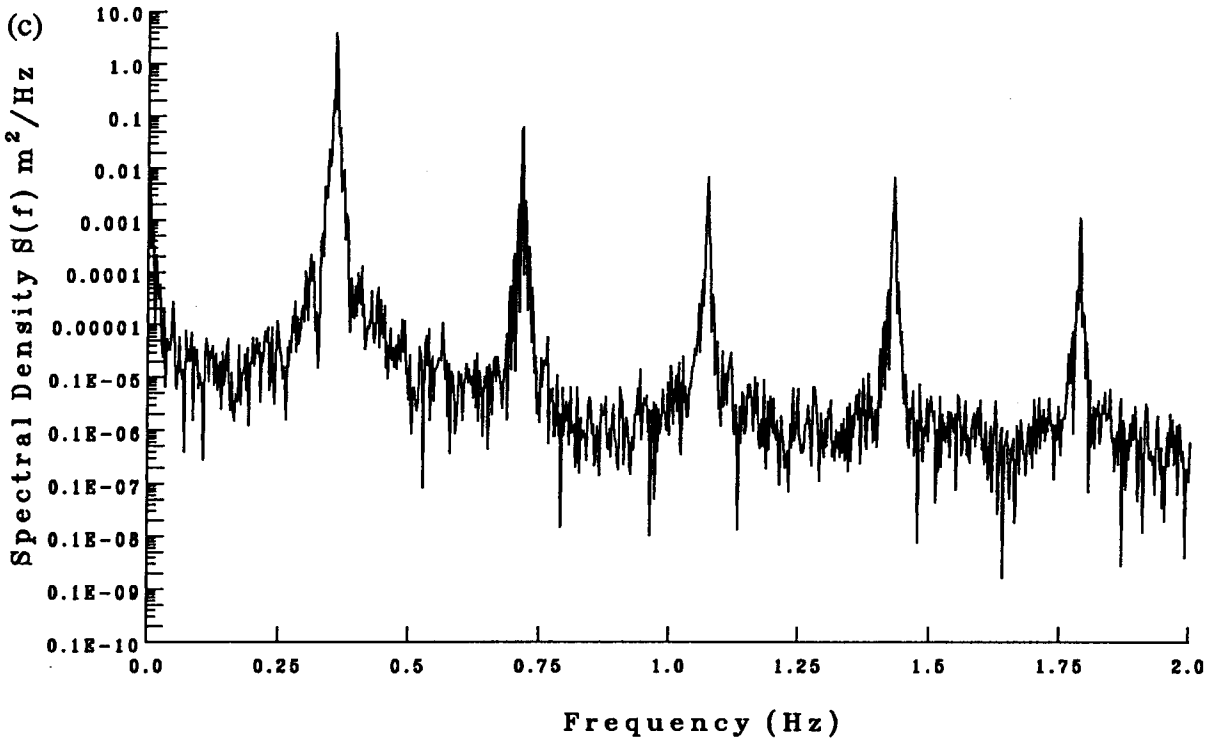
(c)
Spectral Density S(f) m²/Hz
10.0
1.0
0.1
0.01
0.001
0.0001
0.00001
0.1E-05
0.1E-06
0.1E-07
0.1E-08
0.1E-09
0.1E-10
0.0
0.25
0.5
0.75
1.0
1.25
1.5
1.75
2.0
Frequency (Hz)

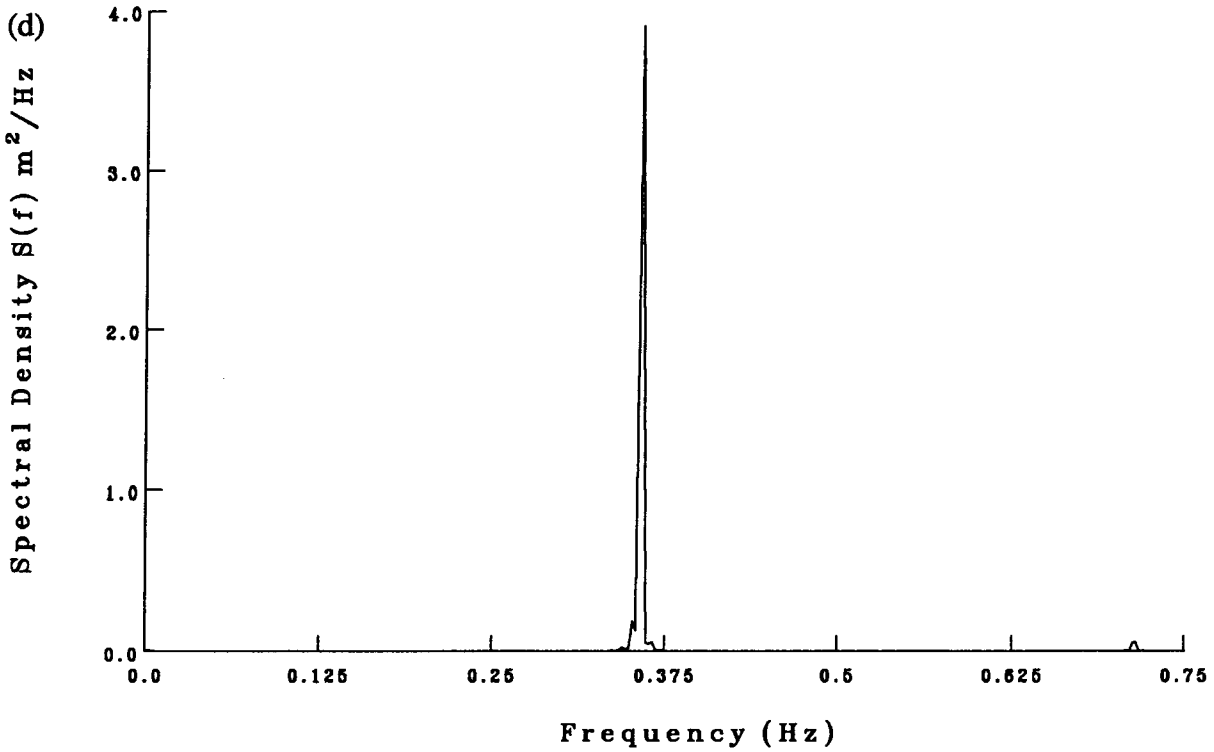
(d)
Spectral Density S(f) m²/Hz
4.0
3.0
2.0
1.0
0.0
0.0
0.125
0.25
0.375
0.5
0.625
0.75
Frequency (Hz)

(a)

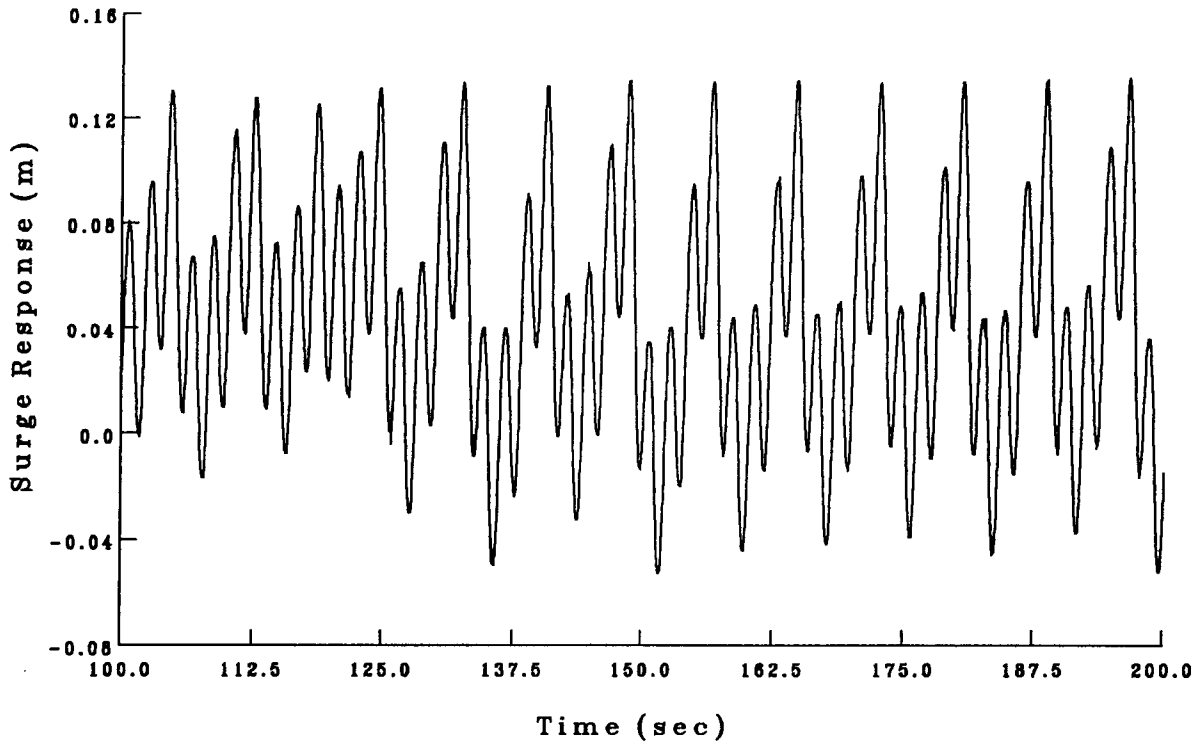

(b)

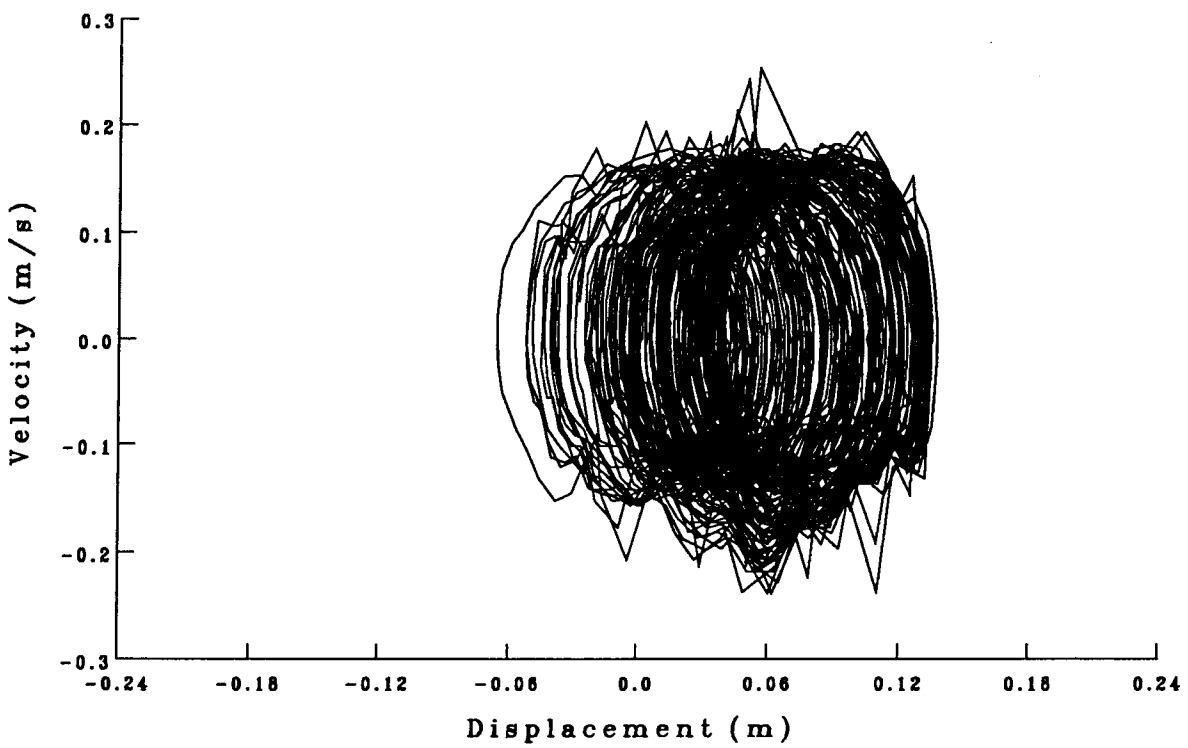

Fig 4.10 - Surge response for monochromatic Excitation
(a) Time series (b) Phase portrait (c) Spectrum - logarithmic (d) Spectrum - linear
H = 11 cm, T = 2.0 s, α = 0.529, K = 4.25, d_g = 11.5 cm

(c)

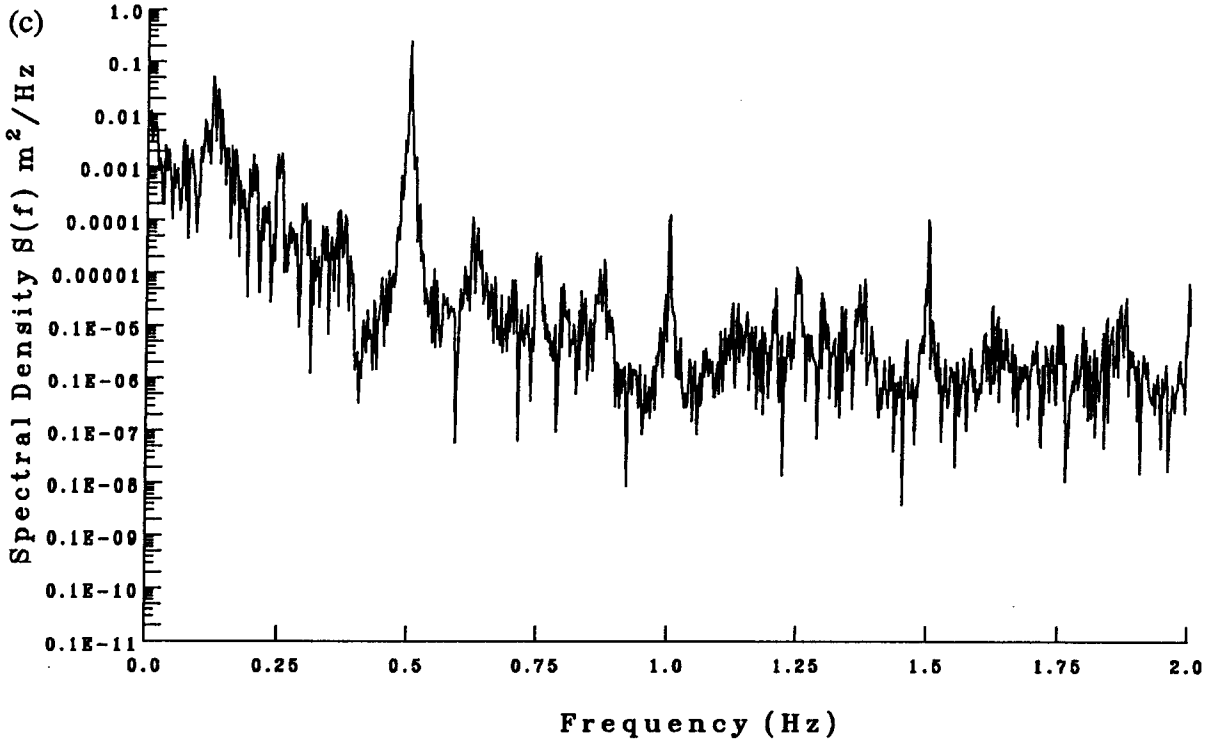
Spectral Density S(f) m²/Hz
1.0
0.1
0.01
0.001
0.0001
0.00001
0.1E-05
0.1E-06
0.1E-07
0.1E-08
0.1E-09
0.1E-10
0.1E-11
0.0
0.25
0.5
0.75
1.0
1.25
1.5
1.75
2.0
Frequency (Hz)

(d)

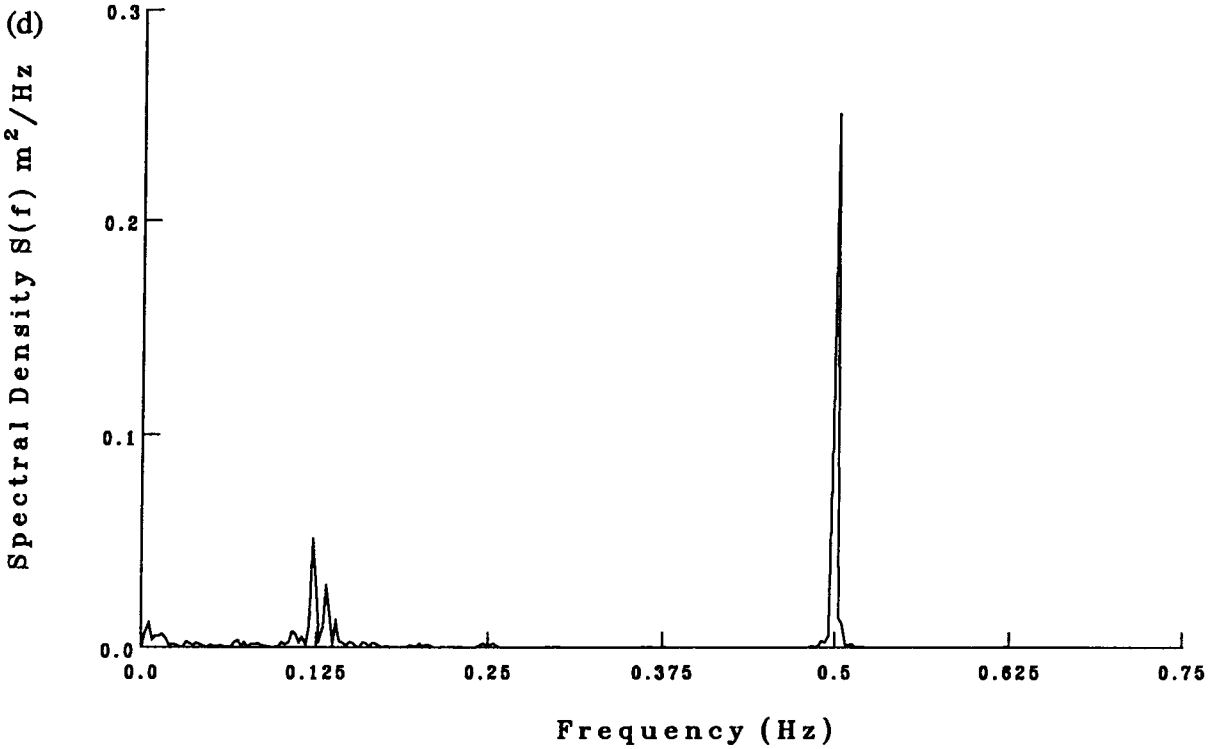
Spectral Density S(f) m²/Hz
0.3
0.2
0.1
0.0
0.0
0.125
0.25
0.375
0.5
0.625
0.75
Frequency (Hz)

(a)

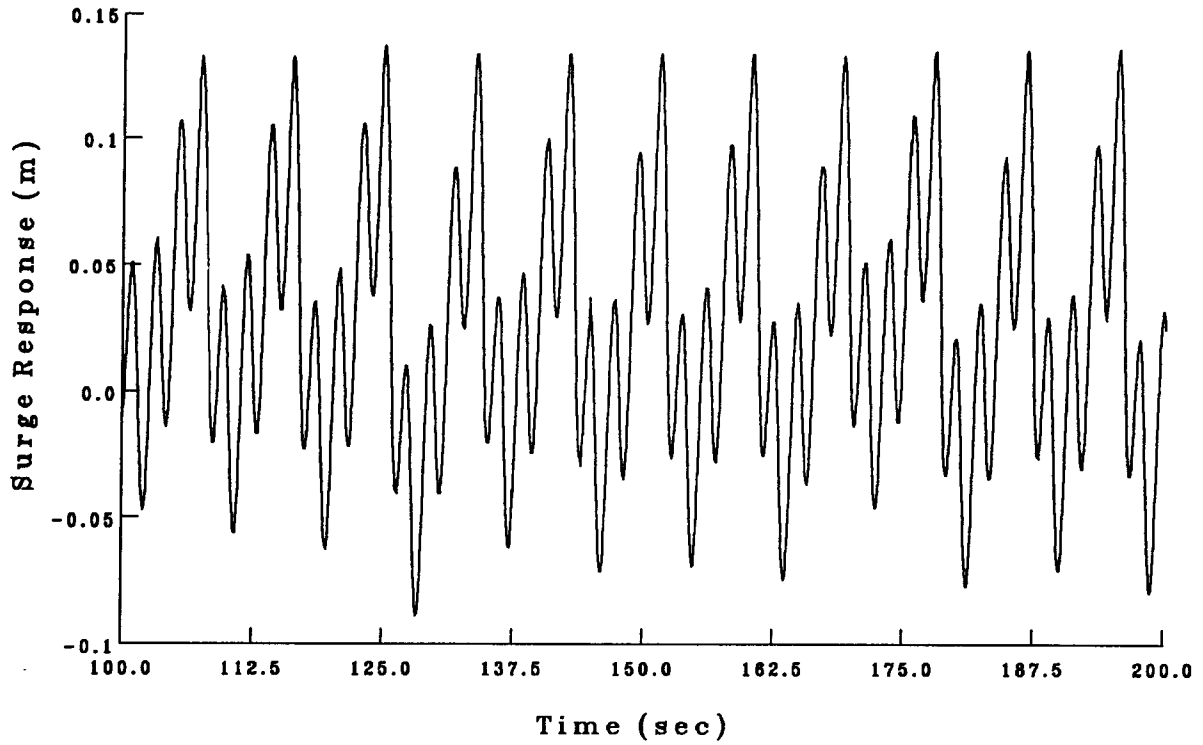

(b)

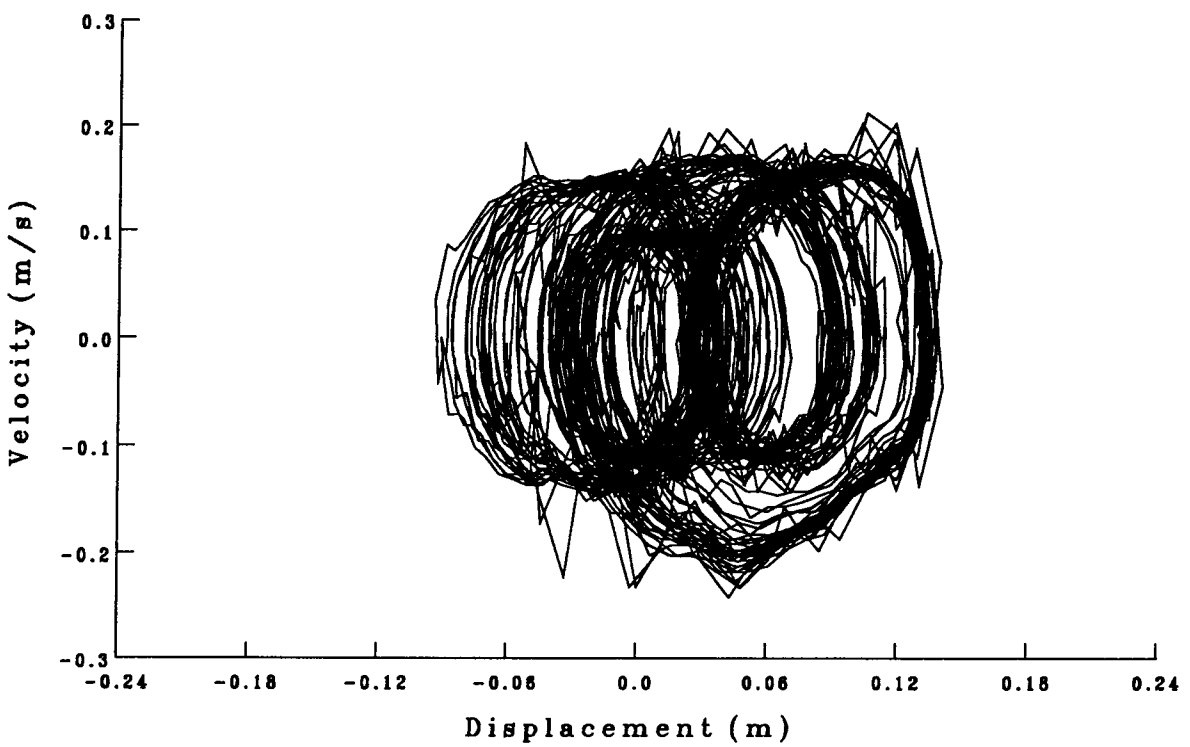

Fig 4.11 - Surge response for monochromatic Excitation
(a) Time series (b) Phase portrait (c) Spectrum - logarithmic (d) Spectrum - linear
H = 11 cm, T = 2.2 s, α = 0.481, K = 4.25, d_g = 11.5 cm

(c)

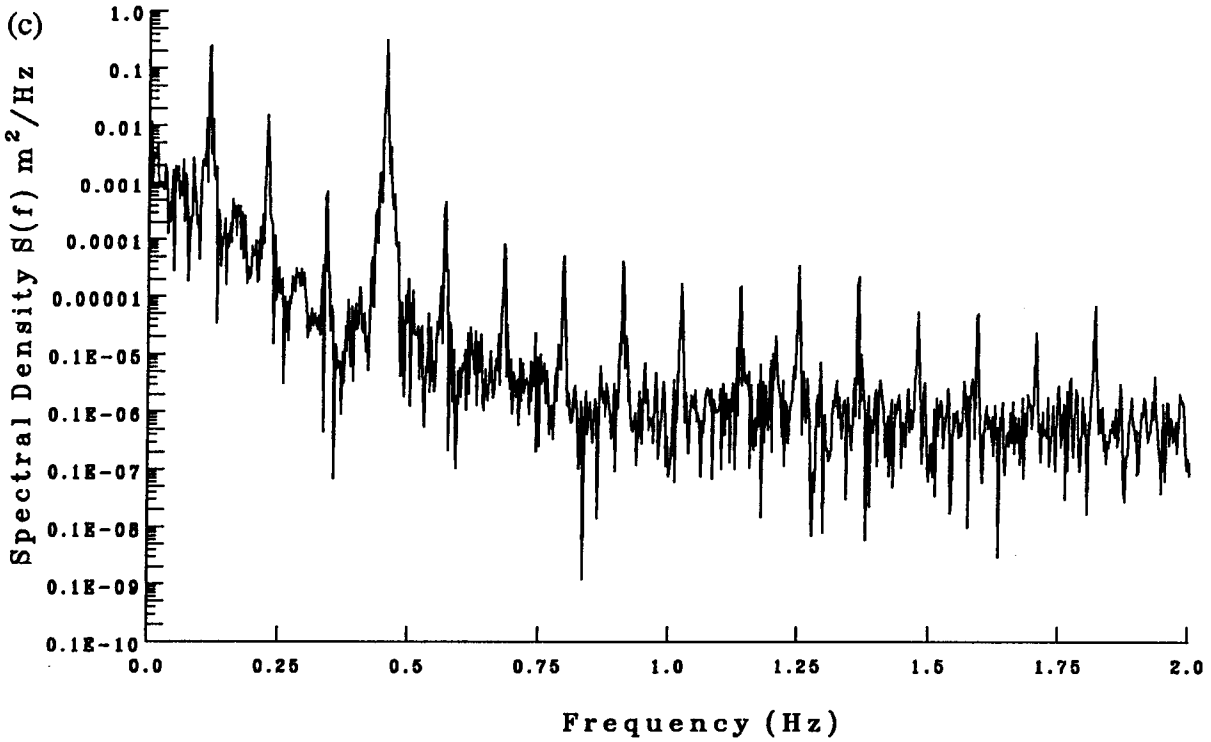
Spectral Density S(f) m²/Hz
1.0
0.1
0.01
0.001
0.0001
0.00001
0.1E-05
0.1E-06
0.1E-07
0.1E-08
0.1E-09
0.1E-10
0.0
0.25
0.5
0.75
1.0
1.25
1.5
1.75
2.0
Frequency (Hz)

(d)

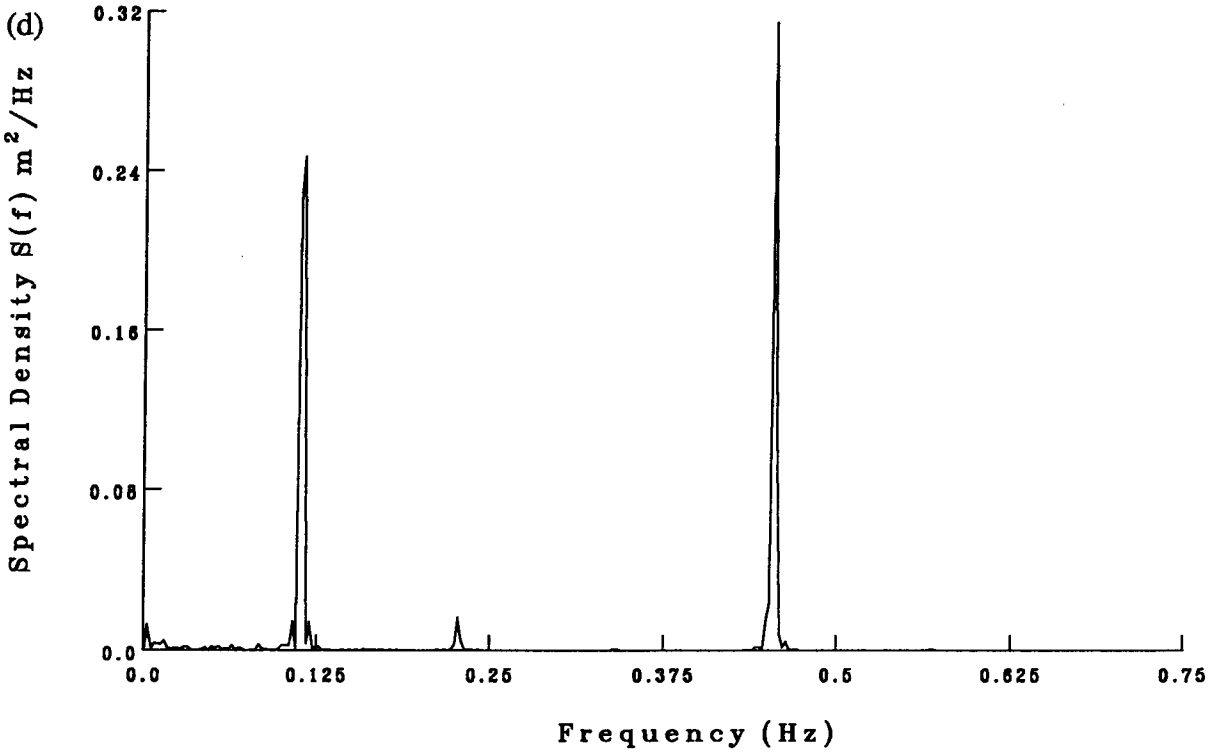
Spectral Density S(f) m²/Hz
0.32
0.24
0.16
0.08
0.0
0.0
0.125
0.25
0.375
0.5
0.625
0.75
Frequency (Hz)

(a)

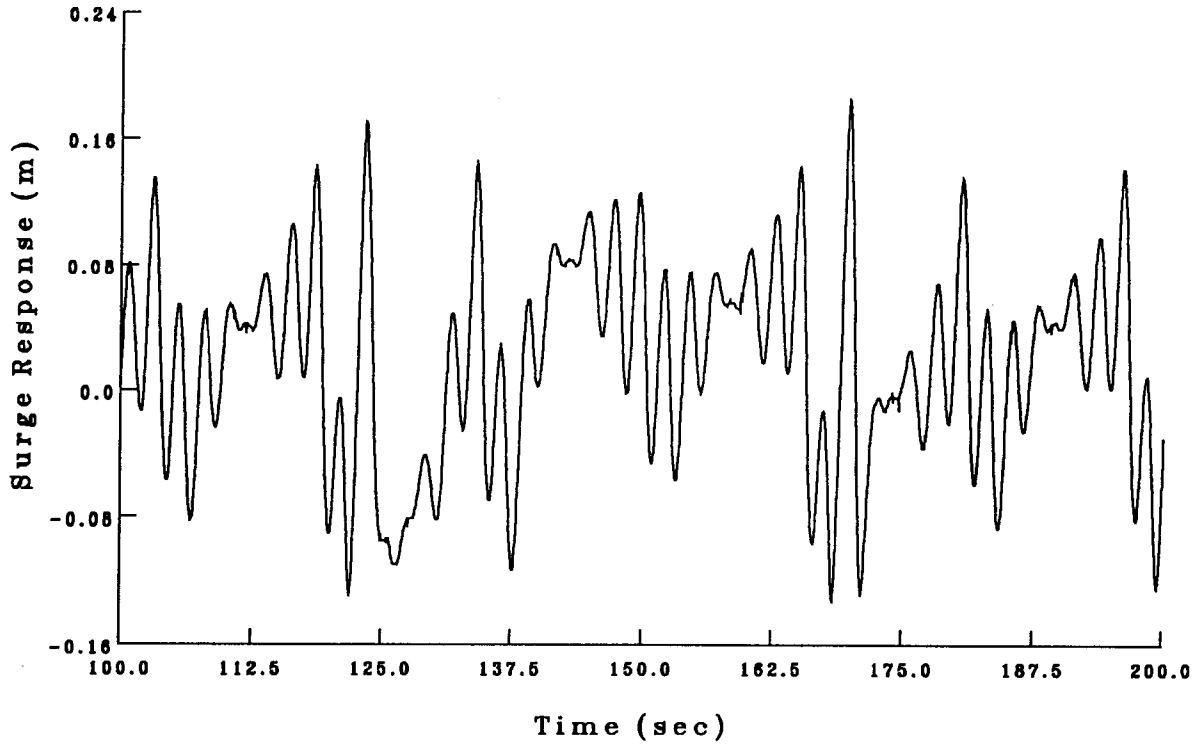

(b)

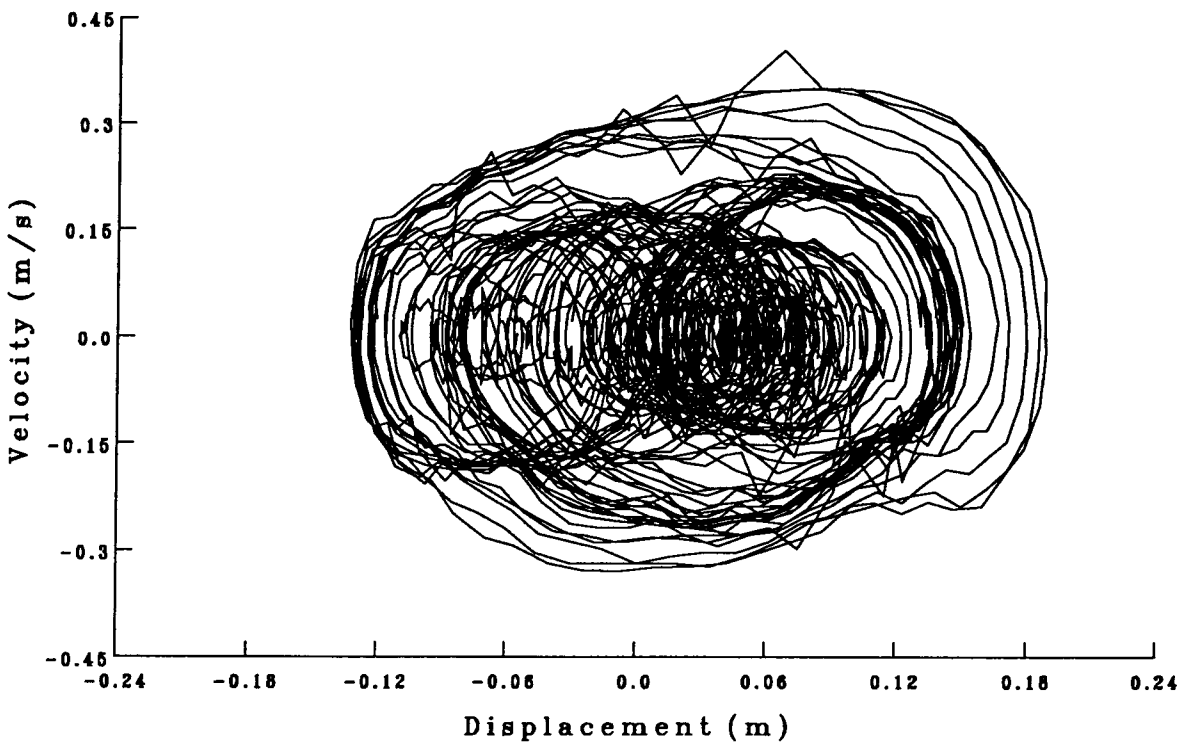

Fig. 4.12 Surge response for bi-chromatic excitation
(a) Time series (b) Phase portrait (c) Spectrum - logarithmic (d) Spectrum - linear
$H_1 = 7.0$ cm, $H_2 = 7.0$ cm, $T_1 = 2.3$ s, $T_2 = 2.7$ s, $\alpha = 0.423$, $K = 4.25$

(c)

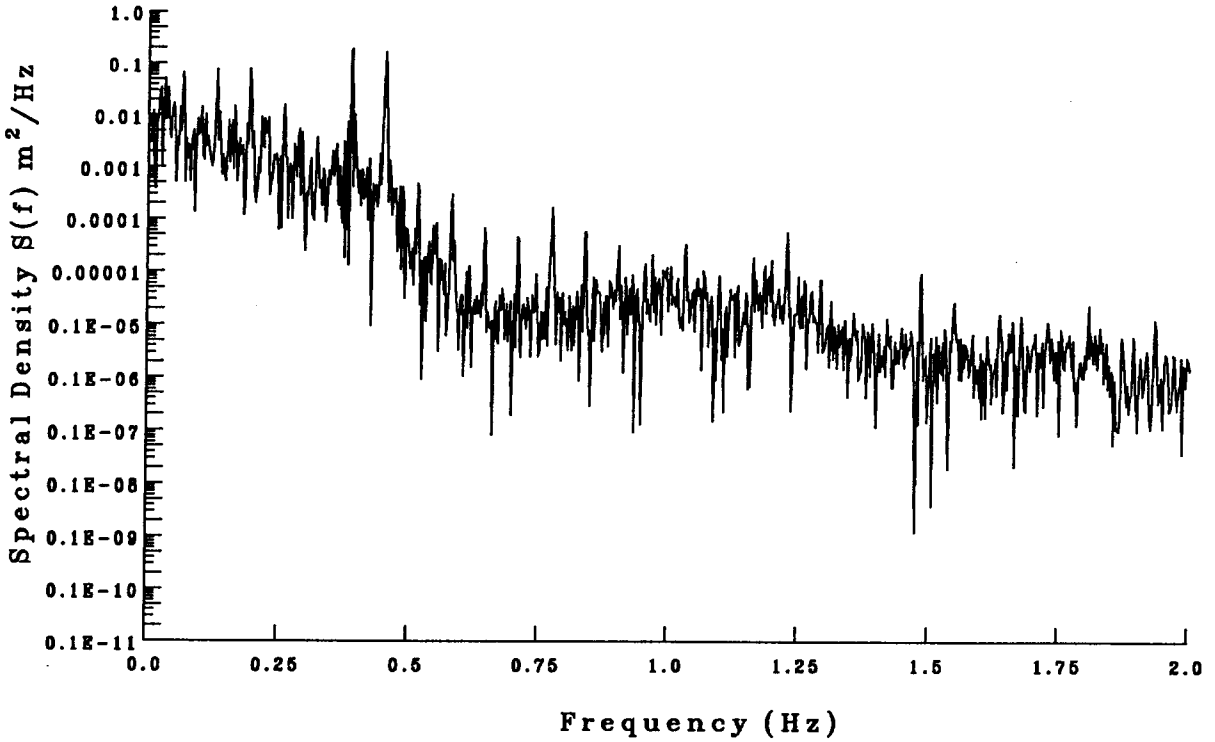
Spectral Density S(f) m²/Hz
1.0
0.1
0.01
0.001
0.0001
0.00001
0.1E-05
0.1E-06
0.1E-07
0.1E-08
0.1E-09
0.1E-10
0.1E-11
0.0
0.25
0.5
0.75
1.0
1.25
1.5
1.75
2.0
Frequency (Hz)

(d)

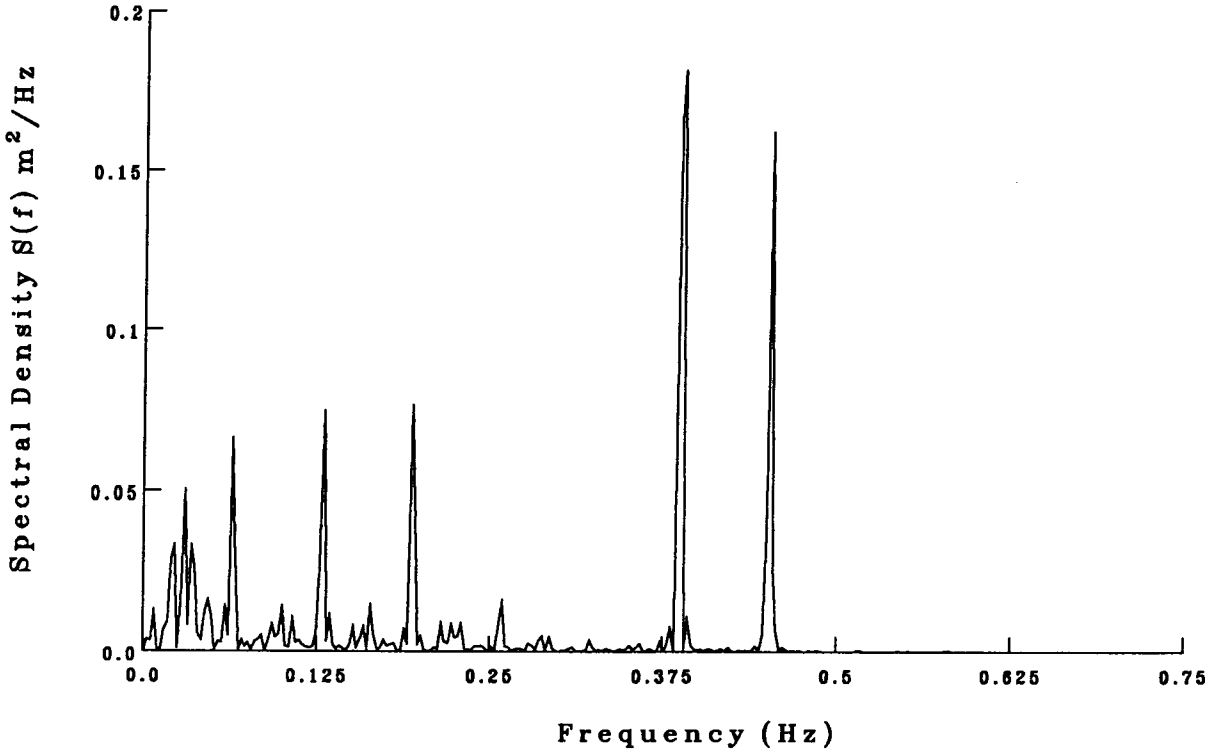
Spectral Density S(f) m²/Hz
0.2
0.15
0.1
0.05
0.0
0.0
0.125
0.25
0.375
0.5
0.625
0.75
Frequency (Hz)

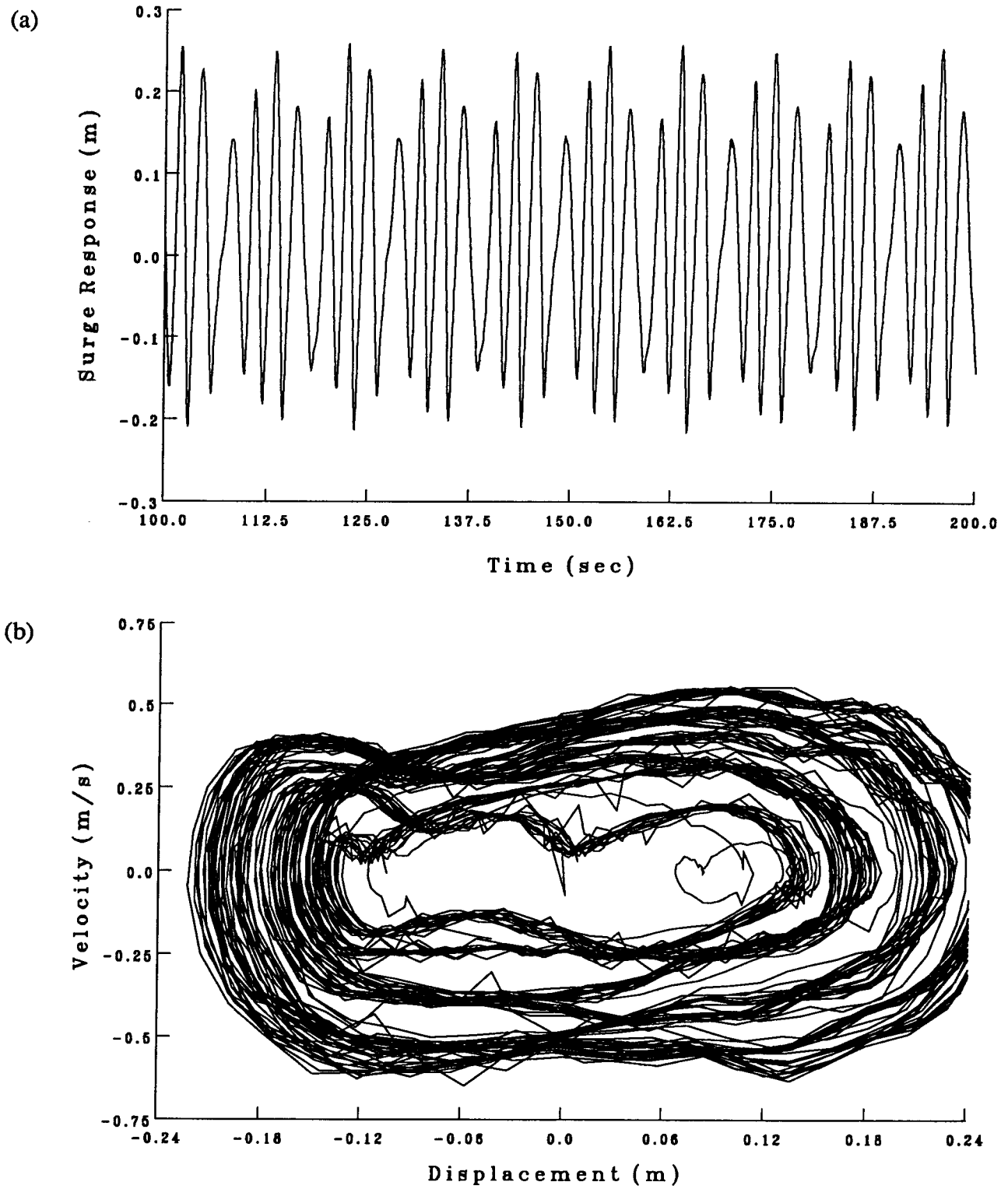

Fig. 4.13 Surge response for bi-chromatic excitation
(a) Time series (b) Phase portrait (c) Spectrum - logarithmic (d) Spectrum - linear
$H_1 = 9.0$ cm, $H_2 = 9.0$ cm, $T_1 = 2.2$ s, $T_2 = 2.8$ s, $\alpha = 0.423$, $K = 4.25$

(c)

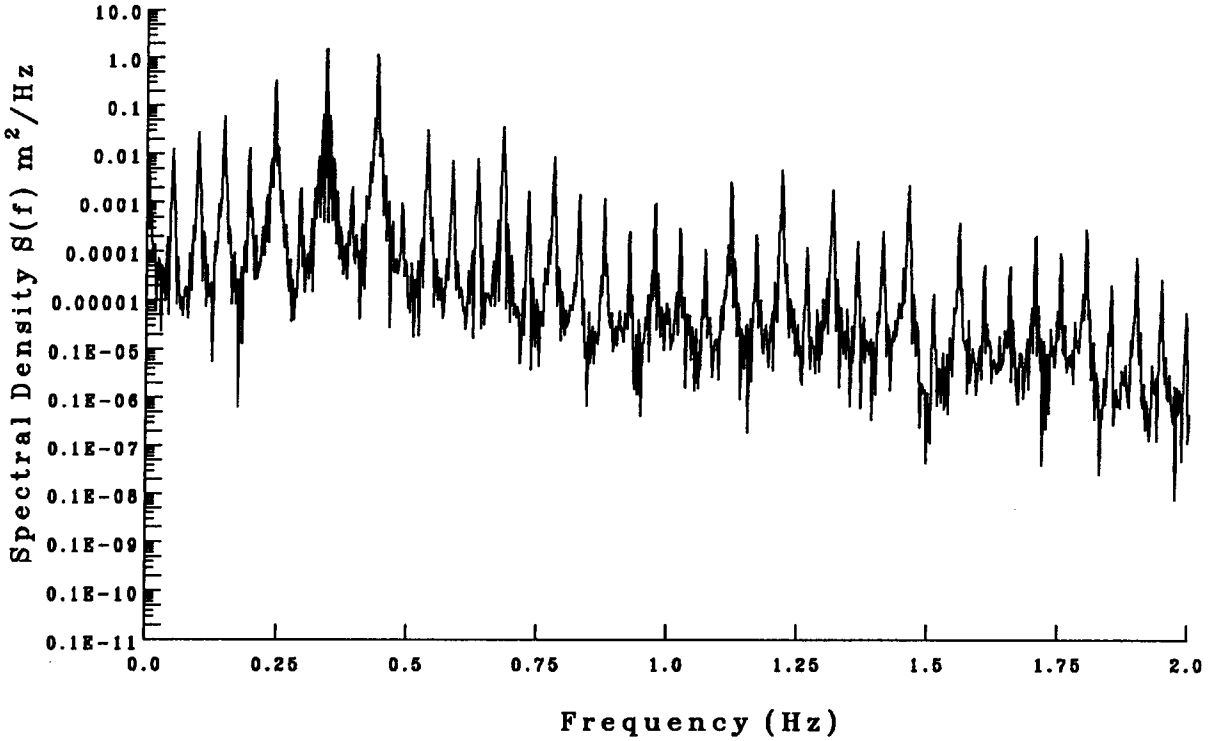
Spectral Density S(f) m²/Hz
10.0
1.0
0.1
0.01
0.001
0.0001
0.00001
0.1E-05
0.1E-06
0.1E-07
0.1E-08
0.1E-09
0.1E-10
0.1E-11
0.0
0.25
0.5
0.75
1.0
1.25
1.5
1.75
2.0
Frequency (Hz)

(d)

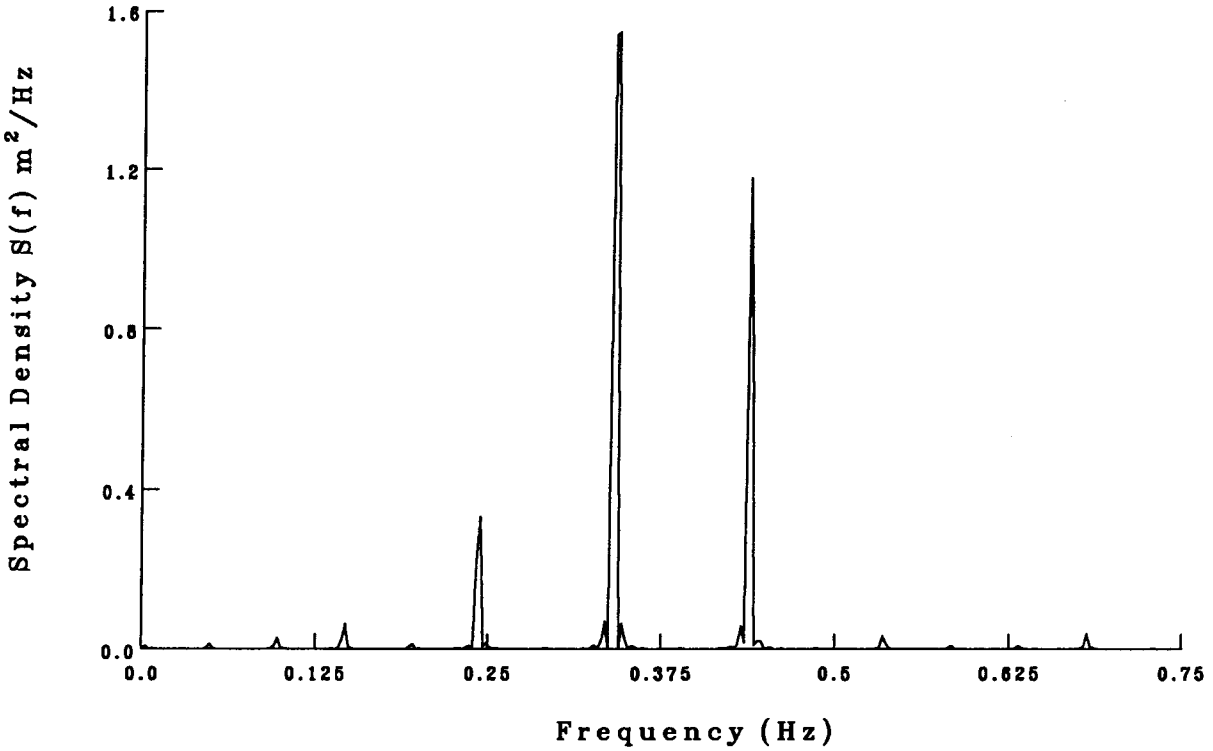
Spectral Density S(f) m²/Hz
1.6
1.2
0.8
0.4
0.0
0.0
0.125
0.25
0.375
0.5
0.625
0.75
Frequency (Hz)

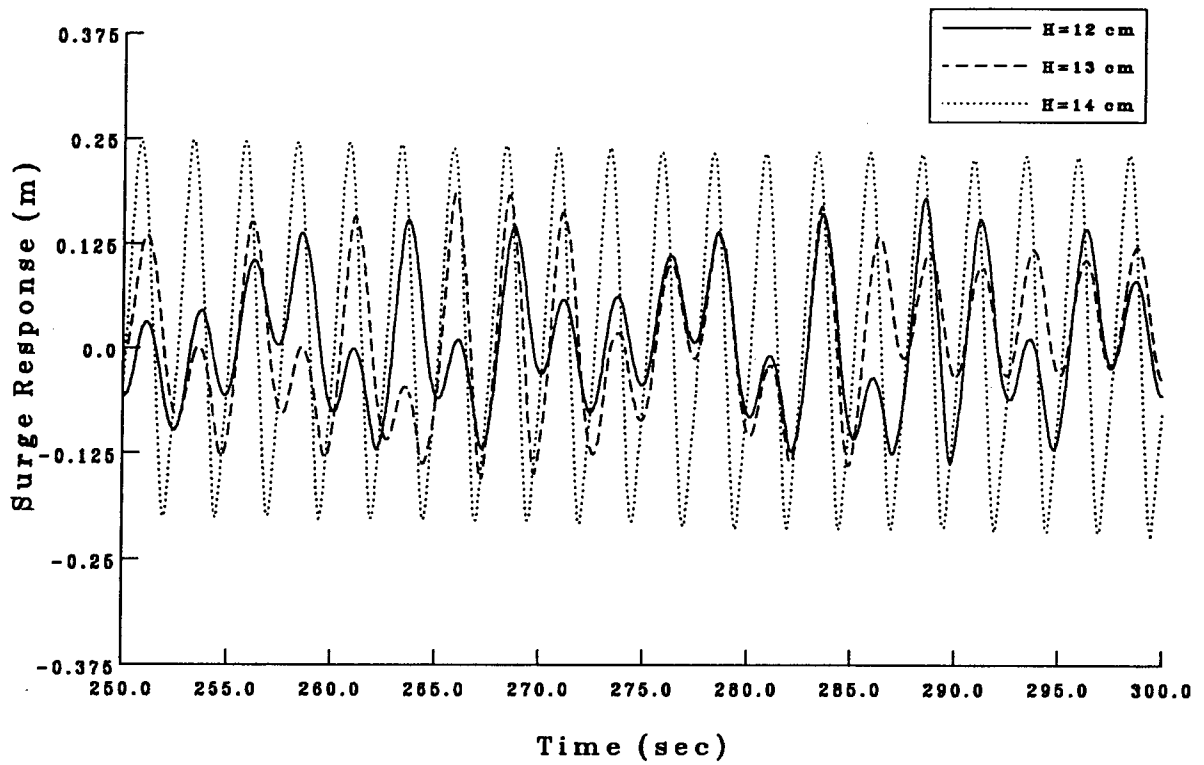

Fig. 4.14 Effect of wave height variation on surge response

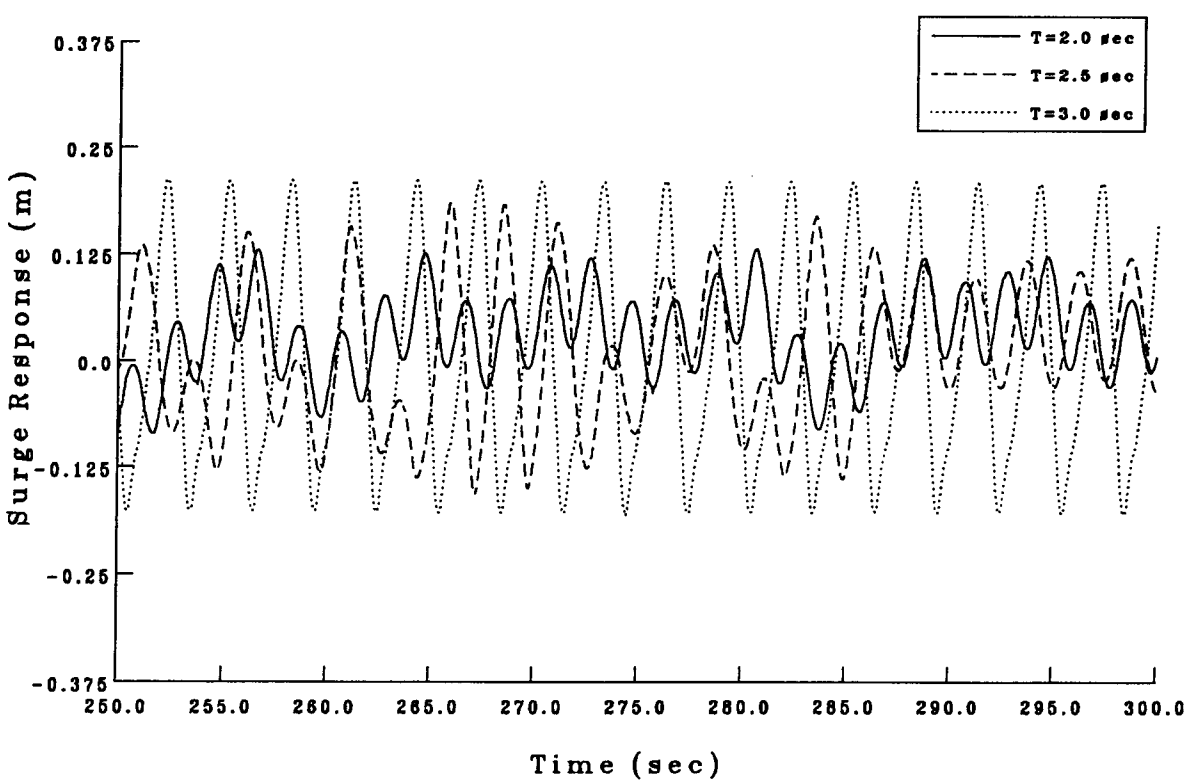

Fig. 4.15 Effect of wave period variation on surge response

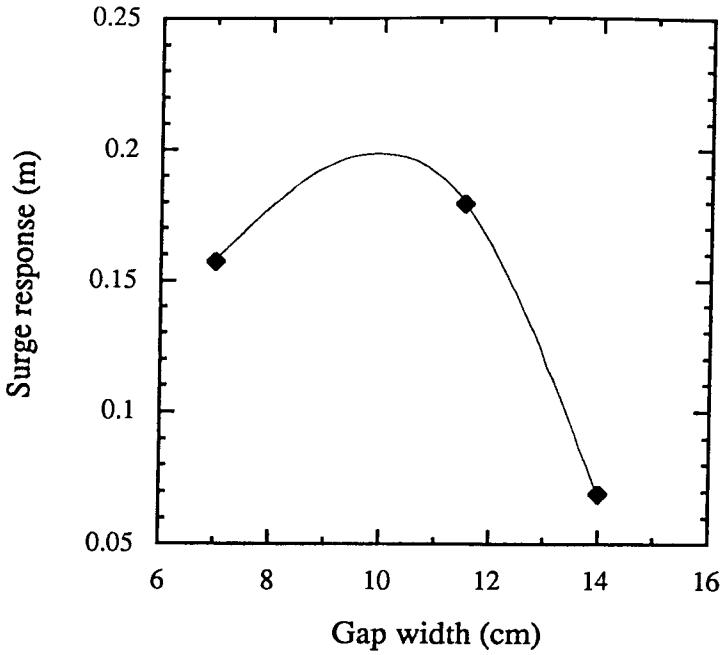

Fig. 4.16 Plot of surge response amplitude vs. gap width

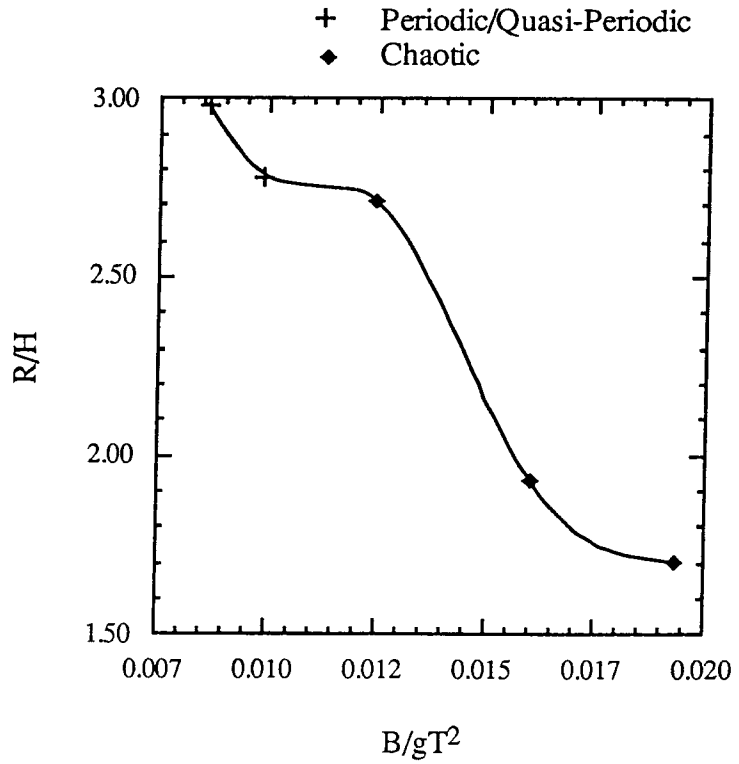

Fig. 4.17 Plot of R/H vs. B/gT^2 for K = 4.25, H = 13 cm

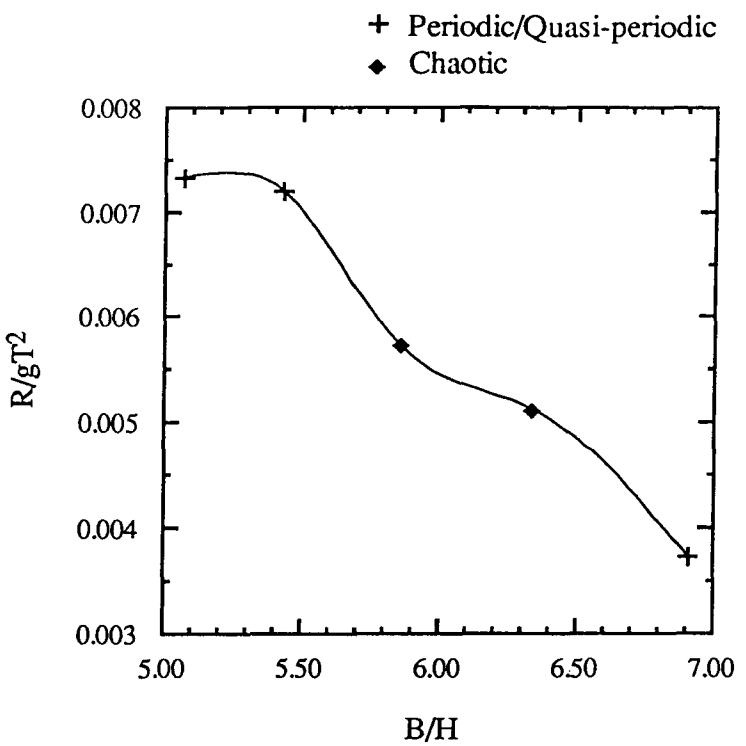

Fig. 4.18 Plot of R/gT^2 vs. B/H for K = 4.25, t = 2.5 s

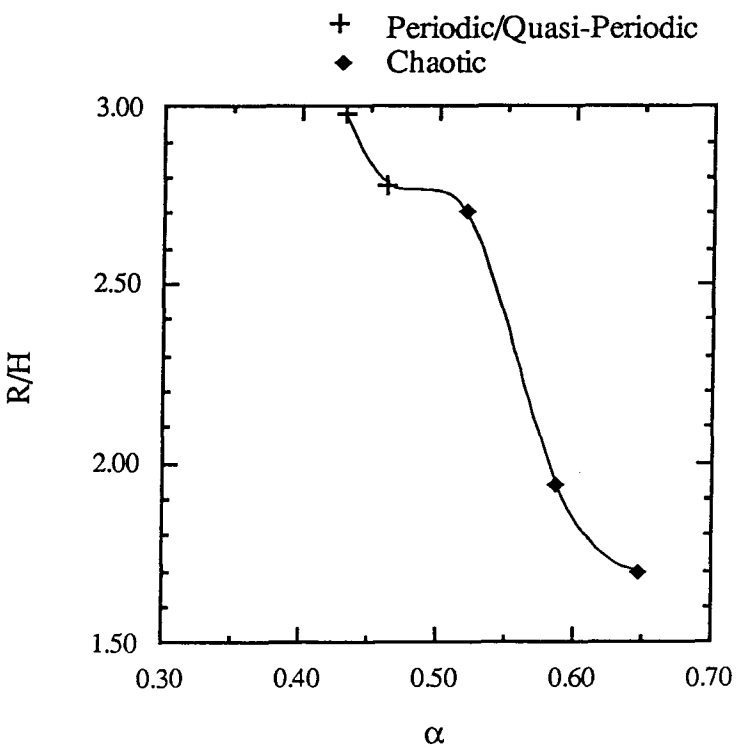

Fig. 4.19 Plot of R/H vs. α for K = 4.25, H = 13 cm

(a)

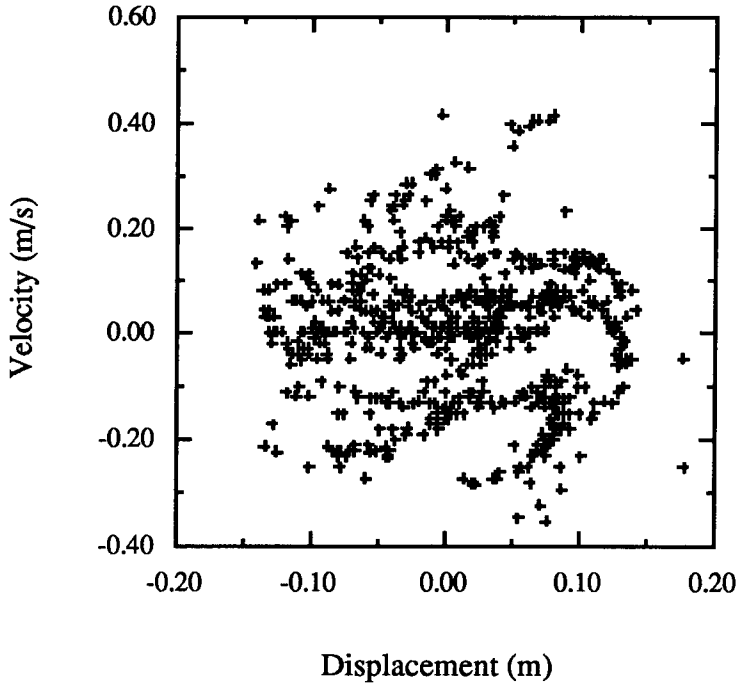

(b)

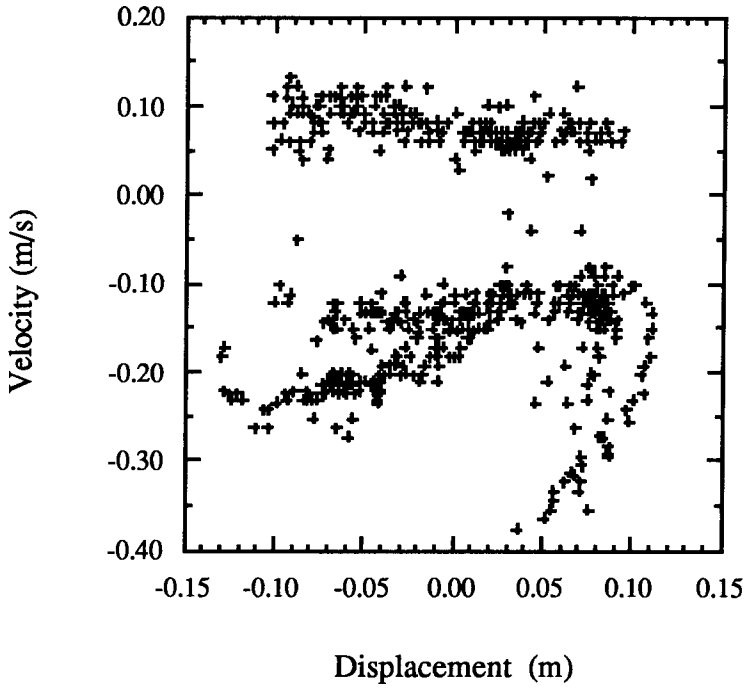

Fig. 4.20 Poincaré map of surge response for bichromatic input
(a) $\tau = 10$ (b) $\tau = 20$

(a)

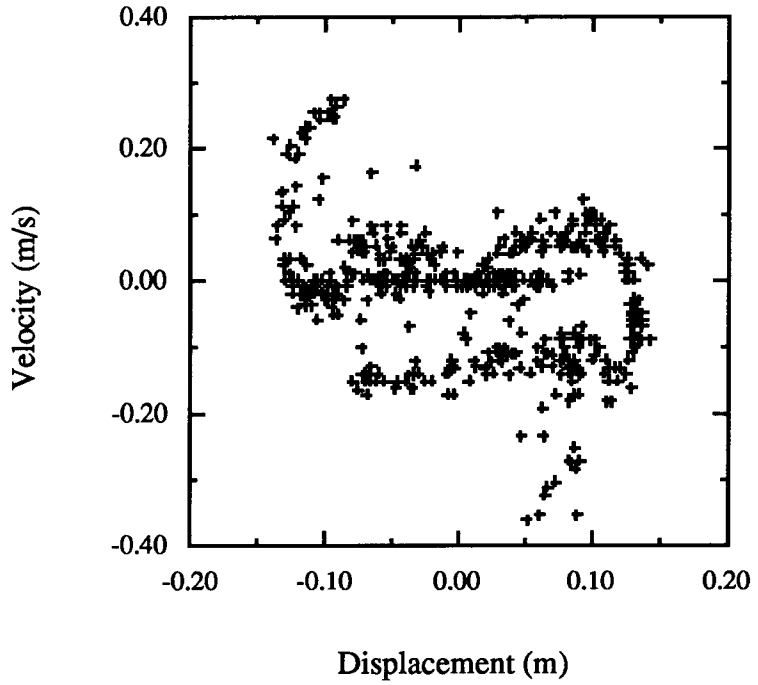

(b)

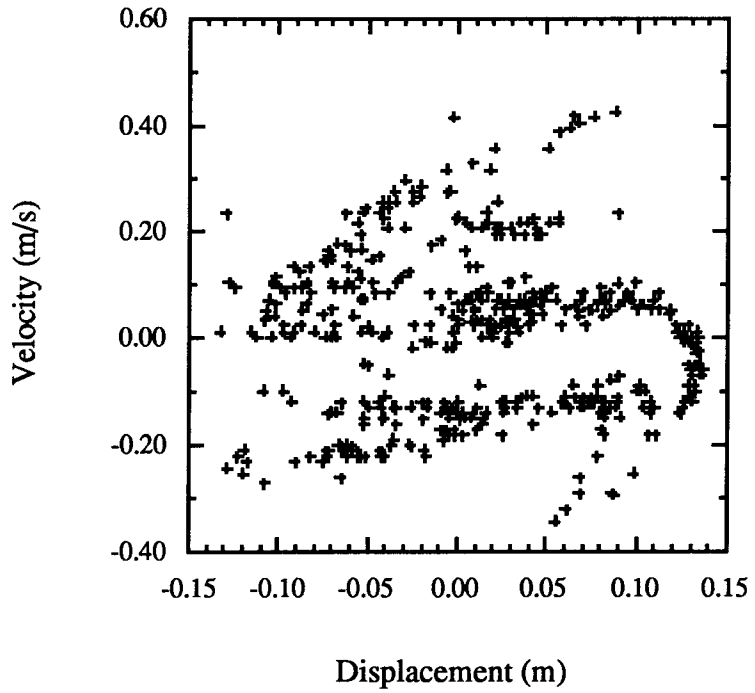

Fig. 4.21 Poincaré map of surge response for bichromatic input
(a) $\tau = 30$ (b) $\tau = 40$

(a)

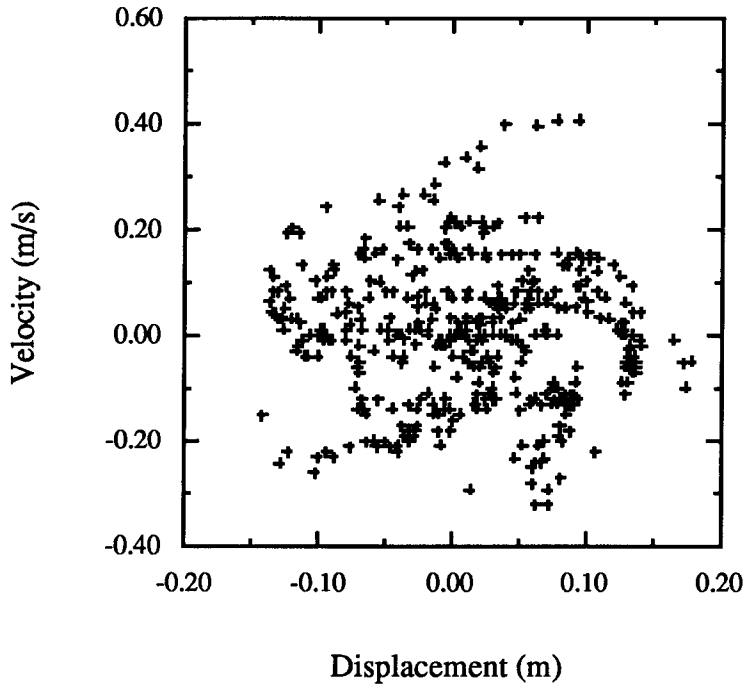

(b)

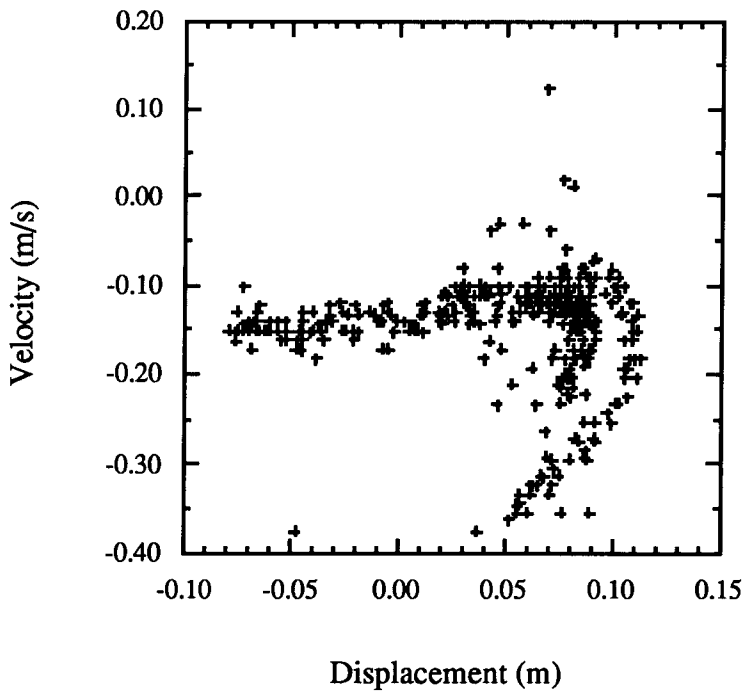

Fig. 4.22 Poincaré map of surge response for bichromatic input
(a) $\tau = 50$ (b) $\tau = 60$

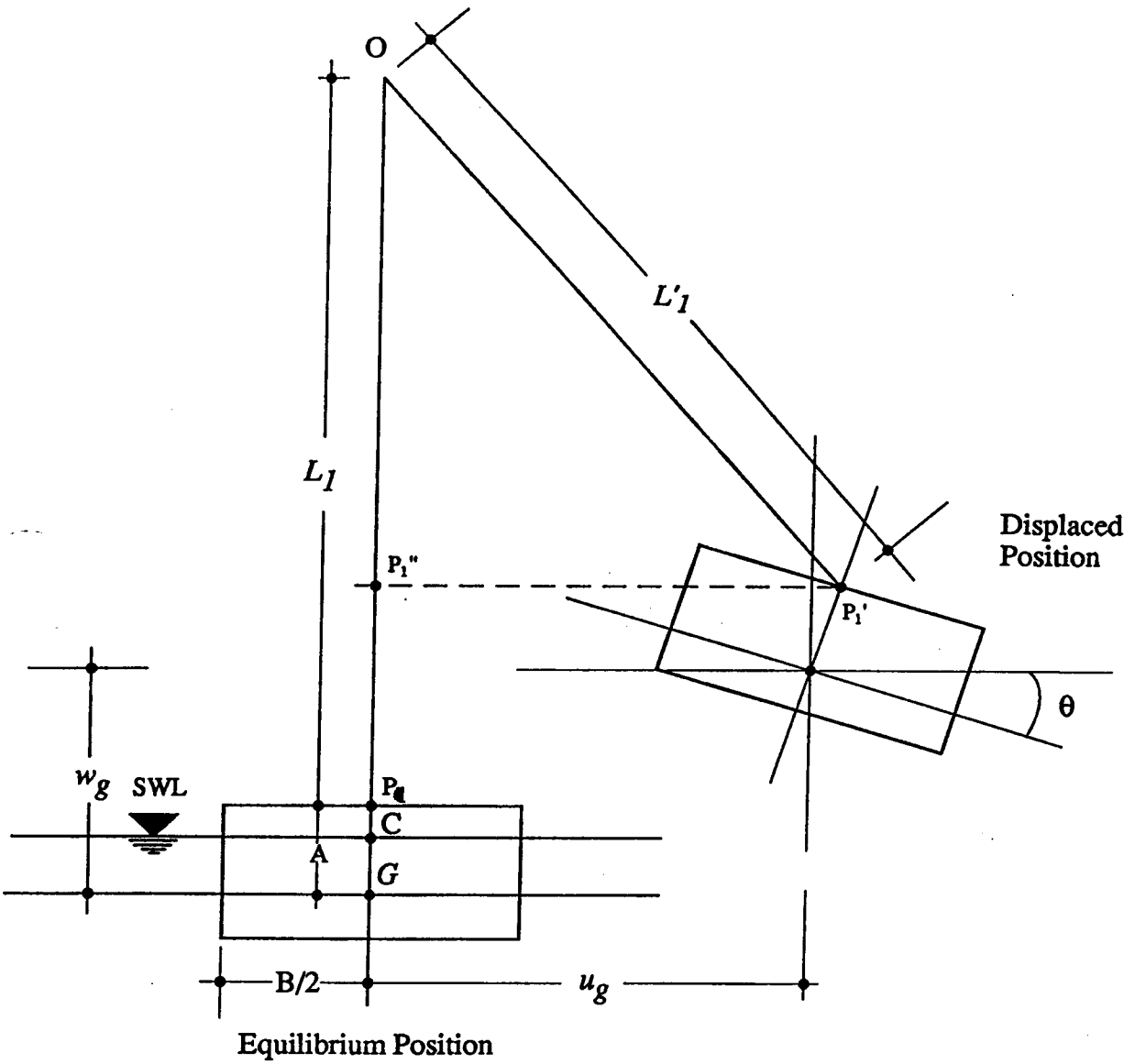

Fig. A-1 Displacement Probe #1, L_1 - original length, L_1' - length at time t

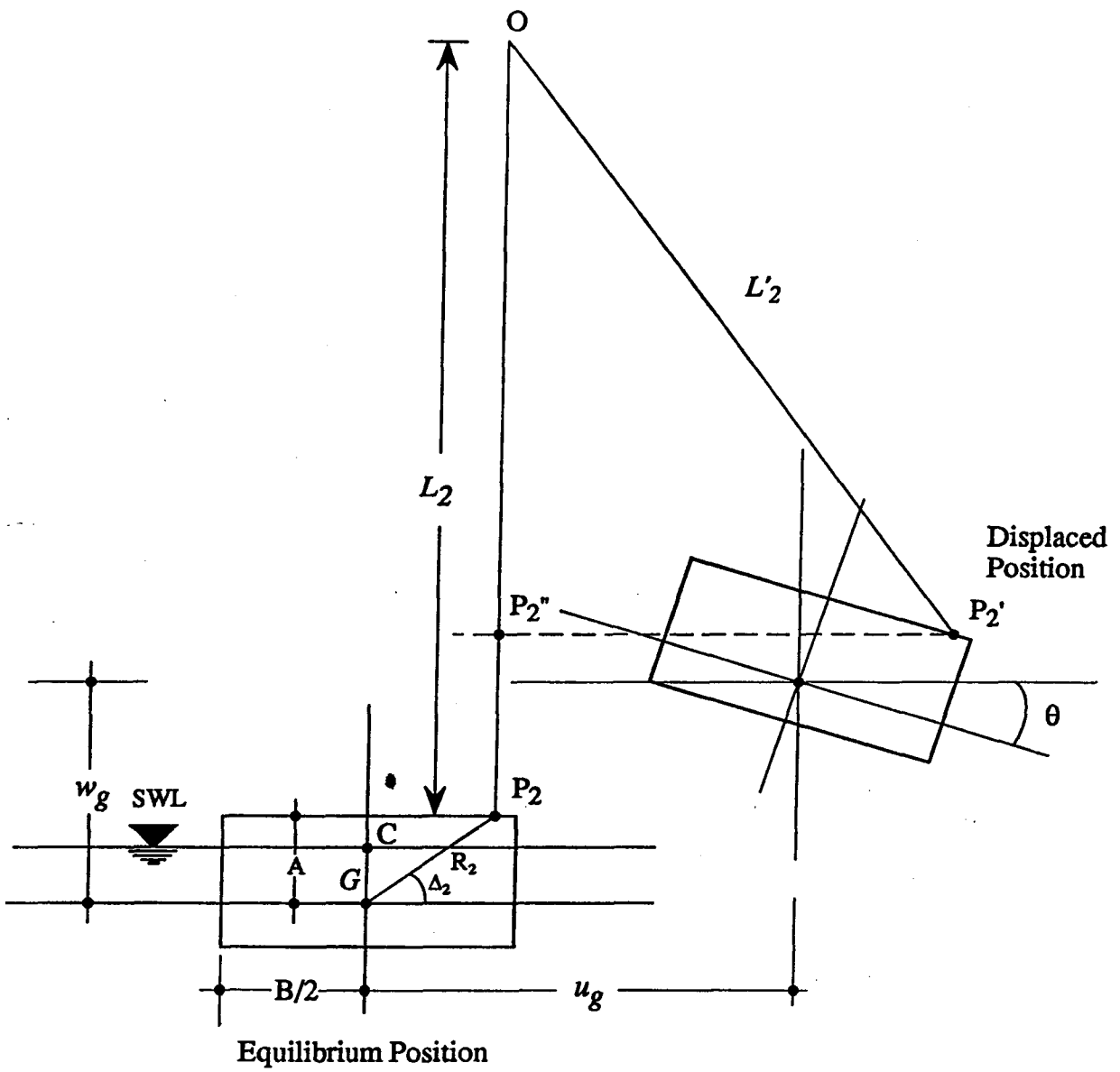

Fig. A-2 Displacement Probe #2, L_2 - original length, L_2' - length at time t

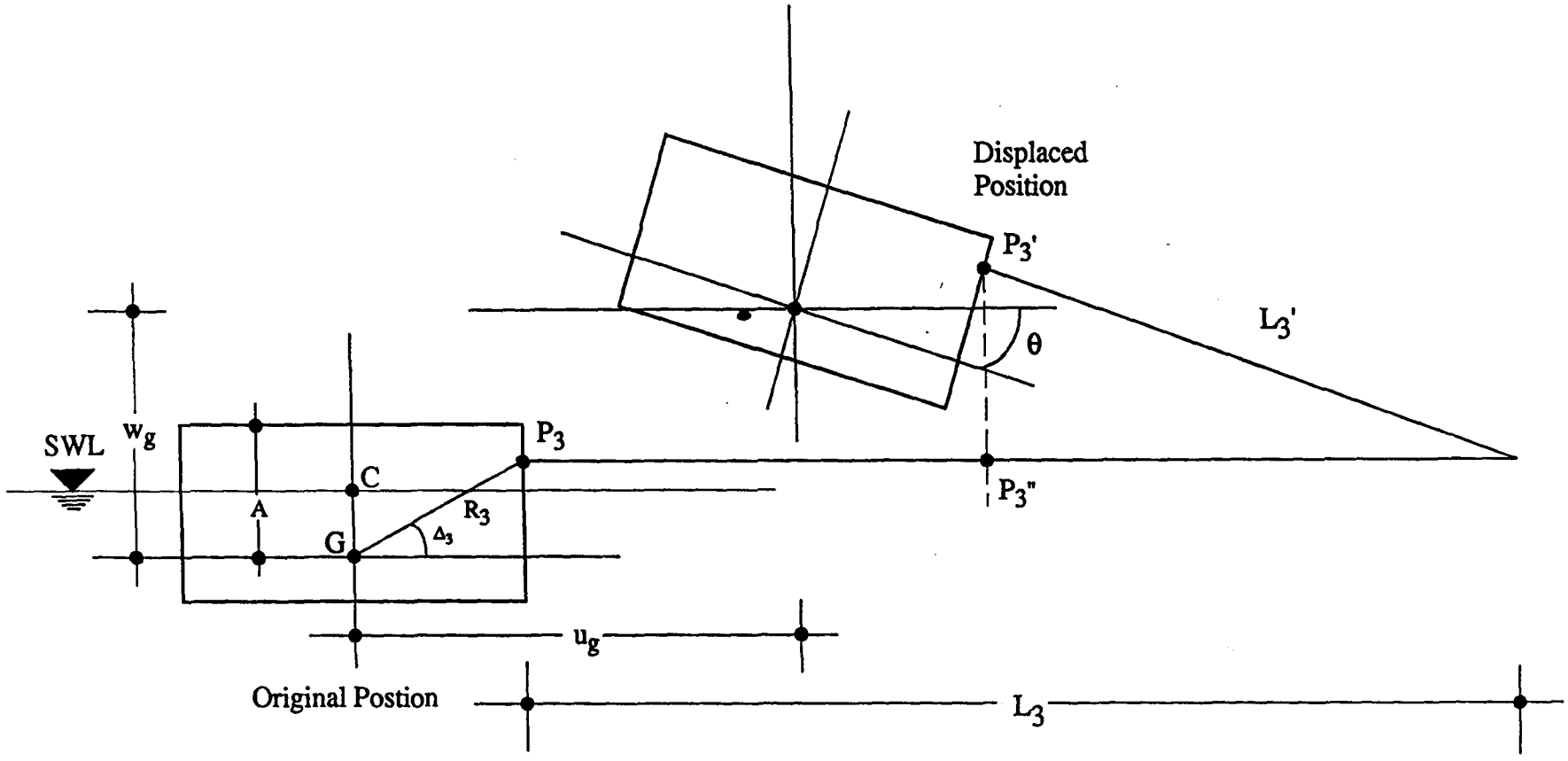

Fig. A-3 Displacement Probe #3, L_3 - original length, L_3' - length at time t

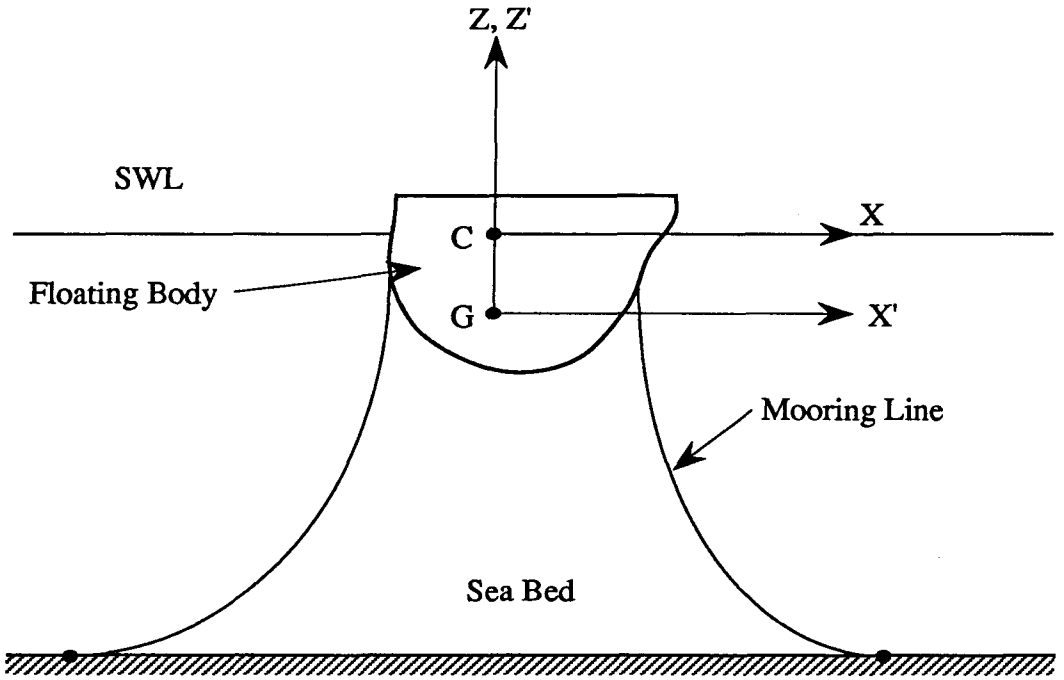

Fig. B-1 Definition sketch of moored two-dimensional floating body

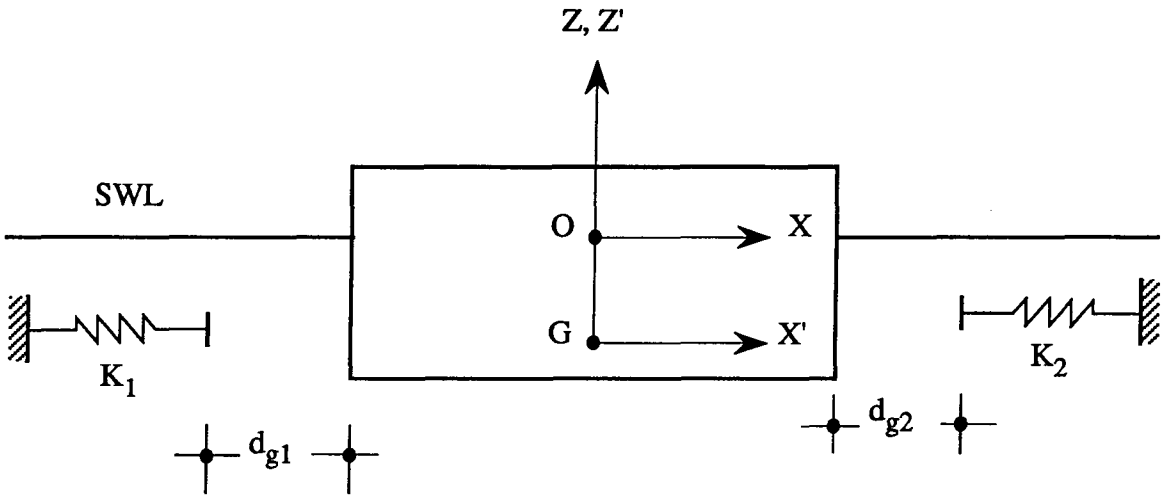

Fig. B-2 Mathematical model of moored floating object with nonlinear moorings